MEASUREMENT SCIENCE REVIEW, **17**, (2017), No. 1, 1-8

DE GRUYTER OPEN

MEASUREMENT SCIENCE REVIEW

ISSN 1335-8871

Journal homepage: http://www.degruyter.com/view/j/msr

Range Detection of the Extremely Low-Frequency Magnetic Field Produced by Laptop's AC Adapter

Darko Brodić[1], Alessia Amelio[2]

[1]*University of Belgrade, Technical Faculty in Bor, Vojske Jugoslavije 12, 19210 Bor, Serbia, dbrodic@tfbor.bg.ac.rs*
[2]*DIMES University of Calabria, Via Pietro Bucci Cube 44, 87036 Rende (CS), Italy, aamelio@dimes.unical.it*

Human exposure to extremely low frequency magnetic field represents a risk to their health. This paper takes into consideration the level of an extremely low-frequency magnetic field between 30 and 300 Hz emitted by an AC laptop adapter. The experiment consists of testing 17 different AC adapters for laptops. During the testing, laptops are operated in a normal operating conditions as well as under heavy load. The magnetic field measurement is conducted in the area around the AC adapter. Obtained data is evaluated according to the critical level of the magnetic field proposed by safety standards. Furthermore, data is classified by a K-medians method in order to determine the critical levels of the magnetic field exposure in the nearby area of the AC adapter. Obtained classifications are evaluated according to safety standards, giving a critical analysis of magnetic field areas at risk. Due to emission of a very strong magnetic field in certain areas, a recommendation for safety use of the AC adapter is proposed.

Keywords: AC adapter, classification, dangerous levels, magnetic field, measurement.

1. INTRODUCTION

Magnetic fields can be generated by natural or man-made sources, which are typically a product of civilization [1]. These magnetic fields can be divided according to their characteristics. The naturally produced magnetic field, which is generated by the Earth, is characterized as a static one. On the contrary, the man-made sources determine a magnetic field with high peaks at different frequencies. It is especially noticeable for extremely low frequency (ELF) range, which is frequently encountered from electrical appliances. This frequency range is between 30 and 300 Hz [2]. Research has proven that an ELF magnetic field has certain negative impact on animals [3]. As a consequence, it can represent a potential hazard to human health.

Human exposure to the ELF magnetic field might cause some negative effects to their health [4]. Researchers have come to the conclusion that ELF magnetic fields can increase the risks of such illnesses as leukemia [5], brain cancer [6], amyotrophic lateral sclerosis [7] and Alzheimer's disease [8]. Furthermore, exposure to ELF magnetic field can have a negative influence on pregnant women, human fetus and small children [9], [10].

The reference level of the magnetic field exposure represents the critical level of the magnetic field emission above which the neighborhood of the emitter is unsafe for humans. The TCO (Tjänstemännens Centralorganisation) standard has proposed a reference level of 0.2 μT in the frequency range up to 2 kHz [11]. In contrast, ICNIRP (International Commission on Non-Ionizing Radiation Protection) has suggested a more relaxed level of 0.2 mT between 50 and 400 Hz [12]. In many other studies the reference level has been selected between 0.2 μT and 0.4 μT [9], [10], [13]. However, a problem still exists for a tested object that emits an ELF magnetic field close to the points where the magnetic field needs to be measured.

Today, laptops are the most widely used types of computers. This is so because of their portability. They represent not only a portable version of the desktop computer, but also a computer-based office on the road. New technologies used for their manufacturing contribute to making them more and more powerful and lighter as well. Furthermore, they are manufactured according to proposed standards like TCO for safe use and with materials that are almost 100 % recyclable [11]. Although they are ecologically friendly, there still exists the problem of their safe use.

Essentially, the problem is linked to the use of electric power which generates an electric and magnetic field. The electric field can be more easily contained by an appropriate shielding than the magnetic field [14]. The magnetic field can be differentiated by its frequency. Different parts of laptops can generate electric and magnetic fields of different frequency. In this way, Wi-Fi, 3G/4G elements produce a very high frequency electromagnetic field, in the range between 2.4 GHz and 6 GHz for Wi-Fi, between 450 MHz and 2 GHz for 3G, and between 2.3 GHz and 5.8 GHz for

DOI: 10.1515/msr-2017-0001

4G [15]. In contrast, other parts of laptops like the Central Processing Unit (CPU), Hard Disk (HD) or Solid State Disk (SSD) and memory produce an extremely low frequency magnetic field, below the range of kHz. This part of the magnetic field is extremely dangerous due to its high level emission. Still, there is an additional element which is prerequisite for any laptop. It is an Alternating to Direct Current (AC/DC) adapter commonly called AC adapter.

The AC adapter represents an electronic device that supplies the laptop with electrical current and charges its battery. Hence, it should be technologically different from the typical computer supply because of its additional role of charging the laptop battery. Also, it should be compact, light and small in order to be the right companion for the laptop in its portability. It consists of a central unit which draws power from an outlet. Furthermore, the unit supplies the current to the laptop through the cord plugged into it.

An AC adapter is classified according to its power rating. It is measured in amperes, volts and/or watts. Typically, it is supplied with AC current at a voltage of 110 or 220 V. Furthermore, an AC adapter creates an output with designated level of current, voltage and power specifically accustomed to each laptop. Today laptops typically use AC adapters that can supply from 30 to 125 W.

In this paper, our attention is directed at the level of the magnetic field emission produced by the AC adapter in an extremely low frequency range. It is a very important topic to investigate because the AC adapter is an unavoidable addition to any laptop. The correct use of the AC adapter is of great importance to any laptop user. In this sense, we have tried to measure the magnetic field produced by AC adapters and further classify it into ranges of different dangerousness to laptop users. It has been established by K-medians clustering according to the safe level limits proposed by different standards and in literature. In the end, we propose some precautions to safely use the AC adapter in the correct way. To the best of our knowledge, we are the first to investigate on this topic and to propose an automatic tool for measuring and classifying the magnetic field emissions of an AC adapter.

This paper is organized as follows. Section 2 gives a brief description of measuring devices. Section 3 describes the elements of the experiment. Section 4 presents the measurement results. Section 5 classifies the obtained results by K-medians clustering method and discusses the results. Section 6 draws a conclusion.

2. MATERIALS AND METHODS

A. Magnetic field

Around the emitter, like a laptop or an AC adapter, users are exposed to the emitted magnetic field. The measurement of the magnetic flux density **B** representing a vector can be split into 3 independent scalar fragments orthogonal to each other, i.e. B_x, B_y and B_z in the direction of the axes *x*, *y* and *z*.

$$\mathbf{B(r,}\,\mathrm{t)} = \mathrm{B_x(t)}\cdot\mathbf{x} + \mathrm{B_y(t)}\cdot\mathbf{y} + \mathrm{B_z(t)}\cdot\mathbf{z}, \tag{1}$$

where *t* is the time, and **r** is the position vector. This vector can be split into 3 independent vectors **x**, **y** and **z**. At a given time point, eq. (1) becomes:

$$\mathbf{B(r)} = B_x\cdot\mathbf{x} + B_y\cdot\mathbf{y} + B_z\cdot\mathbf{x}. \tag{2}$$

Measuring devices measure the scalar components of the magnetic flux density **B**, i.e. B_x, B_y and B_z, and its root mean square (RMS) *B* equal to:

$$B = \sqrt{B_x^{\,2} + B_y^{\,2} + B_z^{\,2}}\ . \tag{3}$$

In the case of magnetic field at multiple frequencies, the total magnetic flux density B_{tot} is defined as:

$$B_{tot} = \sqrt{\sum_{i=1}^{n} B_i}, \tag{4}$$

where B_i is the RMS of the magnetic flux density at frequency *i*, and *n* is the total number of frequencies.

B. Measuring devices

We performed the ELF magnetic field measurement by measuring device Lutron EMF-828 with separate probe [16]. The device measures the magnetic flux density from 0.01 μT to 2 mT in the frequency range from 30 to 300 Hz. It can be used for three measurement extents: 20 μT, 0.2 mT and 2 mT. The precision of the measurement is in the order of 0.01 μT.

The ELF magnetic field is also tested with the measuring device Aaronia Spectran NF-5035 [17], which has a frequency range from 1 Hz to 1 MHz. This measurement confirms the results obtained from Lutron EMF-828. Fig.1. shows the measuring devices Aaronia Spectran NF-5035 and Lutron EMF-828.

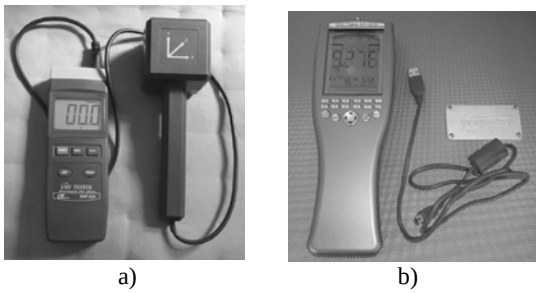

a) b)

Fig.1. The ELF measuring devices: a) Lutron EMF-828, and b) Aaronia Spectran NF-5035.

3. EXPERIMENT

The experiment was conducted on 17 different laptop AC adapters. We proposed 6 measurement positions at which an ELF magnetic field was measured. They were at the top and at the bottom of the AC adapter and 30 cm away from these

positions in four directions which were under 90° to each other. Fig.2. shows the measurement positions.

Furthermore, we tested the AC adapter work in two different operating conditions:

1. Under normal operating conditions, which includes working with office applications, web browsing, etc. All 17 laptops can work in normal operating conditions. Hence, the results from all 17 laptop AC adapters were obtained.
2. Under stress operating condition, using Futuremark 3DMARK Vantage [18] testing program for graphics intensive applications in ref. [19]. Only 9 out of 17 laptops are able to run 3DMARK Vantage. Hence, the results have been obtained for the first 9 out of 17 AC adapters.

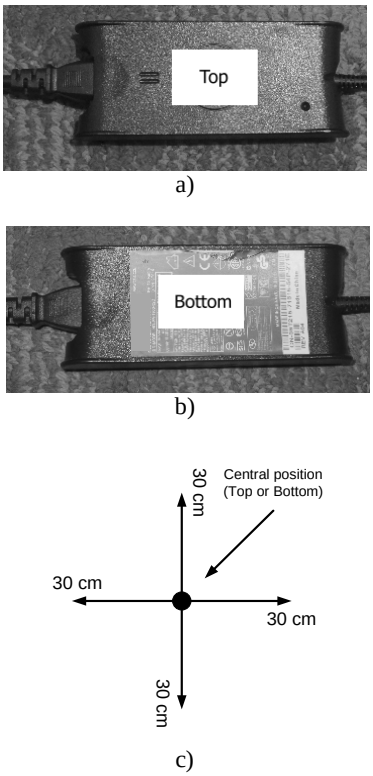

Fig.2. Measurement positions of the AC adapter: a) Top position, b) Bottom position, c) Away positions.

4. MEASURING RESULTS

It can be noticed that the level of the measured magnetic field, which is 30 cm away from the top or bottom positions, is around 0.01 μT. This means that it represents a background magnetic field. Hence, it may be considered as negligible. The results of the measured ELF magnetic field at the top and bottom of the AC adapter in a normal operating condition for all 17 laptops are given in Table 1.

Table 1. includes the following measures: (i) Average, (ii) Difference and (iii) Δ defined as:

$$Average = \frac{EMF(top) + EMF(bottom)}{2}, \quad (5)$$

$$Difference = \left| EMF(top) - EMF(bottom) \right|, \quad (6)$$

$$\Delta = Difference / EMF(top). \quad (7)$$

The magnetic field measured at the top of AC adapters has a minimum value of 0.03 μT, while the maximum value reaches 11.17 μT. Similarly, at the bottom of an AC adapter the obtained minimum value of the measured magnetic field is 0.02 μT, while the maximum has a value of 19.75 μT. If we look carefully at the data, only one AC adapter emits a magnetic field value which is in the safe region.

Table 1. Measured ELF magnetic field at the top and bottom positions of the AC adapters for laptops running in normal conditions.

Laptop No.	Top [μT]	Bottom [μT]	Average [μT]	Difference [μT]	Δ [%]
L1	1.17	0.82	0.99	0.35	30.03
L2	1.76	19.75	10.76	17.99	1019.85
L3	0.56	1.84	1.20	1.28	229.81
L4	10.10	11.77	10.93	1.66	16.48
L5	2.62	4.71	3.67	2.09	79.50
L6	2.93	4.94	3.94	2.01	68.39
L7	4.39	5.40	4.90	1.01	22.90
L8	1.11	3.88	2.50	2.77	249.67
L9	6.29	1.17	3.73	5.12	81.42
L10	2.26	0.65	1.45	1.60	71.05
L11	0.57	2.03	1.30	1.46	257.30
L12	0.51	5.72	3.12	5.21	1020.46
L13	0.49	6.45	3.47	5.96	1210.39
L14	11.17	7.20	9.19	3.97	35.54
L15	2.26	0.65	1.45	1.60	71.05
L16	1.79	3.71	2.75	1.92	106.95
L17	0.03	0.02	0.03	0.01	18.33

Furthermore, if we average the top and bottom magnetic field values, we can get a more uniform result: 2.94 μT at the top and 4.75 μT at the bottom of the AC adapter. Obviously, an AC adapter is designed mainly to emit a lower magnetic field at the top, which means that the position of the AC adapter matters. This is mainly because the circuitry where current flows and where inner components are located is positioned at the bottom of the device. Later, the inclusion of an absolute difference between the top and bottom magnetic field measured value brings new information to be discussed later. The absolute differences are in a range between 0.01 μT and 17.99 μT. It can be noticed that AC adapters emitting higher peaks at any position (top or bottom), typically have a much lower magnetic field emission in the opposite position. This creates extremely high values of differences, which again confirms that the AC adapter is designed to have one "right" position. Obviously, the other position can be considered as a "wrong" position. For this reason, it is convenient to put the "wrong" position of the device on the table, and the "right" position in front of the user. Accordingly, when the device is hanging freely, it is suitable to position its "right" side in front of the user. It is a very important conclusion for the laptop user on how to properly position the AC adapter.

As a confirmation of the previous discussion, we can compute the measure Δ given in % which defines the relative deviation of the measured magnetic field values at the top and at the bottom of the AC adapter. The obtained values are between 16.48 % and 1210.39 %. As a final conclusion, which can be drawn from the results presented in Table 1., it is clear that in spite of differences between AC adapters the level of the measured magnetic field is lower at the top than at the bottom.

Table 2. shows the results of the measured ELF magnetic field at the top and bottom of the AC adapter for the first 9 laptops that operate under stress condition. In this case, only the first 9 out of 17 laptops have passed the test of Futuremark 3DMARK Vantage [18].

Table 2. Measured ELF magnetic field at the top and bottom positions of the AC adapters for laptops running under stress conditions.

Laptop No.	Top [μT]	Bottom [μT]	Average [μT]	Difference [μT]	Δ [%]
L1	5.57	3.77	4.67	1.80	32.33
L2	2.79	20.95	11.87	18.15	649.37
L3	1.28	5.09	3.18	3.81	298.60
L4	12.52	5.44	8.98	7.08	56.52
L5	1.33	1.71	1.52	0.38	28.21
L6	1.09	13.98	7.54	12.89	1178.94
L7	3.76	12.47	8.12	8.71	231.36
L8	2.15	5.32	3.73	3.17	147.49
L9	18.80	7.20	13.00	11.60	61.71

Hence, valid results are obtained for AC adapters of the first 9 laptops. The obtained magnetic field values at the top of AC adapters are between 1.09 μT and 18.80 μT. Also, the measured magnetic field values at the bottom of AC adapters are from 1.7108 to 20.9508 μT. These magnetic field values are higher than those previously obtained in normal operating conditions. Hence, stress condition by intensive graphic programs contributes to higher levels of magnetic field emission. Furthermore, if we average the results of the measured magnetic field obtained from the top and bottom of AC adapters, then their minimum is 1.52 μT, while their maximum is 13.00 μT. Again, the level of the emitted magnetic field is increased by a margin of at least 20 %. Furthermore, the absolute difference receives similar values, i.e. from 0.38 μT to 18.15 μT. Hence, we can conclude that the modality of an operating AC adapter is similar to normal operating conditions leading to a similar efficiency. This point is confirmed by the value of the Δ measure which is between 28.21 and 1178.94 %. However, in spite of similar efficiency, the AC adapter is under higher power consumption when the laptop operates under stress conditions. Essentially, it dissipates power, achieving the highest level of magnetic field emission in its neighborhood. This can be seen in terms of higher power dissipation.

5. CLASSIFICATION

From the laptop user point of view, the most important questions are: (i) What is the level of emitted ELF magnetic field around an AC adapter? (ii) What is the correct way of using the AC adapter? (iii) What is a safe distance from the AC adapter? and (iv) What can be used to minimize safety risks?

To answer all these questions, we can compare the results obtained from measurements of the ELF magnetic field around an AC adapter and use a clustering tool to establish the safety and/or danger zones in order to correctly use the AC adapter.

Each measuring position (top or bottom) of the AC adapter is represented by a one-dimensional feature, which is the measured magnetic field at that position. Consequently, we realize 4 different datasets. The first one (named as top normal) and second one (named as bottom normal) contain the 17 features respectively from the top and bottom part of the AC adapters in normal operating conditions. The third one (named as top stress) and the fourth one (named as bottom stress) include 9 features respectively from the top and bottom part of the AC adapters under stress operating conditions. Each dataset is subjected to a K-medians clustering method to detect magnetic field ranges corresponding to different levels of magnetic fields emitted from AC adapters.

A. The method

K-medians is a center-based clustering method [20] producing compact clusters and quite robust to outliers. We adopted K-medians because it is particularly apt to deal with one-dimensional measured data [21], [22], [23]. Furthermore, a test has been conducted concerning the application of different clustering and discretization algorithms on magnetic field values emitted from an AC adapter. Tests revealed that K-medians produces the best results in terms of ranges below and above the safety limit of 0.2 μT. The number K of output clusters is an input parameter. K-medians considers each cluster represented by its centroid, which is the median value of data inside that cluster. The algorithm consists of a few easy steps: (i) centroids initialization, (ii) data assignment to centroids, and (iii) centroids re-computation. In the first step, K centroids are selected to create initial clusters. This is a critical step, because the selection of initial centroids can influence the final solution. In the second step, each data is assigned to that centroid having the smallest L_1 norm from it. Finally, centroids are computed again for each cluster as the median value of data inside that cluster. Steps (ii) and (iii) are repeated multiple times and centroids change their position, until no movements are performed and centroids become stable. K-medians algorithm aims to minimize the following function:

$$J = \sum_{j=1}^{k} \sum_{i=1}^{n} \left\| x_i^{(j)} - c_j \right\|, \tag{8}$$

where $\|x_i^{(j)} - c_j\|$ is the L_1 norm between the measured value $x_i^{(j)}$ in cluster j and the centroid c_j in cluster j.

B. Results and discussion

Looking at measured values at the top part in Table 1., we notice that only one value, i.e from Laptop 17, is 0.03 μT, is below the reference limit of 0.2 μT. Similarly, at the bottom parts in Table 1., we have only one value below 0.2 μT, i.e. from Laptop 17, which is 0.02 μT. Furthermore, observing the general distribution of top and bottom measured values in normal operating conditions in Table 1., we notice that 4 magnetic field ranges are received. Then, we confirm the optimal K value equal to 4 by experimental evaluation, performed on top normal and bottom normal datasets. In particular, we run K-medians algorithm on the two datasets at different values of a K parameter, from 2 to 5. In this way, we found that the K value determining the best result on both the datasets is 4, because only in this case the low values of 0.03 μT and 0.02 μT are correctly isolated from the other values in both datasets, according to the TCO reference limit of 0.2 μT. Our aim is to correctly separate safe from unsafe measured values (lower and higher than 0.2 μT), we set the K value of K-medians algorithm to 4, in order to receive: (i) low, (ii) middle, (iii) high, and (iv) very high ranges. Association between classifications (low, middle, high and very high) and ranges is performed by considering the maximum and minimum measured values inside each range. Furthermore, the same K value is adopted on top and bottom stress datasets.

The clustering algorithm has been implemented in Matlab R2015a. Clustering experimentation was performed on a laptop computer with Quad-core CPU 2.2 GHz, 16 GB RAM and UNIX operating system. Because K-medians initialization influences the final solution, for each dataset, the algorithm has been run 50 times, each time with a new set of initial centroids. A clustering solution determining the lowest value of *J* function is given as output of the procedure. Application of K-medians algorithm on the top and bottom normal datasets generates the magnetic field ranges reported in Table 3.

It is clearly visible that algorithm determines well-separated ranges from both top and bottom parts of an AC adapter in normal operating conditions. It is also observable that middle and high ranges exhibit minimum and maximum values which are much higher than values of the same ranges obtained from laptop measurement [24], [25], [26]. This is a typical condition of AC adapters and depends on the different architecture of the electrical device. Top and bottom parts emit at a very similar low range, with maximum values of 0.03 μT and 0.02 μT respectively, perfectly discriminated from the algorithm, according to the safety reference limit. On the contrary, the bottom part exhibits different ranges of higher value than the top part. In fact, the top part reaches a middle range with the highest peak of 1.17 μT, while the bottom part emits at a middle range with the highest peak of 2.03 μT. Again, the top part emits at high range with a minimum of 1.79 μT, differently from the bottom part having a minimum of 3.71 μT. Also, the top part has the highest peak of 4.40 μT, while the bottom part reaches 11.77 μT. Finally, a strong difference appears in a very high range, in which the top part reaches the maximum value of 11.18 μT while the bottom part reaches the minimum value of 19 μT.

Table 4. shows the magnetic field ranges obtained from a K-medians algorithm on top and bottom stress datasets. Under stress operating conditions, the bottom part of AC adapter emits a stronger magnetic field level than the top part. In fact, the top part reaches the highest peak in the middle range at 2.15 μT, while the bottom part reaches the highest peak at 7.20 μT. The difference is noticeable for high range, in which the top part exhibits a value between 2.79 μT and 5.57 μT, while the bottom part between 12 μT and 14 μT. Finally, the top part emits at a very high range with a maximum value of 18.80 μT, while the bottom part has a minimum value of 20 μT in the very high range.

Table 3. Magnetic field ranges emitted at top and bottom positions of the AC adapters for laptops running in normal operating conditions.

Top Normal		Bottom Normal	
Magnetic field ranges	min-max values (μT)	Magnetic field ranges	min-max values (μT)
low	0.00 – 0.03	low	0.00 – 0.02
middle	0.49 – 1.17	middle	0.65 – 2.03
high	1.79 – 4.40	high	3.71 – 11.77
very high	6.29 – 11.18	very high	> 19.00

Table 4. Magnetic field ranges emitted at top and bottom positions of the AC adapters for laptops running under stress operating conditions.

Top Stress		Bottom Stress	
Magnetic field ranges	min-max values (μT)	Magnetic field ranges	min-max values (μT)
middle	1.09 – 2.15	middle	1.71 – 7.20
high	2.79 – 5.57	high	12.00 – 14.00
very high	12.52 – 18.80	very high	> 20.00

Again, looking at Table 3. and Table 4., a comparison is performed between ranges in normal operating conditions and under stress. In particular, we can observe that the top part of an AC adapter emits at higher magnetic field levels when it operates under stress conditions rather than in normal conditions. It is confirmed from the highest peak of the middle range, which is 1.17 μT in normal conditions and 2.15 μT under stress conditions. Also, minimum and maximum of high range reach values of 2.79 μT and 5.57 μT respectively under stress conditions, while in normal conditions they are lower and respectively of 1.79 μT and 4.40 μT. The difference is noticeable in the very high range, having a value of 6.29 μT - 11.18 μT in normal conditions, and a much higher value of 12.52 μT - 18.80 μT under stress conditions.

A similar consideration can be observed for the bottom part of the AC adapter. In fact, the highest peak of the middle range is 2.03 μT in normal conditions, differently from the value of 7.20 μT under stress conditions. It is also visible in high range, with a peak of 11.77 μT in normal conditions, and of 14 μT under stress conditions. Finally, very high range includes values higher than 19 μT in normal conditions, and values higher than 20 μT under stress conditions.

An important conclusion of this analysis is that the bottom part of the AC adapter emits at stronger magnetic field levels than its top part. Again, the ranges of the magnetic field of an AC adapter are higher when the laptop is operating under stress conditions than when it runs in normal operating conditions. Finally, the most unsafe conditions for a laptop user are when the laptop is operating under stress conditions and the bottom part of the AC adapter is in direct or close contact with the user.

An analysis of the ranges is very important, but not sufficient to assess the emission degree of AC adapters. To clearly understand other critical aspects, it is essential to know the distribution of top/bottom parts of AC adapters emitting in each range.

Fig.3. shows the composition of the magnetic field ranges obtained on top normal dataset.

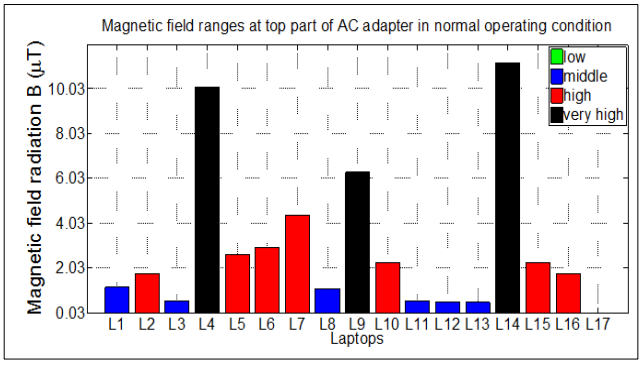

Fig.3. Clustering results corresponding to the magnetic field ranges emitted at the top part of AC adapters when laptops operate in normal conditions. Vertical bars represent the 17 laptops (L1,...,L17) with the top measured value.

We observe that only one AC adapter is included inside the low magnetic field range (Laptop 17), while all other AC adapters are included inside the middle, high and very high ranges. In particular, around 40 % of the top parts of AC adapters emit at high range, while around 35 % of them emit at middle range, which is above the reference limit of 0.2 μT, and around 18 % of them emit at very high range.

Fig.4. illustrates the composition of magnetic field ranges obtained on the bottom normal dataset. Also in this case, only one AC adapter is included in low range (Laptop 17). However, we observe that around 53 % of the bottom parts of AC adapters emit at high range, around 35 % of them emit at middle range, and one bottom part of an AC adapter emits at very high range (Laptop 2). Consequently, also in this case, around 94 % of the bottom parts of AC adapters emit at ranges above the safety reference limit of 0.2 μT.

Fig.5. depicts the composition of magnetic field ranges obtained on top stress dataset. In this case, low range is empty and consequently not reported. Also, around 55 % of the top parts of AC adapters emit at high and very high ranges and around 45 % of the top parts of AC adapters emit in the middle range. This indicates that 10 % more of the top parts of AC adapters emit at a strong magnetic field range wrt the normal operating condition.

Finally, Fig.6. reports the composition of magnetic field ranges obtained on bottom stress dataset. Also in this case, low range is not reported because no AC adapters emit in low range. Although around 67 % of laptop AC adapters are included inside middle range, the inner magnetic field values are very high and far above the limit of 0.2 μT. Again, around 30 % of AC adapters emit in high and very high ranges.

This analysis reveals that a large percentage of laptop AC adapters measured on their top and bottom parts emit at middle, high and very high magnetic field levels, and that very few of them emit at low level. Furthermore, middle, high and very high ranges outweigh the reference safety limit of 0.2 μT. Hence, users should possibly be cautious in managing the AC adapter of laptops. In particular, a safety distance of 30 cm from the center point of an AC adapter should be observed when users operate with a laptop.

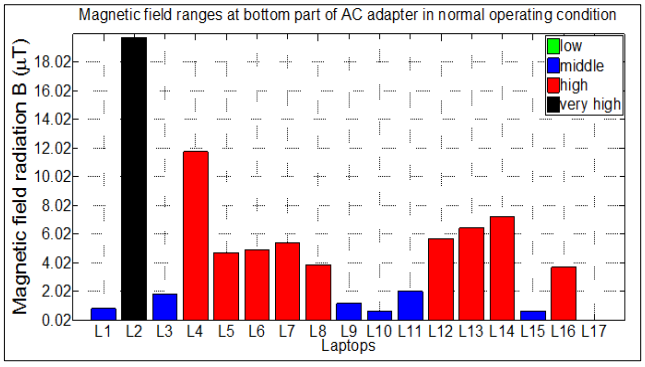

Fig.4. Clustering results corresponding to the magnetic field ranges emitted at the bottom part of AC adapters when laptops operate in normal conditions. Vertical bars represent the 17 laptops (L1,...,L17) with the bottom measured value.

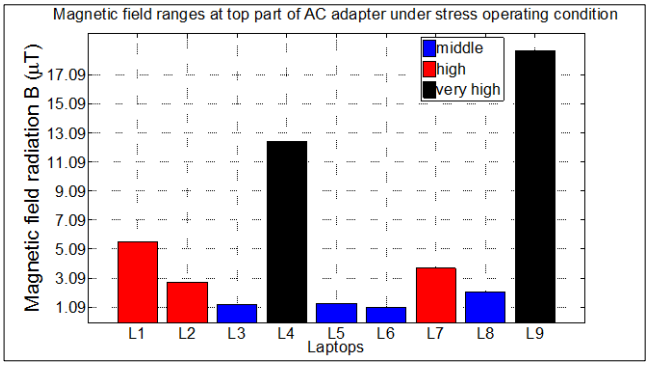

Fig.5. Clustering results corresponding to the magnetic field ranges emitted at the top part of AC adapters when laptops operate under stress conditions. Vertical bars represent the first 9 laptops (L1,...,L9) with the top measured value.

Also, because one of the two parts of AC adapter emits at a higher level of magnetic field (bottom part) than the other part (top part), it is recommended for the users to be in direct contact only with the top part of the AC adapter, when he/she touches it with feet, hands, fingers or other parts of the body. Again, when a laptop operates under stress conditions, that is when a laptop is overloaded with heavy programs, users should avoid contact with the AC adapter of

the laptop. In fact, we have demonstrated that under stress conditions of the laptop, its AC adapter emits magnetic field levels whose prolonged exposition could put at risk human health. Therefore, it is recommended for laptop users to observe these easy safety rules for AC adapters. But, more importantly, it is a suggestion also for laptop manufacturers, who are invited to produce low emission AC adapters as well as checking that the top side of the AC adapter always emits a lower level of ELF magnetic field than bottom side. In this sense, manufacturers should create AC adapters with smaller ELF magnetic field emission at their top. Essentially, the solution (in some cases) can be very easy, i.e. changing only the position of the top and bottom plastic elements. In this way, the changing of the AC adapter sides (top to bottom) will enable lower emission of the ELF magnetic field produced by the AC adapter.

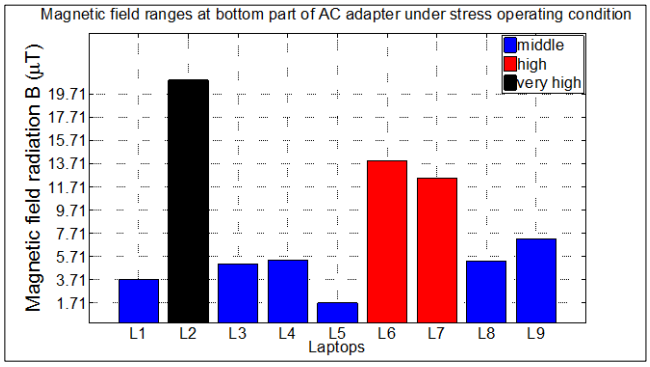

Fig.6. Clustering results corresponding to the magnetic field ranges emitted at the bottom part of AC adapters when laptops operate under stress conditions. Vertical bars represent the first 9 laptops (L1,...,L9) with the bottom measured value.

6. Conclusion

This paper has addressed the problems related to the ELF magnetic field emitted from the AC adapter, which is an infallible companion to the laptop. The measurement of the ELF magnetic field was performed by Lutron EMF-828 and AARONIA NF-5035 devices. The measured results showed a high emission rate of the magnetic field in the area around the AC adapter. To clearly evaluate the results, data has been clustered by a K-medians algorithm in order to differentiate magnetic field levels determining a risk to laptop users. Classification shows that almost all AC adapters emitted a very strong magnetic field. Hence, AC adapters should be used with caution. To employ them safely, we propose putting the AC adapters at least 30 cm away from any part of the human body.

Appendix

A. *TCO standard excerpt*

TCO'05 proposed a measurement methodology of magnetic field RMS value in two frequency ranges: (i) band 1 with a frequency range between 50 Hz and 2 kHz, and (ii) band II with a frequency range between 2 kHz and 400 kHz [11]. TCO measuring geometry includes measurement positions, which are 30 cm away from the emitter of the low frequency magnetic field. Typically, emitters represent the portable computers like a laptop or tablet. Furthermore, proposed measurement geometry has a universal approach. Hence, it can be used also for magnetic field emitters such as AC adapters. Unfortunately, the body position of the portable computer user may be closer than proposed measurement positions. Hence, investigation of an extremely low frequency magnetic field value at a smaller distance or in its center is mandatory from the users' point of view. The measuring positions proposed by the TCO standard for the objects emitting the magnetic field are given in Fig.7.

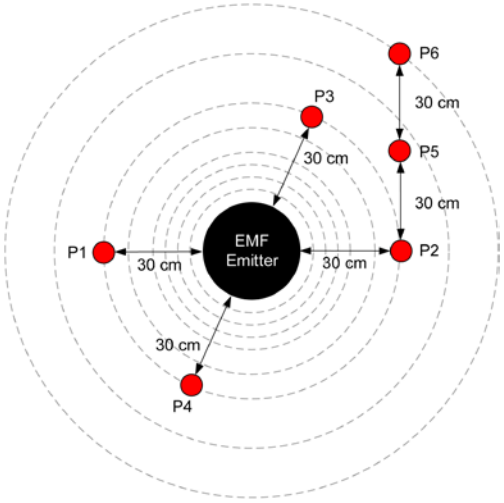

Fig.7. Measuring positions proposed by TCO standard for the objects that emit a magnetic field (P1, ..., P6).

B. *Tested AC adapter characteristics*

Table 5. shows the characteristics of the tested AC adapters, which include output voltage, output current and nominal power consumption.

Table 5. AC adapter characteristics.

Laptop	Voltage [V]	Current [A]	Power [W]
L1	19	6.32	125
L2	19	4.74	90
L3	19	3.95	75
L4	19	3.42	65
L5	19.5	4.62	90
L6	19	2.1	40
L7	19.5	4.62	90
L8	19.5	4.62	90
L9	19	2.37	45
L10	19	3.95	75
L11	19.5	4.62	90
L12	19	4.74	90
L13	19	4.74	90
L14	19	4.22	80
L15	15	5	75
L16	16.5	3.65	60
L17	19	2.37	45

ACKNOWLEDGMENT

This work was partially supported by the Grant of the Ministry of Education, Science and Technological Development of the Republic Serbia [TR33037]. Authors are fully grateful to Ms. Janet Newell, native professor of English language, for her precious editing support.

REFERENCES

[1] IARC. (2002). *IARC Monographs on the Evaluation of Carcinogenic Risks to Humans. Non-Ionizing Radiation, Part 1: Static and Extremely Low-Frequency (ELF) Electric and Magnetic Fields*. IARC Press, Volume 80.

[2] Advisory Group on Non-Ionising Radiation. (2001). ELF electromagnetic fields and the risk of cancer. *Documents of the NRPB*, 12 (1).

[3] Fernie, K.J., Reynolds, S.J. (2005). The effects of electromagnetic fields from power lines on avian reproductive biology and physiology: A review. *Journal of Toxicology and Environmental Health, Part B: Critical Reviews*, 8 (2), 127-140.

[4] World Health Organization (WHO). (2007). *Extremely Low Frequency Fields: Environmental Health Criteria 238*. WHO, ISBN 978-92-4-157238-5.

[5] Bastuji-Garin, S.R., Zittoun, R. (1990). Acute leukemia in workers exposed to electromagnetic fields. *European Journal of Cancer*, 26, 1119-1120.

[6] Harrington, J.M., McBride, D.I., Sorahan, T., Paddle, G.M., Van Tongeren, M. (1997). Occupational exposure to magnetic fields in relation to mortality from brain cancer among electricity generation and transmission workers. *Occupational and Environmental Medicine*, 54, 7-13.

[7] Johansen, C., Olsen, J. (1998). Mortality from amyotrophic lateral sclerosis, other chronic disorders and electric shocks among utility workers. *American Journal of Epidemiology*, 148, 362-368.

[8] Sobel, E., Dunn, M., Davanipour, Z., Qian, Z., Chui, H.C. (1996). Elevated risk of Alzheimer's disease among workers with likely electromagnetic field exposure. *Neurology*, 47, 1477-1481.

[9] Zoppetti, N., Andreuccetti, D., Bellieni, C., Bogi, A., Pinto, I. (2011). Evaluation and characterization of fetal exposures to low frequency magnetic fields generated by laptop computers. *Progress in Biophysics and Molecular Biology*, 107 (3), 456-463.

[10] Bellieni, C.V., Pinto, I., Bogi, A., Zoppetti, N., Andreuccetti, D., Buonocore, G. (2012). Exposure to electromagnetic fields from laptop use of "laptop" computers. *Archives of the Environmental and Occupational Health*, 67 (1), 31-36.

[11] TCO Development AB. (2012). *TCO Certified Notebooks 4.0*. http://tcodevelopment.com/files/2013/04/TCO-Certified-Notebooks-4.0.pdf.

[12] ICNIRP. (2010). Guidelines for limiting exposure to time-varying electric and magnetic fields (1 Hz–100 kHz). *Health Physics*, 99 (6), 818-836.

[13] Calvente, I., Fernandez, M.F., Villalba, J., Ilea, N. (2010). Exposure to electromagnetic fields and its relationship with childhood leukemia: A systematic review. *Science of Total Environment*, 408 (16), 3062-3069.

[14] Ott, H.W. (2009). *Electromagnetic Compatibility Engineering*. John Wiley & Sons.

[15] Koppel, T., Ahonen, M. (2013). Radiofrequency electromagnetic fields from mobile devices used for learning and working. *Elektronika ir Elektrotechnika*, 19 (6), 65-70.

[16] Lutron Electronic Ent. Co., Ltd. *Lutron EMF-828 specification*. www.sunwe.com.tw/lutron/EMF-828eop.pdf.

[17] Aaronia AG. *Aaronia Spectran NF-5035*. http://www.aaronia.com/Datasheets/Spectrum_Analyzer/Gauss_Meter_Spectran_NF-5000.pdf.

[18] Futuremark Corporation. *3DMark Vantage*. http://www.futuremark.com/benchmarks/3dmark-vantage.

[19] Brodić, D. (2015). Measurement of the extremely low frequency magnetic field in the laptop neighborhood. *Revista Facultad de Ingeniería*, 76, 39-45.

[20] Bradley, P.S., Mangasarian, O.L., Street, W.N. (1997). Clustering via concave minimization. In *Advances in Neural Information Processing Systems 9 (NIPS 1996)*. NIPS Proceedings, Denver, CO, USA, 368-374.

[21] Mathews, J., Nair, M.S., Jo, L. (2012). Improved BTC algorithm for gray scale images using k-means quad clustering. In *Neural Information Processing: 19th Int. Conference ICONIP 2012*. Doha, Qatar, 9-17.

[22] Prasad, S., Kumar, P., Sinha, K.P. (2015). Grayscale to color map transformation for efficient image analysis on low processing devices. *Advances in Intelligent Systems and Computing*, 320, 9-18.

[23] Wang, H., Song, M. (2011). Ckmeans.1d.dp: Optimal k-means clustering in one dimension by dynamic programming. *The R Journal*, 3 (2), 29-33.

[24] Brodic, D., Amelio, A. (2015). Classification of the extremely low frequency magnetic field radiation measurement from the laptop computers. *Measurement Science Review*, 15 (4), 202-209.

[25] Brodic, D. (2016). Analysis of the extremely low frequency magnetic field from laptop computers. *Metrology and Measurement Systems*, 23 (1), 143-154.

[26] Brodić, D., Amelio, A. (2016). Detecting of the extremely low frequency magnetic field ranges for laptop in normal operating condition or under stress. *Measurement*, 91, 318-341.

Received October 23, 2016.
Accepted January 30, 2017.

MEASUREMENT SCIENCE REVIEW, **17**, (2017), No. 1, 9–18

DE GRUYTER OPEN

MEASUREMENT SCIENCE REVIEW

Journal homepage: http://www.degruyter.com/view/j/msr

ISSN 1335-8871

Comparison of Two Experiments Based on a Physical and a Torsion Pendulum to Determine the Mass Moment of Inertia Including Measurement Uncertainties

Leonard Klaus

Physikalisch-Technische Bundesanstalt (PTB), Bundesallee 100, 38116 Braunschweig, Germany, leonard.klaus@ptb.de

To determine the mass-moment-of-inertia properties of devices under test with particularly small mass moments of inertia (some $10^{-4}\,\mathrm{kg\,m^2}$), two measurement set-ups based on different measurement principles were developed. One set-up is based on a physical pendulum, the second set-up incorporates a torsion pendulum. Both measurement set-ups and their measurement principles are described in detail, including the the chosen data acquisition and analysis. Measurement uncertainty estimations according to the *Guide to the Expression of Uncertainty in Measurement* (GUM) were carried out for both set-ups by applying Monte Carlo simulations. Both set-ups were compared using the same three devices under test. For each measurement result, the measurement uncertainties were estimated. The measurement results are compared in terms of consistency and the resulting measurement uncertainties. For the given devices under test, the torsion pendulum set-up gave results with smaller measurement uncertainties compared to the set-up incorporating a physical pendulum.

Keywords: Torsional pendulum, calibration, measurement uncertainty evaluation.

1. Introduction

Determining the mass moment of inertia (MMOI) precisely can be important in many applications. For simpler mechanical designs, a calculation based on technical drawings might be sufficient. A measurement is required in the case of a complex design, various materials or if assigned measurement uncertainties are needed.

1.1. Measurement principles and realised set-ups

The experimental determination of the mass moment of inertia based on pendulums is a well-tried method. It is based on the measurement of the pendulum swing frequency, which is dependent on the mass moment of inertia of the device under test (DUT). Approaches based on torsional oscillations feature linear equations of motion and can be implemented as torsion pendulums or filar pendulums [1]. Bi-filar to multi-filar pendulum approaches have been used from the 1930s [2, 3] up to now [4] for the measurement of the mass moment of inertia, especially for heavy objects. The advantage of these approaches is that only few modifications to the device under test are necessary, the set-up is simple, and the added oscillating components have a very small additional MMOI. However, the precision is limited due to the imprecise measurement of the swing frequency and motion in additional degrees of freedom. Both disadvantages may be overcome with more advanced set-ups which cancel out the above-mentioned advantages to some extent due to the higher complexity [5]. Torsion pendulum set-ups are typically used for DUTs with smaller mass moments of inertia [6].

Physical pendulums have also been used for the determination of the mass moment of inertia to a lesser extent [7, 8] or in conjunction with a filar pendulum for measurements in multiple axes [2, 3].

1.2. Purpose of the mass moment of inertia measurements

The combination of the aforementioned requirements for the experimental determination of the mass moment of inertia was the motivation for the design of the set-ups described in this contribution. For the development of a model-based approach for the dynamic calibration of torque transducers [9], different components of a corresponding measurement device had to be analysed in terms of their mechanical properties; amongst other things in terms of the mass moment of inertia. The devices under test have complex mechanical designs, are consisting of different materials and – most importantly – the measurement uncertainties need to be assigned to the measurement results. To this end, two set-ups based on a physical pendulum and on a torsion pendulum were designed, manufactured, and commissioned.

Compared to the presented previously realised set-ups, the specimens for which the mass moment of inertia had to be determined are comparably small and have a low mass moment of inertia in the range of some $10^{-4}\,\mathrm{kg\,m^2}$ rising unique design issues for the set-ups. Typical examples of devices under test

DOI: 10.1515/msr-2017-0002

Fig.1. Typical specimens for which the mass moment of inertia had to be determined by means of the presented pendulum set-ups.

are shown in Figure 1. A first determination of some mass-moment-of-inertia properties of the dynamic torque calibration device was already carried out in 2006 for one part of the calibration device. The chosen method of a torsion pendulum showed unsatisfactory non-linear effects. Aside from that, the results – including measurement accuracies – were good [10].

In the following sections, both set-ups will be described and compared.

2. Physical pendulum

Additional measurements became necessary after modifications to the measuring device and for the development of a model-based calibration approach. To this end, a new set-up based on a physical pendulum was designed. A short overview can be found in [11].

2.1. Measurement principle

A physical pendulum oscillates around a horizontal axis of rotation after being displaced from its vertical equilibrium position, as depicted in Figure 2.

The (ideal) undamped motion of the pendulum is described by

$$J \cdot \ddot{\vartheta}(t) + m \cdot g_{\mathrm{loc}} \cdot l \cdot \sin \vartheta(t) = 0 \qquad (1)$$

with the pendulum's mass moment of inertia J, the excitation angle ϑ, the mass of the pendulum m, the distance of the pendulum's centre of gravity s to its axis of rotation l and the local gravitational acceleration g_{loc}. For small angles of excitation, the latter equation can be linearised applying the small-angle approximation $\sin\varphi \approx \varphi$ giving

$$J \cdot \ddot{\vartheta}(t) + m \cdot g_{\mathrm{loc}} \cdot l \cdot \vartheta(t) = 0 \ . \qquad (2)$$

In the frequency domain, the relation of the mass moment of inertia and the squared angular pendulum swing frequency ω^2 of the linearised equation becomes obvious giving

$$J = \frac{m \cdot g_{\mathrm{loc}} \cdot l}{\omega^2} \ . \qquad (3)$$

The simplifying assumption of linear and undamped oscillations causes deviations, which have to be taken into account for the measurement uncertainty evaluation.

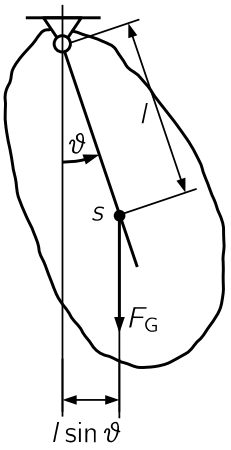

Fig.2. Schematic diagram of a physical pendulum.

2.2. Realised set-up

To realise oscillations with very low damping, the bearing of the pendulum was realised using a spherical air bearing with an aluminium pendulum lever (as depicted in Figure 3). The friction of the bearing was previously analysed for other purposes [12]. Although the friction of the chosen bearing was comparably high compared to other air bearings, it was assumed to be sufficiently low for the given application in conjunction with being robust against bending moments.

On one side of the air bearing, the pendulum lever was mounted by using a centring mechanism, positioning it at a defined position. Mounted on the other side of the air bearing, a precise angle measurement system consisting of a radial grating disk and an incremental scanning head provides time series data of the pendulum excitation angle with high resolution. The analogue quadrature voltage output signals are interpolated and converted to digital TTL signals, before being acquired and analysed using a counter/timer data acquisition card.

With the bearing and the mounted additional components, the pendulum itself has an unknown mass moment of inertia, which is denoted as J_0. To be able to carry out measurements, a known detuning of the pendulum is required for an identification of J_0, or in the case of a measurement with a mounted device under test: $J_0 + J_{\mathrm{DUT}}$. The detuning was realised by adding mass bodies at different distances from the axis of rotation at well-defined positions. For this purpose, the pendulum lever was designed with mounting holes. Each mass body has a cylindrical shape with known dimensions and mass (cf. Figure 7). The mass moment of inertia of each mass body around its cylinder axis can be calculated giving

$$J_{\mathrm{cyl}} = \frac{m \cdot r^2}{2} \qquad (4)$$

with the mass m and the radius r. The Huygens-Steiner theorem gives the acting mass moment of inertia for a mass body at its mounted position at a distance l from the axis of rotation

$$J_{\mathrm{shifted}} = J_{\mathrm{cyl}} + m \cdot l^2 \ . \qquad (5)$$

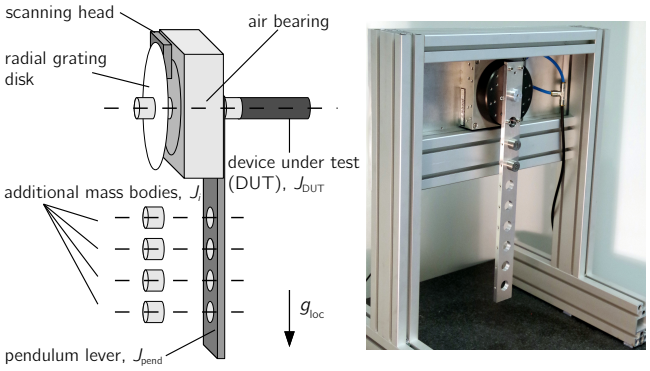

Fig.3. Sketch of the physical pendulum set-up (left) and photograph of the set-up including two added mass bodies mounted on the pendulum lever (right).

The mounting position is known due to measurements of the lever dimensions by means of a coordinate measurement system. However, not only the term of J in Equation (3) will be affected by the added mass bodies, but also the mass of the pendulum and the position of the centre of gravity as well.

The measurement of the mass moment of inertia is carried out with different configurations of added mass bodies, giving for each configuration i the detuned pendulum's equation (cf. (3))

$$J_0 + J_{\mathrm{DUT}} + \sum J_i = \frac{m_0 \cdot g_{\mathrm{loc}} \cdot l_0 + \sum m_i \cdot g_{\mathrm{loc}} \cdot l_i}{\omega_i^2} \quad . \tag{6}$$

The devices under test will not contribute to the restoring torque, because they will be mounted on the axis of rotation. Due to the known J_i, m_i, and l_i, an approximation of the unknown $J_0 + J_{\mathrm{DUT}}$ and restoring torque $m_0 \cdot g_{\mathrm{loc}} \cdot l_0$ is possible. The higher the number of measurement configurations with different mass bodies, the lower the uncertainty of the estimate.

2.3. *Data analysis*

The identification of the mass moment of inertia was carried out using a number of measurements with different numbers of mass bodies at different positions in the pendulum lever. The swing frequency of each measurement was determined applying a sine fit algorithm to the time series data set. To this end, a damped sine function

$$y(t) = \hat{y}_0 \cdot \mathrm{e}^{-\delta t} \cdot \sin(\omega t + \varphi) + B \tag{7}$$

with the magnitude $\hat{y}_0$, offset B, decay rate δ, angular frequency ω, and phase angle φ was approximated to the measurement data. The procedure of the data acquisition and analysis is diagrammed in Figure 4.

The parameter approximation to derive the unknown mass moment of inertia and the restoring torque is carried out as a bivariate regression incorporating a non-linear model function G

$$y = G(X, \theta) \tag{8}$$

relating the measured frequencies ω_i in the vector of observed

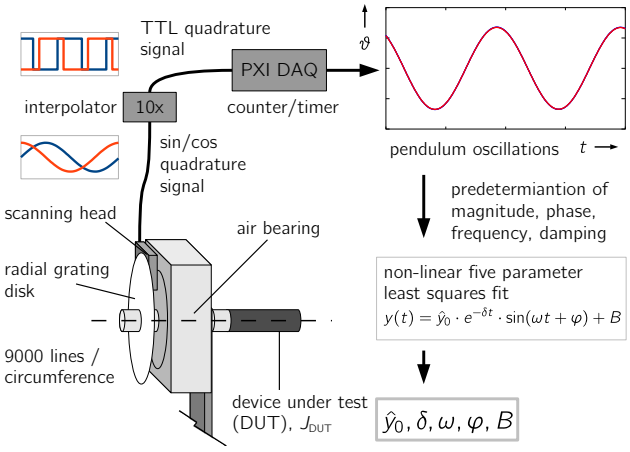

Fig.4. Angle measurement, data acquisition and processing for the physical pendulum set-up.

values y

$$y = [\omega_1, \omega_2, \ldots, \omega_n]^{\mathrm{T}} \tag{9}$$

to the matrix of independent values X consisting of the added mass moments of inertia and the restoring torque values of the corresponding configurations

$$X = \begin{bmatrix} \sum J_1 & \sum (m_1 \cdot g_{\mathrm{loc}} \cdot l_1) \\ \sum J_2 & \sum (m_2 \cdot g_{\mathrm{loc}} \cdot l_2) \\ \ldots & \ldots \\ \sum J_n & \sum (m_n \cdot g_{\mathrm{loc}} \cdot l_n) \end{bmatrix} \quad , \tag{10}$$

and also to the vector of approximated parameters θ as

$$\theta = [J_0 + J_{\mathrm{DUT}}, \sum (m_0 \cdot g_{\mathrm{loc}} \cdot l_0)]^{\mathrm{T}} \quad . \tag{11}$$

For the parameter estimation, an iterative least squares estimator was applied to the non-linear model equation. The sum of the squared errors is minimised in order to estimate the parameters giving

$$\hat{\theta} = \arg\min_{\hat{\theta}} (y - G(X, \theta))^2 \quad . \tag{12}$$

For the determination of the mass moment of inertia of a DUT, in a first step the properties of the pendulum itself (J_0, $m_0 \cdot g_{\mathrm{loc}} \cdot l_0$) had to be determined. Consecutively, it was possible to carry out additional measurements with the mounted DUT. The mass moment of inertia was derived by the subtraction of the two measurement results as follows

$$J_{\mathrm{DUT}} = (J_0 + J_{\mathrm{DUT}}) - J_0 \quad . \tag{13}$$

2.4. *Deviations due to linearisation*

The identification of the mass moment of inertia is based on the assumption of a linear behaviour of the physical pendulum. The real pendulum's swing time is dependent on the pendulum excitation angle, and will only converge to the linear behaviour for small pendulum excitation angles. For the measurement uncertainty evaluation, the influence of the non-linearity had to be estimated. The pendulum equation (cf. (1)) – although

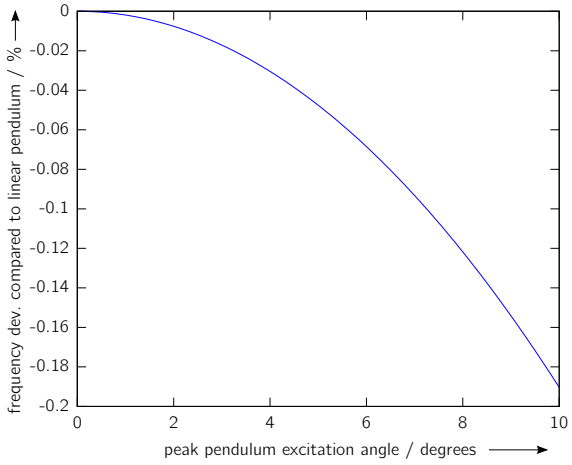

Fig. 5. Deviation of the physical pendulum swing frequency and a linear model assumption as a function of the peak excitation angle.

apparently simple – is not easy to solve and was investigated in several publications [7, 13, 14, 15]. The deviations due to the linearisation were quantised with regard to the peak excitation angle ϑ_s of the pendulum.

The pendulum swing time τ_{ϑ_s} of the non-linear physical pendulum is given [7] as

$$\tau_{\vartheta_s} = \frac{2}{\pi}\,\tau_0\,K(k) \quad , \tag{14}$$

with the swing time τ_0 of the linear solution (cf. Equation (2))

$$\tau_0 = 2\pi\sqrt{\frac{J}{m\cdot l\cdot g_{\mathrm{loc}}}} \quad , \tag{15}$$

and the elliptic integral of the first kind $K(k)$ [16, pp. 569]

$$K(k) = \int_0^{\frac{\pi}{2}} \frac{\mathrm{d}\varphi}{(1-k^2\sin^2\varphi)^{\frac{1}{2}}} \quad . \tag{16}$$

For the non-linear pendulum with the excitation angle ϑ_s, the expression below follows for k [17, pp. 208]

$$k = \sin(\frac{\vartheta_s}{2}) \quad . \tag{17}$$

Therefore, the ratio of linear and non-linear pendulum swing time is given as

$$\frac{\tau_{\vartheta_s}}{\tau_0} = \frac{2}{\pi}\int_0^{\frac{\pi}{2}} \frac{\mathrm{d}\varphi}{(1-k^2\sin^2\varphi)^{\frac{1}{2}}} \quad . \tag{18}$$

Figure 5 depicts the calculated deviations of the pendulum swing frequencies of the linear and non-linear model. It becomes obvious that the deviations are very small for small pendulum excitation angles. The remaining influences of the chosen peak excitation angles of less than 2.5° are only in a range of 1×10^{-4} and are taken into account for the measurement uncertainty estimation.

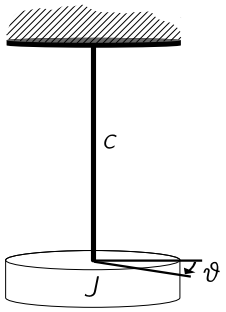

Fig. 6. Schematic diagram of a torsion pendulum with the spring c and mass moment of inertia J.

3. TORSION PENDULUM

A second approach implemented for the determination of the mass moment of inertia was a torsion pendulum.

3.1. *Measurement principle*

A torsion pendulum consists of typically vertically arranged components which are able to oscillate rotationally. Differently from a physical pendulum, the energy of the pendulum is stored in a torsion spring. This spring is fixed at one end, while the other end can rotate freely. A schematic diagram of a torsion pendulum is depicted in Figure 6. After an excitation, oscillations with a natural frequency related to the acting mass moment of inertia will occur.

The homogeneous equation of motion under the assumption of undamped oscillations follows as

$$J\cdot\ddot{\vartheta}(t) + c\cdot\vartheta(t) = 0 \tag{19}$$

with the angle of excitation ϑ, the torsional stiffness of the spring c, and the mass moment of inertia J. In the frequency domain, the linear relation of the inverse of the squared angular swing frequency ω and the mass moment of inertia becomes obvious

$$J = \frac{c}{\omega^2} \quad . \tag{20}$$

Due to the fact that the torsional stiffness of the spring used in a set-up for the determination of the mass moment of inertia is usually unknown, an approach comparable to the one chosen for the physical pendulum had to be applied. Multiple measurements with different added known mass bodies were used to estimate the mass moment of inertia of a device under test by applying a linear regression. The mass-moment-of-inertia elements used were made of brass and are shown in Figure 7.

3.2. *Measurement set-up*

The measurement set-up of the torsion pendulum is based on components of the dynamic torque calibration device, whose mass-moment-of-inertia properties had to be determined. The set-up is depicted in Figure 8. This approach has numerous advantages over a dedicated measurement set-up:

Fig.7. Added mass-moment-of-inertia elements for the torsion pendulum (left) and for the physical pendulum (right).

- Only small modifications to the dynamic torque calibration device are needed for the measurement of the mass moment of inertia
- Measurements are performed under the same conditions as in the later dynamic torque calibration application
- Angle measurement components are already existing and adjusted
- Set-up can be established in a short time.

As already mentioned, a similar approach designed and commissioned a decade ago showed non-linear behaviour. The source of the non-linearities was not clearly identified. Several actions were taken to minimise non-linearities in the actual set-up:

- Press-fitted upper and lower mounting parts with large overlap areas to the spring to reduce local stress maxima
- Longer torsion spring to limit strain despite a larger diameter of the spring compared to the first set-up
- Small angles of excitation to reduce strain.

The integration of the torsion pendulum in the dynamic torque calibration device was carried out so that the pendulum was detachable. The torsion spring is mounted on the top of the rotor of an air bearing, and a radial grating disk is mounted below. An incremental scanning head measures the pendulum excitation angle utilising the grating disk. The additional mass bodies are mounted using a coupling element.

To avoid any modifications to the rotating components of the dynamic torque calibration device, the lower part of the torsion spring needed to be connected without any permanent mounting components. Therefore, a disk-shaped lower ending of the torsion spring was designed, which was connected to the air bearing's rotor by means of bonding wax. The applied *Stronghold Blanchard Wax 7036* – typically used for the temporary mounting of semiconductor wafers – is recommended for the mounting of accelerometers [18]. Being solid at room temperature, the wax starts to soften if heated to temperatures above 70 °C. It can be removed easily using acetone as a solvent.

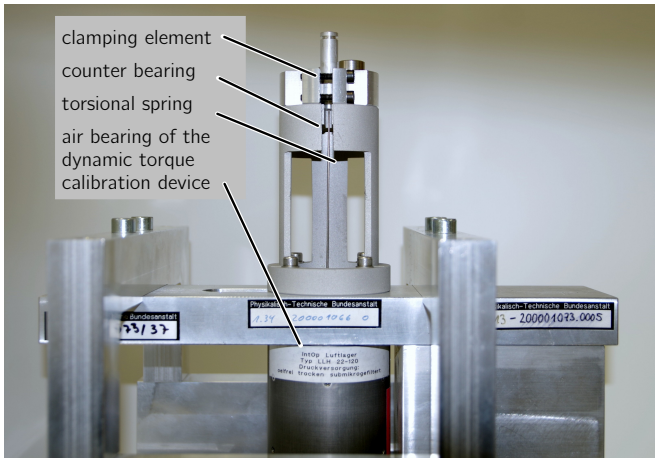

Fig.8. Set-up for the determination of the mass moment of inertia based on a torsion pendulum.

For mounting the torsion spring to the rotor of the air bearing, both parts were heated to temperatures high enough to make the mounting wax completely liquid. Both components were pressed together to obtain a thin and stable layer of wax.

3.3. *Data analysis*

The measurement of the time-varying angle excitation of the torsion pendulum was carried out similarly to the physical pendulum by means of an incremental angle measurement system, and a sine function was applied to the time series data (cf. Equation (7)). After deriving the swing frequencies, the actual MMOI of the device under test was determined by means of a linear regression. From the inverse of Equation (20) the expression below follows for the squared pendulum swing time

$$\tau^2 = \frac{4\,\pi^2}{c}(J_{\mathrm{DUT}} + J_i) \quad . \tag{21}$$

The line equation has a zero at $J_i = -J_{\mathrm{DUT}}$. For a number of measurements with different known added mass-moment-of-inertia bodies J_i, a line equation can be approximated to the measurement data. The intersection of the approximated line and the x-axis gives the extrapolated mass moment of inertia of the DUT, as depicted in Figure 9.

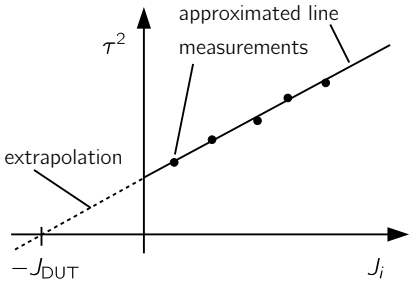

Fig.9. Determination of the mass moment of inertia by means of a line approximation.

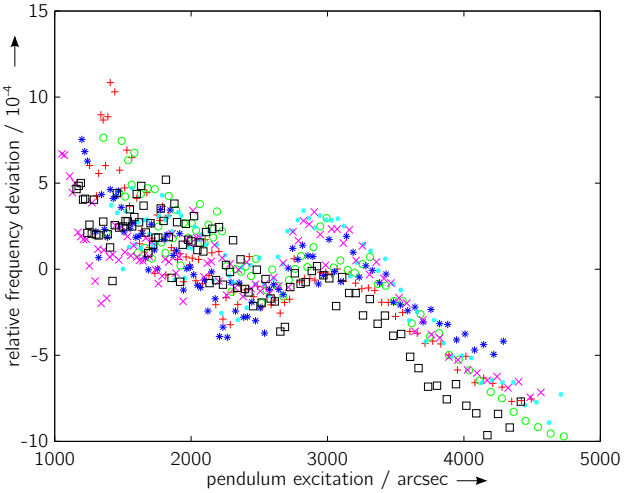

Fig. 10. Dependency of the relative deviation of the pendulum swing frequency on the pendulum excitation angle for each mass body configuration.

The mass moment of inertia of the pendulum itself, i.e. of the top part of the measuring device, needs to be subtracted, depending on for which device under test the mass moment of inertia is to be determined. This is similar to the procedure applied for the physical pendulum set-up (cf. Equation (13)).

3.4. *Non-linearities*

The linearity of the torsion pendulum is one advantage if choosing this design. However, the set-up which was first established experienced significant non-linear behaviour. As mentioned before, the design of the new torsion pendulum set-up was optimised in order to minimise non-linearity. The non-linear behaviour becomes obvious if there is an excitation-dependent change in the pendulum swing frequency.

After commissioning the new pendulum set-up, dedicated analyses were carried out to quantise the amount of non-linear behaviour. For this purpose, time series data of pendulum swings was divided into segments of about one oscillation. The frequency of each oscillation was determined by means of a sine fit. The results are depicted as the swing-frequency deviation versus excitation in Figure 10.

It becomes obvious from the results that small non-linear effects still remain. The swing frequency clearly increases with decreasing swing amplitude. This behaviour is similar for all measurements and is most likely caused by the mounting of the torsion spring with wax. The rotor of the air bearing was modified in the set-up which was first established in order to mount the torsion spring. This was not possible in the latter case.

The magnitude of the pendulum frequency change was significantly reduced by a factor of 10. While the first set-up experienced a frequency change of about 1 % relative to the mean value per an excitation of 1000 arcsec, this non-linear effect was reduced to 0.1 % in the actual set-up.

4. MEASUREMENT UNCERTAINTY EVALUATION

The measurement uncertainty of both set-ups was estimated based on the *Guide to the Expression of Uncertainty in Measurement* (GUM) [19] and its *Supplement 1* (GUM S1) [20], respectively. The evaluation of the measurement uncertainty according to the GUM is based on a mathematical model of the measurement itself. Measurement uncertainty contributions due to different input quantities $X_1, X_2, \ldots, X_n$ are propagated to the measurement result Y based on the measurement's model function giving

$$Y = f(X_1, X_2, \ldots, X_n) \ . \tag{22}$$

Every single input quantity is characterised by its probability density function (PDF), leading to a corresponding PDF of the measurement result.

The classic estimation of measurement uncertainties in the GUM based on partial derivative calculations is limited in terms of possible input PDFs and assumes a linear measurement model. The approach proposed in the GUM S1 incorporates a repeated simulation of the measurement process by means of Monte Carlo simulations. The measurement uncertainties of the different input quantities are simulated by their PDFs. Each simulation is carried out with random samples drawn from the PDFs.

4.1. *Dependency of estimated uncertainty and number of Monte Carlo runs*

The outcome of Monte Carlo simulations may be dependent on the number of simulation runs. If the number of runs is too low, the estimated uncertainties may be too high or too low. To avoid this problem, a sufficiently high number of simulations have to be carried out. Unfortunately, this number is dependent on the application and therefore cannot be known in advance. To overcome this problem, different proposals to define a stopping criterion have been analysed [21]. For the given application, the uncertainty calculation was carried out for different numbers of Monte Carlo runs. After analysing the results, a significantly high number of runs (conservative safety margin added) were chosen.

4.2. *Damping*

The models for the determination of the mass moment of inertia for both measurement set-ups assume undamped oscillations. Although the damping in both set-ups was minimised by all measures (mechanical design, use of air bearings), there still might be influences which have to be taken into account for the measurement uncertainty evaluation.

The influence of the remaining damping was estimated by analysing the decay of the pendulum swing over time. To this end, the pendulum oscillations were acquired and a damped sine function (cf. Equation (7)) was approximated to the acquired time series data. The parameters of interest are, in this case, the decay rate δ and the pendulum's damped angular frequency ω_d. Both relate to the (theoretical) undamped pend-

Table 1. Uncertainty contributions for the determination of the physical pendulum set-up.

input quantity	uncertainty contribution	distribution/ correlated (y/n)
angle deviation grating	$u = 0.033\,\text{arcsec}$	Gaussian (n)
angle dev. signal period	$u = 1.44\,\text{arcsec}$	rectangular (n)
angle dev. eccentricity	$u = 0.39\,\text{arcsec}$	rectangular (n)
frequency deviation non-linearity	$u_{\text{rel}} = 1 \times 10^{-4}$	Gaussian (y)
frequency deviation damping	$u_{\text{rel}} = 1 \times 10^{-7}$	Gaussian (y)
oscillator PXI system	$u_{\text{rel}} = 2.5 \times 10^{-6}$	rectangular (n)
local gravitational acceleration g_{loc}	$u_{\text{rel}} = 5 \times 10^{-8}$	Gaussian (n)
pendulum tilt	$u_{\text{rel}} = 1.25 \times 10^{-7}$	Gaussian (y)
determination of mass	$u = 5 \times 10^{-8}\,\text{kg}$	Gaussian (y)
pendulum position	$u = 2 \times 10^{-6}\,\text{m}$	Gaussian (n)
dimensions mass bodies	$u = 2 \times 10^{-6}\,\text{m}$	Gaussian (y)
bevels of mass bodies	$u = 4 \times 10^{-9}\,\text{kg m}^2$	Gaussian (y)

Table 2. Uncertainty contributions for the determination of the torsion pendulum set-up.

input quantity	uncertainty contribution	distribution
angle deviation grating	$u = 0.06\,\text{arcsec}$	Gaussian
angle dev. signal period	$u = 0.5\,\text{arcsec}$	rectangular
angle dev. eccentricity	$u = 0.06\,\text{arcsec}$	rectangular
frequency deviation non-linearity	$u_{\text{rel}} = 1 \times 10^{-3}$	Gaussian
frequency deviation damping	$u_{\text{rel}} = 2.1 \times 10^{-6}$	Gaussian
oscillator PXI system	$u_{\text{rel}} = 2.5 \times 10^{-6}$	rectangular
mass bodies	$u = 9.48 \times 10^{-8}\,\text{kg m}^2$	Gaussian
J torsion spring	$u = 2.2 \times 10^{-10}\,\text{kg m}^2$	Gaussian
J mounting disk	$u = 7.9 \times 10^{-9}\,\text{kg m}^2$	Gaussian
J wax film	$u = 18.5 \times 10^{-12}\,\text{kg m}^2$	Gaussian

ulum oscillation frequency ω_0 giving

$$\omega_0 = \sqrt{\delta^2 + \omega_{\text{d}}^2} \quad . \tag{23}$$

Data from several measurements derived values of 2.1×10^{-6} for the torsion pendulum set-up and 1×10^{-7} for the physical pendulum set-up for the maximum relative deviation due to the damping.

4.3. *Uncertainty contributions for the two set-ups*

For each of the set-ups, the different measurement uncertainty contributions were identified and quantised.

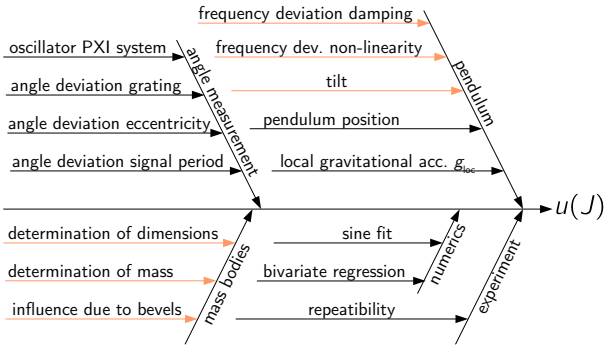

Fig. 11. Ishikawa diagram of the measurement uncertainty contributions of the set-up based on a physical pendulum. Correlated uncertainty contributions are marked in orange.

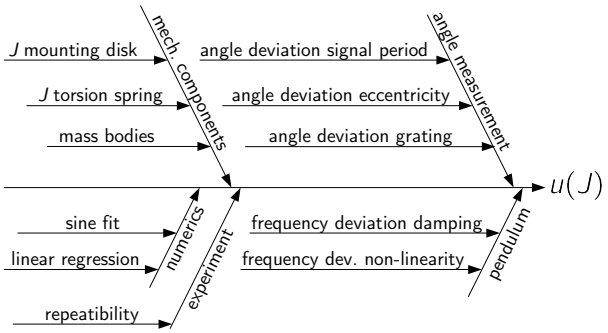

Fig. 12. Ishikawa diagram of the measurement uncertainty contributions of the set-up based on a torsion pendulum.

The different uncertainty contributions of the physical pendulum are displayed in Figure 11 as an Ishikawa diagram, and are given in detail in Table 1. The same information for the torsion pendulum set-up can be found in Figure 12 and Table 2, respectively.

For each measurement, i.e. each set of different time series data files of pendulum measurements with varying added mass-moment-of-inertia elements, Monte Carlo simulations were carried out in order to estimate the measurement uncertainty. The calculations were performed using the open source numerical computation software GNU Octave [22]. The Monte Carlo simulations included the whole data analysis applying uncertainty contributions of the time series data to the measurement data files, uncertainty contributions corresponding to fit parameters in the corresponding code for the parameter estimation, and so on.

The physical pendulum set-up contains correlated uncertainty contributions (marked orange in Figure 11) due to the subtraction of the mass moment of inertia of the pendulum itself (J_0), which was derived by a second measurement. These correlated uncertainty contributions were applied by sampling from the same random number generator. Therefore, the two measurements of $J_0 + J_{\text{DUT}}$ and J_0 were included in one Monte Carlo simulation.

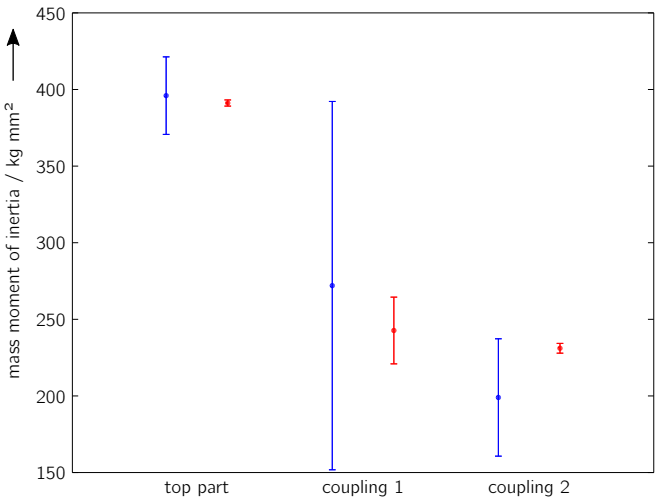

Fig. 13. Measurement results for the mass moment of inertia of three DUTs determined by means of the physical pendulum set-up (blue) and the torsion pendulum set-up (red) including the assigned expanded measurement uncertainties ($k = 2$).

The torsion pendulum results contain no correlated input quantities. Although measurement results of different measurements are subtracted, correlated input quantities were not assumed. Differently to the procedure with the physical pendulum set-up, the torsion spring was removed and remounted for all measurements; the same applies to the mass bodies and the coupling elements on which the mass bodies were mounted.

The measurement uncertainties for the local gravitational acceleration are so small, because the building in which the measurements were carried out has a narrow grid of measured values of g_{loc} on different floors [23]. The nearest measurement point of g_{loc} was just a few metres away from the laboratory with the pendulum set-ups.

4.4. *Additional uncertainty contributions*

It is possible that there are additional uncertainty contributions, which cannot be accounted for in the Monte Carlo simulation. These contributions may become obvious from repeatability measurements. For instance, if a remounting alters the properties of the DUT or if there is a (minor) violation of the assumption of rotational symmetry due to manufacturing or bending, these uncertainty contributions have to be taken into account as well. Therefore, repeatability measurements with the DUT mounted at different angle positions were carried out with each of the set-ups for the measurement uncertainty estimation. The standard uncertainty contributions s from the Monte Carlo simulation s_{MC} and the contributions from repeatability measurements s_{rep} were added giving

$$s = \sqrt{s_{\mathrm{MC}}^2 + s_{\mathrm{rep}}^2} \ . \tag{24}$$

This approach is very conservative, because the measurement uncertainty contributions already estimated by means of the Monte Carlo simulation might be taken into account a second time in the results of the repeatability measurements. Nevertheless, it was a feasible way to include the experimentally determined contributions.

5. Measurement results

Comparison measurements of the same devices under test were carried out at both measurement set-ups.

5.1. *Devices under test*

Mass moments of inertia of three different DUTs were determined as detailed below:

- The rotor of an air bearing with a radial grating disk
- Two identically constructed coupling elements as depicted in the top left of Figure 1.

For each device under test, several repetitive measurements were carried out. For this purpose, the device under test was dismounted and remounted for the next measurement run.

5.2. *Comparison of results*

Measurement results including the estimated expanded measurement uncertainties (MU) with an expansion factor $k = 2$ are shown in Figure 13 and given in detail in Table 3 for the physical pendulum results and in Table 4 for the torsion pendulum results. It becomes obvious from the results that the two measurement set-ups agree very well within the estimated expanded measurement uncertainties. The relative measurement uncertainties of the torsion pendulum are much smaller compared to the results of the physical pendulum.

The high relative measurement uncertainties of the physical pendulum can be explained by the disadvantageous ratio of the mass moment of inertia of the pendulum (J_0) and of the device under test (J_{DUT}), which is caused by the mechanical design. The relative uncertainties for J_0 itself are satisfying. With a different mechanical design or with DUTs with a higher mass moment of inertia, this ratio would decrease and therefore the resulting relative measurement uncertainties would decrease accordingly.

The significantly higher measurement uncertainty of the DUT *coupling 1* compared to *coupling 2* is due to a minor deformation of coupling 1, which is bent a little. This partial rotational asymmetry causes higher deviations; much higher deviations are found in the physical pendulum set-up, because the returning torque is affected as it depends on the angle position at which the DUT is mounted. The mounted mass bodies tend to straighten a bent DUT in the torsion pendulum set-up as well.

6. Summary

For the determination of the mass moment of inertia of certain components of a dynamic torque calibration device, two measurement set-ups were designed and commissioned. The two set-ups incorporate different measurement principles (a physical pendulum and a torsion pendulum). The measurement

Table 3. Measurement results for the determination of the mass moment of inertia with the physical pendulum.

DUT	mass moment of inertia / kg mm^2	expanded MU $U(k=2)$ / kg mm^2	relative exp. MU $U_{\mathrm{rel}}(k=2)$
top part and pendulum (5 measurements)	2.25×10^4	43.14	0.21 %
pendulum (J_0) (5 measurements)	2.21×10^4	35.35	0.17 %
coupling 1 (3 measurements)	272.38	120.18	44.12 %
coupling 2 (4 measurements)	198.83	38.31	19.27 %
top part (5 measurements)	395.60	25.31	6.4 %

Table 4. Measurement results for the determination of the mass moment of inertia with the torsion pendulum.

DUT	mass moment of inertia / kg mm^2	expanded MU $U(k=2)$/kg mm^2	relative exp. MU $U_{\mathrm{rel}}(k=2)$
coupling 1 (20 measurements)	242.71	21.78	8.97 %
coupling 2 (20 measurements)	231.11	3.19	1.38 %
top part (20 measurements)	395.67	3.77	0.95 %

uncertainties for both set-ups were estimated and the results are presented.

The measurements show a good agreement of the two independent measurements. With the given devices under test, the torsion pendulum set-up has smaller measurement uncertainties. The higher uncertainties of the physical pendulum are caused by the mechanical design of the set-up and not by the measurement principle. The relative uncertainties would be significantly smaller for heavier DUTs or with a different design of the set-up.

ACKNOWLEDGEMENT

The author would like to thank his colleague M. Röhr for designing and manufacturing the torsion spring and carrying out most of the torsion pendulum measurements.

This work was part of the Joint Research Project IND09 *Traceable Dynamic Measurement of Mechanical Quantities* of the European Metrology Research Programme (EMRP). The EMRP is jointly funded by the EMRP participating countries within EURAMET and the European Union.

REFERENCES

[1] Genta, G., Delprete, C. (1994). Some considerations on the experimental determination of moments of inertia. *Meccanica* 29 (2), 125–141. doi: 10.1007/BF01007497.

[2] Soulé, K.A., Miller, M.P. (1933). *The experimental determination of the moments of inertia of airplanes*. NACA Technical Report 467, National Advisory Committee for Aeronautics, Langley Field, USA.

[3] Gracey, W. (1948). *The experimental determination of the moments of inertia of airplanes by a simplified compound-pendulum method*. NACA Technical Note 1629, National Advisory Committee for Aeronautics, Langley Field, USA.

[4] Jardin, M., Mueller, E. (2007). Optimized Measurements of UAV Mass Moment of inertia with a bifilar pendulum. In *AIAA Guidance, Navigation and Control Conference and Exhibit*, 20-23 August 2007, Hilton Head, USA. doi: 10.2514/6.2007-6822.

[5] Swank, A.J. (2012). Precision mass property measurements using a five-wire torsion pendulum. In *27th Annual Meeting of the American Society for Precision Engineering*, 21-26 October 2012, San Diego, USA.

[6] Kooijman, J.D.G., Schwab, A.L., Meijaard, J.P. (2008). Experimental validation of a model of an uncontrolled bicycle. *Multibody System Dynamics* 19 (1-2), 115–132. doi: 10.1007/s11044-007-9050-x.

[7] Pedersen, N.F., Sørensen, O.H. (1977). The compound pendulum in intermediate laboratories and demonstrations. *American Journal of Physics* 45 (10), 994–998. doi: 10.1119/1.10867.

[8] Robertson, R.L., Harris, E.C. (1962). A simplified technique for precision measurement of moment of inertia. In *21st National Conference of the SAWE*, 14-17 May 1962, Seattle, USA. Society of Allied Weight Engineer.

[9] Klaus, L. (2015). Dynamic torque calibration. *PTB Mitteilungen* 125 (2), 12–17. doi: 10.7795/310.20150203.

[10] Bruns, T., Wedmann, A. (2006). Experimentelle Bestimmung von Massenträgheitsmomenten als Ruck-

fuhrungsgroße fur die dynamische Drehmomentkalibrierung (Experimental determination of moments of inertia for traceability in dynamic torque calibration). *tm – Technisches Messen* 73 (12), 692–697. doi: 10.1524/teme.2006.73.12.692.

[11] Klaus, L., Bruns, T., Kobusch, M. (2014). Modelling of a dynamic torque calibration device and determination of model parameters. *Acta IMEKO* 3 (2), 14–18. doi: 10.21014/acta_imeko.v3i2.79.

[12] Peschel, D., Mauersberger, D. (1994). Determination of the friction of aerostatic radial bearings for the lever-mass system of torque standard machines. In *XIII IMEKO World Congress*, 5-9 September 1994, Turin, Italy. IMEKO, 216-220.

[13] Beléndez, A., Pascual, C., Méndez, D.I., Beléndez, T., Neipp, C. (2007). Exact solution for the nonlinear pendulum. *Revista Brasileira de Ensino de Física* 29 (4), 645–648. doi: 10.1590/S1806-11172007000400024.

[14] Baker, G.L., Blackburn, J.A. (2005). *The Pendulum*. Oxford University Press.

[15] Ochs, K. (2011). A comprehensive analytical solution of the nonlinear pendulum. *European Journal of Physics* 32 (2), 479–490. doi: 10.1088/0143-0807/32/2/019.

[16] Abramowitz, M., Stegun, I.A. (eds.) (1964; 1972 – 10th printing with corrections). *Handbook of Mathematical Functions with Formulas, Graphs, and Mathematical Tables*. United States Department of Commerce.

[17] Symon, K.R. (1960). *Mechanics*. 2nd edition. Addison-Wesley.

[18] Endevco Meggit Sensing Systems (2006). *Guide to adhesively mounting accelerometers*. Technical Report.

[19] Joint Committee for Guides in Meteorology. (2008). *Evaluation of measurement data —- Guide to the expression of uncertainty in measurement*. JCGM 100:2008.

[20] Joint Committee for Guides in Meteorology. (2008). *Evaluation of measurement data —- Supplement 1 to the "Guide to the expression of uncertainty in measurement" – Propagation of distributions using a Monte Carlo method*. JCGM 101:2008.

[21] Wübbeler, G., Harris, P.M., Cox, M.G., Elster, C. (2010). A Two-stage procedure for determining the number of trials in the application of a Monte Carlo method for uncertainty evaluation. *Metrologia* 47 (3), 317–325. doi: 10.1088/0026-1394/47/3/023.

[22] Free Software Foundation, Inc. *GNU Octave*. `http://www.octave.org/`.

[23] Lindau, A., Kumme, R., Heiker, A. (2002). Investigation in the local gravity field of a force laboratory of PTB. In *Joint International Conference IMEKO TC3/TC5/TC20: Proceedings of the International Conference on Force, Mass, Torque, Hardness and Civil Engineering Metrology in the Age Globalization*, 24-26 September 2002, Celle, Germany. VDI-Berichte Nr. 1685.

Received October 19, 2016.
Accepted January 25, 2017.

MEASUREMENT SCIENCE REVIEW, **17**, (2017), No. 1, 19-26

DE GRUYTER OPEN

MEASUREMENT SCIENCE REVIEW

Journal homepage: http://www.degruyter.com/view/j/msr

ISSN 1335-8871

Characterization of the Embryogenic Tissue of the Norway Spruce Including a Transition Layer between the Tissue and the Culture Medium by Magnetic Resonance Imaging

R. Kořínek[1], J. Mikulka[2], J. Hřib[3], J. Hudec[1], L. Havel[3], K. Bartušek[1]

[1]*Institute of Scientific Instruments of the CAS, Kralovopolska, 147, 612 64, Brno, Czech Republic, korinek@isibrno.cz*
[2]*Brno University of Technology, Faculty of Electrotechnical Engineering and Communication, Department of Theoretical and Experimental Electrical Engineering, Technická, 3082/12, 616 00, Brno, Czech Republic*
[3]*Mendel University in Brno, Faculty of Agronomy, Department of Plant Biology, Zemedelska, 1, 613 00, Brno, Czech Republic*

The paper describes the visualization of the cells (ESEs) and mucilage (ECMSN) in an embryogenic tissue via magnetic resonance imaging (MRI) relaxometry measurement combined with the subsequent multi-parametric segmentation. The computed relaxometry maps T_1 and T_2 show a thin layer (transition layer) between the culture medium and the embryogenic tissue. The ESEs, mucilage, and transition layer differ in their relaxation times T_1 and T_2; thus, these times can be used to characterize the individual parts within the embryogenic tissue. The observed mean values of the relaxation times T_1 and T_2 of the ESEs, mucilage, and transition layer are as follows: 1469 ± 324 and 53 ± 10 ms, 1784 ± 124 and 74 ± 8 ms, 929 ± 164 and 32 ± 4.7 ms, respectively. The multi-parametric segmentation exploiting the T_1 and T_2 relaxation times as a classifier shows the distribution of the ESEs and mucilage within the embryogenic tissue. The discussed T_1 and T_2 indicators can be utilized to characterize both the growth-related changes in an embryogenic tissue and the effect of biotic/abiotic stresses, thus potentially becoming a distinctive indicator of the state of any examined embryogenic tissue.

Keywords: Norway spruce, ESEs, mucilage, transition layer, MRI relaxometry.

1. INTRODUCTION

Magnetic resonance imaging (MRI) is a non-invasive method widely applied in the study of molecules. The MRI approach is frequently employed not only in medicine but also in biological, biochemical, and chemical research. Most of the papers describing the use of MRI to investigate plant physiology have emphasized certain aspects of anatomy or functional morphology [1]. In plant biology, MRI supports several major activities, namely, the research of the water and mineral compounds transported within a plant [2], [3], the determination of plant metabolites [4], [5], the investigation of cellular processes [6], and the examination of the growth and development of plants [7]. MRI is also instrumental towards monitoring water changes in early somatic embryos (ESEs). Šupálková et al. [8] examine the influence of the ESEs of spruce treated with cadmium and/or lead ions for twelve days using multi-instrumental analytical procedures; these authors employ image analysis to estimate the growth, a fluorimetric sensor to detect the viability of enzyme-treated ESEs, and the MRI technique to facilitate non-destructive measurement of the volume of the ESEs.

The interaction between the cells plays a fundamental role in the growth and development of multicellular organisms. In this context, let us note that the structural integrity of plants was described by, for example, Šebánek et al. [9]; it may also be mentioned that the extracellular matrix (ECM) issue pertains to Dostál's [10] topic of the structural integrity of plant organism [11].

At the early stage of their development, the ESEs are covered with a special extracellular cell wall layer referred to as the extracellular matrix surface network (ECMSN), [12]. Neděla et al. [13], [14], [15] utilized an environmental scanning electron microscope (ESEM) to describe the ECM and/or ECMSN in conifers (spruce, pine, and fir) at the native stage. Arabinogalactan-proteins (AGPs) are progressively accumulated within the ECMSN, a well-known marker covering the embryogenic cells during the embryo development. Specific AGPs are essential in somatic embryogenesis and exhibit the capability of directing the development of the cells [16]. It is possible that AGPs may be present as adhesives in the middle lamella to cement the cell-to-cell contact and they may also be involved in the adhesion of the callus cell clumps [17]. Two homogeneous AGPs were purified from the Norway spruce

DOI: 10.1515/msr-2017-0003

callus cells via ion-exchange and gel-permeation chromatography followed by enzymatic treatment [18]. The function of AGPs was recently summarized in a review by Seifert and Roberts [19].

Our article further extends a related, previously published paper [20], where the authors conducted 4 experiments: 1) the designing of methods to assess the water amount in relevant somatic embryos; 2) a comparison of the SNR in images acquired at different magnetic flux density values of the basic magnetic field; 3) monitoring the tissue growth via various techniques; and 4) the segmentation of two subjectively distinguishable regions in the tissue, with each of these exhibiting a specific T_2 relaxation time. Our research report develops the work carried out by Mikulka et al., especially as regards the image processing methodology. In the given context, the aim of the present article is to utilize MRI relaxometry in order to visualize the relaxation times of the early embryogenic tissue (callus) of the Norway spruce.

2. SUBJECT & METHODS

Plant material

A clone of the somatic embryos (ESEs) of the Norway spruce (Picea abies (L.) Karst.), marked as 2/32, was used in our experiments. The cultures were maintained on a semi-solid (Gelrite Gellan Gum, Merck, Germany), half-strength LP medium [21], which underwent further modifications within later research [22]. The concentrations of 2.4-dichloro-phenoxyacetic acid (2.4-D) and N6 – benzyladenine (BAP) corresponded to 4.4 and 9 µM, respectively [23]. The pH value was adjusted to 5.7 - 5.8 before autoclaving (121°C, 100 kPa, 20 mins.). The organic part of the saccharose-free solution was sterilized by filtering through a 0.2 µm polyethylensulfone membrane (Whatman, Puradisc 25 AS). We used Petri dishes (50 mm in diameter) for the actual cultivation. The sub-cultivation of the stock cultures was performed in two-week intervals; the stock and experimental cultures were maintained at a temperature of 23 ± 2 °C in a cultivation box kept in a dark place.

Isolation of the somatic embryos and mucilage

Ten days after the last passaging, the embryogenic tissues (calluses) of the Norway spruce were used for the isolation of the somatic embryos from the above-discussed heterogeneous, fully asynchronous culture (suspensor cells and embryogenic cells at different stages of development). The most developed somatic embryos with only a minimum amount of mucilage (ECMSN) on the surface were extracted from the embryogenic culture by means of tweezers and placed into two depressions in an acrylic glass cuboid. The mucilage was obtained from the embryogenic tissue (callus) via automatic tweezers placed in the middle of the embryogenic callus; we acquired the substance through capillary attraction and then pipetted it off. This procedure was repeated several times to provide the amount of mucilage necessary to fill the remaining, empty depressions in the applied acrylic glass cuboid. In this manner, the embryos and mucilage were prepared for the MR relaxometry measurement.

MRI relaxometry

Magnetic resonance imaging (MRI) is a non-invasive imaging method to supply information about an examined tissue, enabling us to observe the inner part of the tissue without causing any physical damage. The MR image contrast is influenced by several characteristics of the tissues and other materials; such characteristics include the T_1, T_2, and T_2^* relaxation, spin density, susceptibility, and flow effects. When a magnetized spin system is perturbed from the thermal equilibrium state after radio frequency excitation, then, according to the laws of thermodynamics, the system will return into the state of thermal equilibrium. Practically, in MRI, the measured magnetization vector is equal to the sum of all microscopic magnetic moments in the object. In general terms, the behavior of the magnetization vector over time is defined by the Bloch equation [24]. The longitudinal and transverse relaxation times T_1 and T_2 represent the time evolution of the longitudinal and transverse magnetization while the magnetization of water protons reverts back to the equilibrium, following the radio frequency (RF) excitation. The T_2^* time constant defines the progress of the free induction decay signal. The above-mentioned relaxation times are tissue-specific, and all of them depend on the biophysical and chemical properties of the examined tissue. The image contrast is contingent on the used excitation scheme, frequently referred to as the pulse sequence or technique/method.

The general purpose of the experiment was to perform in situ measurement of the ESEs via MRI relaxometry techniques. To measure the T_2 relaxation, we applied the fast spin-echo (FSE) technique; the T_1 relaxation was measured using the inversion recovery fast spin-echo (IRFSE) method. All the described experiments were performed on a 9.4 T (Bruker) MRI scanner at the Institute of Scientific Instruments, Brno. The MAREVISI (8.2) and MATLAB (R2014b) programs were used for the processing.

Data processing

A method for the multi-parametric segmentation of MR images of tissue cultures was proposed; this segmentation technique exploits the principle of linear mixture models. The values of the relaxation times in the tissue areas have normal distribution (Gaussian distribution); we therefore chose a Gaussian mixture model (GMM), generally expressible as follows [25]:

$$p(\boldsymbol{\theta} \mid \mathbf{x}) = \sum_{i=1}^{K} \tilde{\phi}_i N(\tilde{\boldsymbol{\mu}}_i, \tilde{\boldsymbol{\Sigma}}_i)$$

where the i-th component of the vector of random numbers $\mathbf{x}$ with the normal distribution N is characterized by the

weight $\tilde{\phi}_i$, vector of mean values $\tilde{\boldsymbol{\mu}}_i$, and covariance matrix $\tilde{\boldsymbol{\Sigma}}_i$. The vectors $\tilde{\boldsymbol{\mu}}_i$ and $\tilde{\boldsymbol{\Sigma}}_i$ are estimated via the maximum likelihood method. Direct calculation is virtually unfeasible, owing to strong non-linearity of the optimized function; for this reason, the estimation of the parameter values was performed using an expectation-maximization (EM) algorithm.

The segmentation of the culture images was executed in two steps. Within the first stage, we used Gaussian mixture models to approximate the data of the isolated ESEs and mucilage; in the next stage, the posterior probabilities of pertinence to one of the two GMM components were assigned to the relaxation values of the images. The final segmented image is obtained after thresholding of the acquired probability images.

3. RESULTS

MRI measurements of two embryogenic tissue samples (the Norway spruce) were performed; in this context, we also measured the tissues (the ESEs and mucilage) isolated from the embryogenic tissue. The acquired images were used for the calculation of the T_1 and T_2 maps, which provide the contrast between the ESEs, mucilage, and transition layer. The coronal and axial slices were measured with the following parameters: the field of view (FOV) of 20 × 20 mm; the acquisition matrix size of 256 × 256 pixels; the layer thickness of 0.5 mm; and the layer gap of 0.5 mm. The voxel size of 0.078 × 0.078 × 0.5 mm is derived from the above parameters. Fig.1. shows the PD images and T_1, T_2 maps of the coronal images of the embryogenic tissue (samples No. 1). The slices are numbered from the bottom (substrate) to the top.

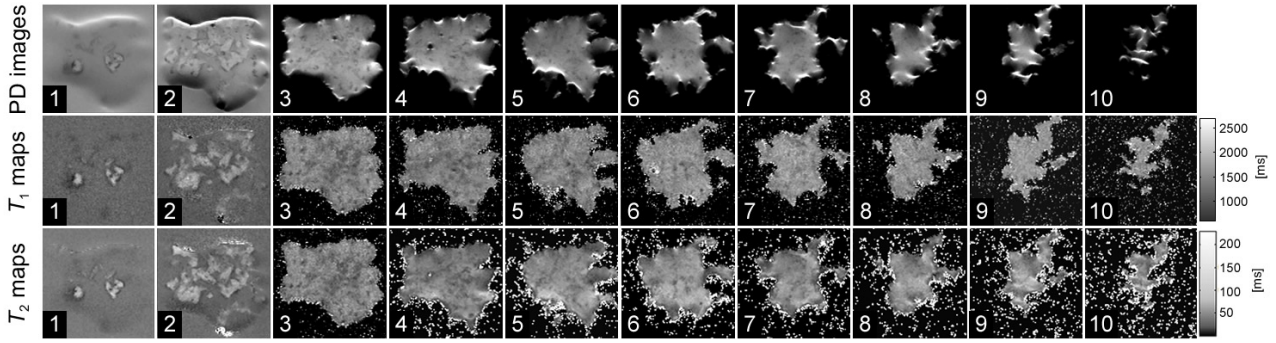

Fig.1. The ten PD-weighted images and T_1, T_2 maps of the coronal slices of the Norway spruce (sample No. 1).

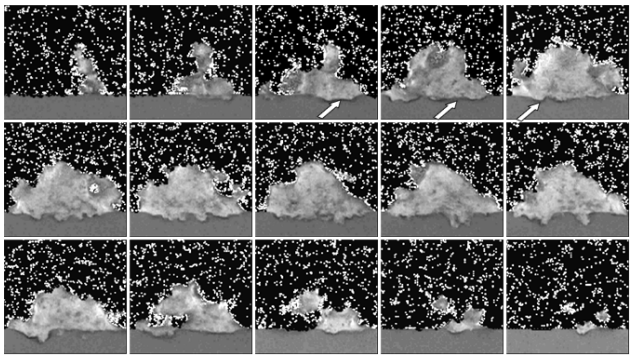

Fig.2. The T_2 maps of the axial slices of the ESEs of the Norway spruce (sample No. 1). The transition layer is indicated by the arrows.

In the acquired axial slices of the embryogenic tissue, the thin layer between the embryogenic tissue and substrate is more visible. Fig.2. shows the T_2 maps exhibiting good contrast between the transition layer, substrate, and embryogenic tissue; the layer is also clearly perceptible in the T_1 maps.

Unlike the PD images, the T_1 and T_2 maps enable us to recognize individual portions of the embryogenic tissue. Manual selection of the region containing the specific parts (the ESEs, mucilage, and transition layer) is not always reproducible; therefore, we performed automatic segmentation of the sought parts to ensure the reproducibility of the experiment. The measured data of the isolated ESEs and mucilage were used in the formation of the model to be applied for the automatic segmentation of the embryogenic tissue.

The distribution of the relaxation times T_1 and T_2 in the isolated ESEs and mucilage is shown in Fig.3. Two regions with different T_1 and T_2 can be subjectively distinguished; the relaxation time values were obtained from two slices where the isolated ESEs and mucilage are plainly visible. The regions of the ESEs and mucilage are represented by 568 and 455 manually selected pixels, respectively.

In the first step, we estimated the basic statistical values from the selected set of relaxation values. For both the ESEs and the mucilage, the sample mean values and sample standard deviations were estimated. Then, the image data (relaxation times) were approximated by means of the two-component GMM, and this model was also used to estimate the mean values and standard deviations. The result of approximating the three-dimensional (3D) histograms via the GMM is presented in Fig.3.; the 3D histogram shows two areas with normal distribution.

The calculated mean values of the relaxation times of the ESEs and mucilage determined for two different approaches are shown in Table 1. In the former case, we defined the statistical parameters, namely, the sample mean value and standard deviation, from randomly selected pixels inside the ESEs and mucilage; as regards the latter approach, estimations of the mean values and standard deviations were

established from the two-component GMM applied to the same data. The mean values and standard deviations of the relaxation times T_1 and T_2 for both approaches correspond to each other; this fact confirms the assumed normal distribution of the relaxation times inside the homogeneous regions, and it also clearly points to the possibility of modeling the image data through the use of a GMM.

The second processing stage consists of the computation of the probability images, where each pixel represents the probability that a pixel belongs to the ESEs or mucilage. In the case of the two-component model, two probability images are obtained. The results acquired from one slice of sample 2 (culture) are shown in Fig.4.; here, the left image shows the pixels pertaining to the ESEs, while the right one indicates those related to the mucilage.

In the last processing stage, the probability images are segmented by means of the threshold method. The segmentation threshold was determined according to the 3σ (3-sigma) principle, which is a very strict criterion; for this reason, we preferred 1σ. In the case of normal distribution, 1σ expresses the probability of p = 68.2 % that a pixel really belongs to the ESEs or mucilage. The result of the thresholding is utilized for the segmentation of the original T_1- and T_2-weighted images. The segmented regions for both samples are presented in Fig.5., where the red line defines the entire area of the analyzed embryogenic tissue, the yellow one separates the regions with the ESEs, and the blue one marks the mucilage regions; for the latter two groups, the probability of p = 68.2 % applies.

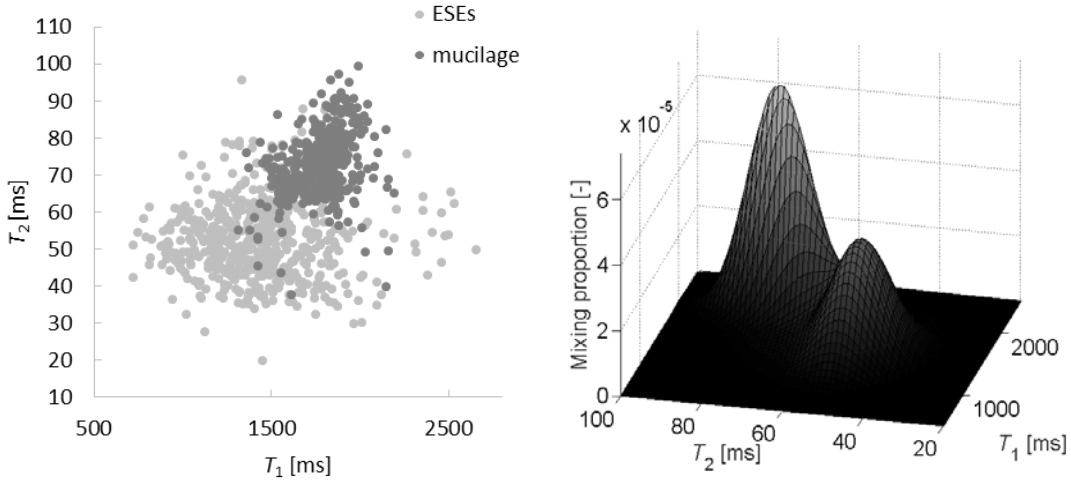

Fig.3. The distribution of the relaxation times T_1 and T_2 in the ESEs and mucilage regions (left); the fitted probability density function (a two-component Gaussian mixture model) of the modeled relaxation times (right)..

Table 1. The estimation of the mean values and standard deviations of the relaxation times from randomly selected pixels and from values determined by distribution function modeling via the two-component GMM.

	Isolated mucilage		Isolated ESEs	
	T_1 [ms]	T_2 [ms]	T_1 [ms]	T_2 [ms]
Sample selection	1763 ± 169	73 ± 8	1435 ± 318	52 ± 10
GMM	1784 ± 124	74 ± 8	1469 ± 324	53 ± 10

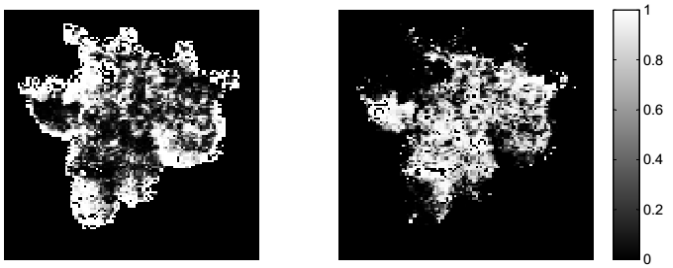

Fig.4. The probability maps of the ESEs (left) and mucilage (right).

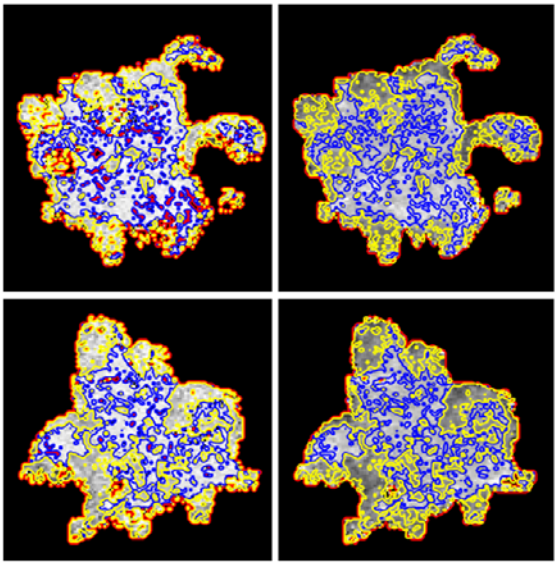

Fig.5. The segmented T_1 and T_2 maps of cultures No. 1 and No. 2. The T_1 maps are shown on the left (top and bottom), while the T_2 ones are presented on the right (top and bottom).

In the case of the axial slices, we expanded our two-component GMM to a three-component one in such a manner that the manually selected pixels in the area of the transition layer from the chosen axial slice were added to the original two-component GMM. As the separation of the transition layer is practically unfeasible, the pixels representing the transition layer in the axial slice were selected manually. The three-component GMM secures the possibility of recognizing, besides the ESEs and mucilage, also the transition layer between the embryogenic tissue and applied substrate. The distribution of the relaxation times for the ESEs, mucilage, and transition layer is shown in Fig.6. (left). The resulting approximation of the three-dimensional (3D) histograms via the three-component GMM can be seen in Fig.6. (right).

The calculated mean values of the relaxation times of the ESEs, mucilage, and transition layer are shown in Table 2. The three-component GMM was successfully applied in the axial slices, where the transition layer is visible. The probability distribution maps for the ESEs, mucilage, and transition layer can be seen in Fig.7. The final segmentation was performed with the same threshold (p = 68.2 %) as in the previous case. The green contour in Fig.8. represents the region of the segmented transition layer.

The relaxometry measurements of the isolated ESEs and mucilage show that these parts of the embryogenic tissue can be well characterized using a classifier created from the relaxation times T_1 and T_2. The relaxation times of the isolated ESEs, mucilage, and the transition layer are indicated in Table 2. The elliptical scattering of the relaxation times (Fig.3.) is caused by the fact that we cannot ensure good separation of these embryogenic tissue parts, and this is especially true of the manually separated pixels of the transition layer (Fig.6.). However, we also need to note that the same MRI sequences were used for both the measurement of the discussed isolated tissue parts and the in situ measurement.

Table 2. The estimation of the mean values and standard deviations of the relaxation time values determined via distribution function modeling with the three-component GMM.

	Isolated mucilage		Isolated ESEs		Transition layer	
	T_1 [ms]	T_2 [ms]	T_1 [ms]	T_2 [ms]	T_1 [ms]	T_2 [ms]
GMM	1784 ± 124	74 ± 8	1469 ± 324	53 ± 10	929 ± 164	32 ± 4.7

After the MRI-based measuring steps, the morphology of the embryogenic tissue was displayed (Fig.9.a), b)) using optical microscopy (an Olympus SZX10 stereo microscope). The sample orientation of the embryogenic tissue is the same as in the MRI measurement (Fig.9.c)). Fig.9. contains a PD-weighted image and the images obtained via the optical microscopy technique. While the former two images show the surfaces of embryogenic tissues No. 1 and No. 2, the latter one exhibits a slice (defined volume) through the inside of embryogenic tissue No. 1. The air bubbles in the culture are clearly visible (the white bold arrows in the PD image). In the PD-weighted image, the high-intensity regions are artefacts due to the different magnetic susceptibilities between the air and the embryogenic tissue; these artefacts do not affect the resulting T_1 and T_2 maps.

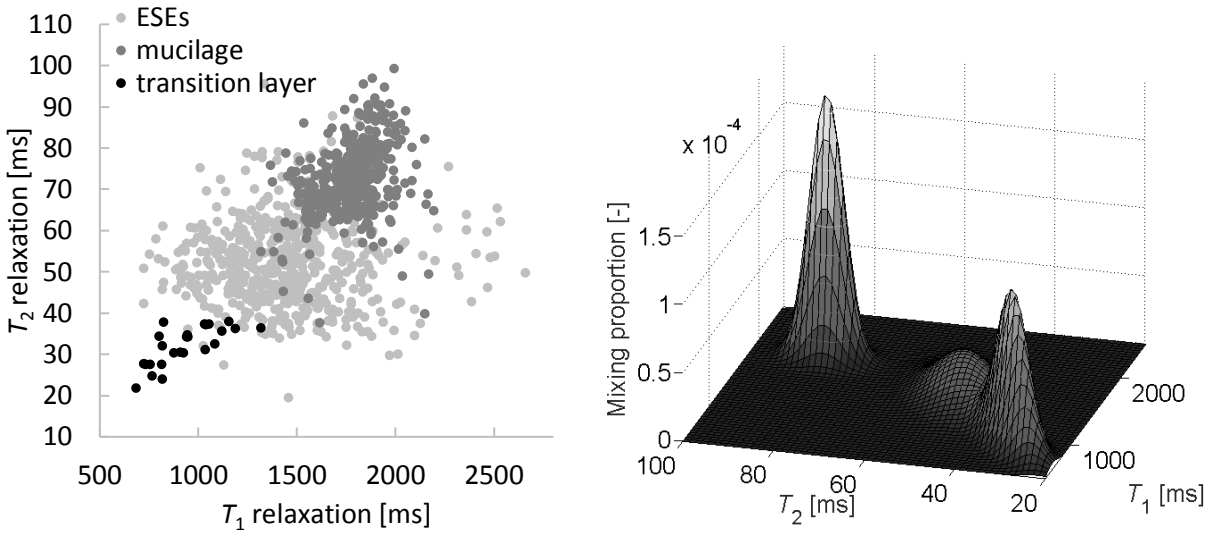

Fig.6. The distribution of the T_1 and T_2 relaxation times in the regions of the ESEs, mucilage, and transition layer (left); the fitted probability density function (a three-component Gaussian mixture model) of the modeled relaxation times (right).

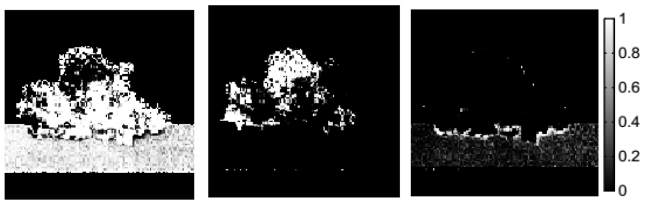

Fig.7. The probability maps of the ESEs (left), mucilage (center), and transition layer (right).

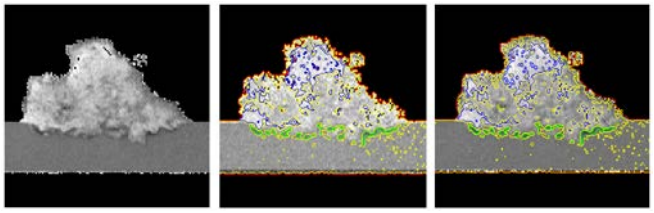

Fig.8. The original T_1 map of the axial slice (left); the segmentation results in the T_1 (centre) and T_2 (right) maps. The green line indicates the transition layer.

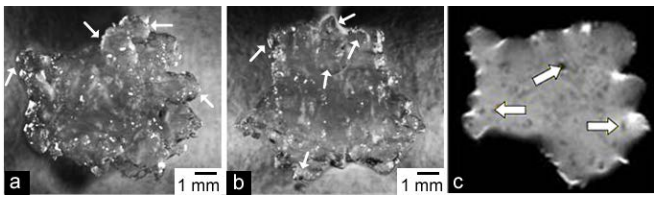

Fig.9. The microscopic images of samples No. 1 (a) and No. 2 (b); the thin white arrows show clusters of the ESEs. The PD-weighted MR image (c) of the ESEs of the Norway spruce (sample No. 1); the bold white arrows indicate the air bubbles.

4. Conclusion and discussion

The embryogenic tissue of a conifer is characterized by the presence of bipolar structures composed of an embryonic part with densely packed embryogenic cells and a suspensor formed by long vacuolated cells [12]. A structural subcellular marker, such as the extracellular matrix surface network (ECMSN), was found to be a characteristic feature for the embryogenic tissue [26], [27]. From the botanical point of view, the ECMSN is plant mucilage. The cell wall of plants consists of dynamic cellular compartments with structural, protective, and growth regulating functions. Plant cell walls, together with cytoskeleton, determine the polarity and control the morphogenesis [28]. The external cell wall is particularly interesting due to its exposure to environmental factors; in this context, let us note that the different cellular responses mediate the adaptation of the plant to changed environmental conditions. One of such responses may lie in the formation of the ECM surface layer or network on the outer cell wall. The secretions are probably one of the factors playing a role in the cell integration and recognition process. The morphogenesis is controlled by particular morphogenic programs within which cell-to-cell communication is critical for the cellular decision-making process. Dostál [29] indicates that growth correlations become more complex and difficult during plant development. It appears likely that, in the course of the embryogenesis, the ECM constitutes an important structural integrity agent.

The role of the ECMSN during morphogenesis remains unclear; however, the cell adhesion, protective function, and coordinating developmental stage have all been explained.[30]. The analysis of the chemical composition of the ECMSN performed with different solvents and enzymes revealed differences between the species and identified the relevant proteins. Other researchers used specific antibodies to identify the AGPs and pectin epitopes in the ECMSN.[31], [30]. Generally, AGPs are plant cell surface macromolecules belonging to the subfamily of hydroxyprolin-rich glycoproteins; they can act as signaling macromolecules and are involved in the vegetative, reproductive, and cellular growth and development [19]. Verdeil et al. [30] indicate that the chemical composition and structural arrangement of the ECMSN on a cell surface play a significant role in morphogenic processes.

The measurement of embryogenic cultures via magnetic resonance imaging is beneficial for embryogenic tissue characterization. In more general terms, the intensity of a PD-weighted image in a voxel is proportional to the amount of ^{1}H nuclei (a quantitative summary of the number of protons per unit tissue) in the measured tissue. The water holding capacity of the AGPs of the ECM may reflect other physiological roles. The AGPs' ability to hydrate may be also important in their capacity to prevent injuries and to resist drying out [17]. For many years, the ECM was dismissed as a relatively inert "ground substance", whose sole function was packing; however, it has now become clear that the ECM is significantly more complex than previously presumed and that the interaction with the surrounding matrix is one of the major elements to control cell behavior. [32].

The results obtained through MRI relaxometry show the possibility of distinguishing between the ESEs, ECMSN (mucilage), and transition layer in an embryogenic tissue; for these recognition purposes, uniform classifiers are applied. The classifiers consist only of the T_1 and T_2 relaxation times. The dispersion of the T_2 relaxation time for the ESEs, mucilage, and transition layer is low compared to the T_1 indicator; thus, the T_2 maps are more advantageous for the actual embryogenic tissue differentiation. The distribution of the ESEs, mucilage, and transition layer was obtained using automatic segmentation. The mucilage (ECMSN) is then distributed unevenly in the embryogenic tissue. Regions with a minimum mucilage volume also appear in the space between the cells (the ESEs). In the case of MR imaging applied to represent an embryogenic tissue, the quantification of the amount of ESEs and mucilage within a voxel is unfeasible.

Relaxometry measurements in combination with the subsequent automatic multi-parametric segmentation (based on the T_1 and T_2 relaxation times) provide non-destructive differentiation between the cells and mucilage in an embryogenic tissue. In the case of contiguous slices, three-

dimensional distribution of the cells and mucilage can be visualized. The function of the transition layer remains unclear; thus, the aim of further investigation is to perform a detailed analysis of the chemical composition and properties of the transition layer between the embryogenic callus and the medium. In a narrower sense, within the given context, we seek to define the effect of the transition layer on the growth and development of the culture. Changes of the relaxation times T_1 and T_2 during cultivation may help us to characterize the chemical and physical changes in the ESEs. Moreover, the times T_1 and T_2 may serve as an indicator of the effect of stress on the developmental somatic embryos in an embryogenic culture in situ. Relaxometry measurements appear to constitute an interesting and useful methodological element in the research into the structure of embryogenic tissues.

ACKNOWLEDGMENT

The research was supported by grants of the Czech Science Foundation (GA14-22777S, GA13-09086S) and by the European Commission and the Ministry of Education, Youth, and Sports (projects No. CZ.1.05/2.1.00/01.0017, LO1212).

REFERENCES

[1] Mac Fall, J.S., Van As, H. (1996). Magnetic resonance imaging of plants. In *Nuclear Magnetic Resonance in Plant Biology*. The American Society of Plant Physiologists, 33-76.

[2] Scheenen, T., Vergeldt, F., Heemskerk, A., Van As, H. (2007). Intact plant magnetic resonance imaging to study dynamics in long-distance sap flow and flow-conducting surface area. *Plant Physiology*, 144, 1157-1165.

[3] Ionenko, I., Anisimov, A., Dautova, N. (2010). Effect of temperature on water transport through aquaporins. *Biologia Plantarum*, 54, 488-494.

[4] Pu, Y., Chen, F., Ziebell, A., Davison, B., Ragauskas, A. (2009). NMR characterization of C3H and HCT down-regulated alfalfa lignin. *BioEnergy Research*, 2, 198-208.

[5] Zulak, K., Weljie, A., Vogel, H., Facchini, P. (2008). Quantitative 1H NMR metabolomics reveals extensive metabolic reprogramming of primary and secondary metabolism in elicitor-treated opium poppy cell cultures. *BMC Plant Biology*, 8, 5.

[6] Lambert, J., Lampen, P., von Bohlen, A., Hergenroder, R. (2006). Two- and three- dimensional mapping of the iron distribution in the apoplastic fluid of plant leaf tissue by means of magnetic resonance imaging. *Analytical and Bioanalytical Chemistry*, 384, 231-236.

[7] Glidewell, S., Möller, M., Duncan, G., Mill, R., Masson, D., Williamson, B. (2002). NMR imaging as a tool for noninvasive taxonomy: Comparison of female cones of two Podocarpaceae. *New Phytologist*, 154, 197-207.

[8] Šupálková, V., Petřek, J., Baloun, J., Adam, V., Bartušek, K., Trnková, L., Beklová, M., Diopan, V., Havel, L., Kizek, R. (2007). Multi-instrumental investigation of affecting of early somatic embryos of spruce by cadmium (II) and lead (II) ions. *Sensors*, 7, 743-759.

[9] Šebánek, J., Sladký, Z., Procházka, S. (1991). *Experimental Morphogenesis and Integration of Plants: Terofal*. 1st Edition. Prague, Czech Republic: Academia; Elsevier.

[10] Dostál, R. (1967). *On Integration in Plants*. 1st Edition. Harvard University Press.

[11] Hřib, J., Vooková, B., Neděla, V. (2015). Imaging of native early embryogenic tissue of Scots pine (Pinus sylvestris L.) by ESEM. *Open Life Sciences*, 10, 285-290.

[12] Šamaj, J., Salaj, T., Matúšová, R., Salaj, J., Takáč, T., Šamajová, O., Volkmann, D. (2008). Arabinogalactan-protein epitope Gal4 is differentially regulated and localized in cell lines of hybrid fir (Abies alba x Abies cephalonica) with different embryogenic and regeneration potential. *Plant Cell Reports*, 27, 221-229.

[13] Neděla, V., Hřib, J., Vooková, B. (2012). Imaging of early conifer embryogenic tissues with the environmental scanning electron microscope. *Biologia Plantarum*, 56, 595-598.

[14] Neděla, V., Hřib, J., Havel, L., Runštuk, J. (2013) Early state of spruce somatic embryos in native state observed using the ESEM and Cryo-SEM. *Microscopy and Microanalysis*, 19 (suppl. 2), 20-21.

[15] Neděla, V., Tihlaříková, E., Hřib, J. (2015). The low-temperature method for study of coniferous tissues in the environmental scanning electron microscope. *Microscopy Research Techniques*, 78 (1), 13-21.

[16] Egertsdotter, U., von Arnold, S. (1995). Importance of arabinogalactan proteins for the development of somatic embryos of Norway spruce (Picea abies). *Physiologia Plantarum*, 93, 334-345.

[17] Clarke, A., Anderson, R.L., Stone, B. (1979). Form and function of arabinogalactans and arabinogalactan-proteins. *Phytochemistry*, 18, 521-540.

[18] Karácsonyi, Š., Pätoprstý, V., Kubačková, M. (1998). Structural study on arabinogalactan-proteins from Picea abies L. Karst. *Carbohydrate Research*, 307, 271-279.

[19] Seifert, G., Roberts, K. (2007). The biology of arabinogalactan proteins. *Annual Review of Plant Biology*, 58, 137-161.

[20] Mikulka, J., Hutova, E., Korinek, R., Marcon, P., Dokoupil, Z., Gescheidtova, E., Havel, L., Bartusek, K. (2016). MRI-based visualization of the relaxation times of early somatic embryos. *Measurement Science Review*, 16, 54-61.

[21] von Arnold, S. (1987). Improved efficiency of somatic embryogenesis in mature embryos of Picea abies (L.) Karst. *Journal of Plant Physiology*, 128, 233-244.

[22] Havel, L., Durzan, D. (1996). Apoptosis during diploid parthenogenesis and early somatic embryogenesis of Norway spruce. *International Journal of Plant Sciences*, 157, 8-16.

[23] Vlašínová, H., Mikulecký, M., Havel, L. (2003). The mitotic activity of Norway spruce polyembryonic culture oscillates during the synodic lunar cycle. *Biologia Plantarum*, 47, 475-476.

[24] Bloch, F. (1946). Nuclear Induction. *Physical Review*, 70, 460-473.

[25] Xiong, T., Zhang, L., Yi, Z. (2016). Double Gaussian mixture model for image segmentation with spatial relationship. *Journal of Visual Communication and Image Representation*, 34, 135-145.

[26] Dubois, T., Dubois, J., Guedira, M., Diop, A., Vasseur, J. (1992). SEM characterization of an extracellular matrix around somatic proembryos in roots of Cichorium. *Annals of Botany*, 70, 119-124.

[27] Šamaj, J., Bobák, M., Blehová, A., Krištin, J, Auxtová-Šamajová, O. (1995). Developmental SEM observations of an extracellular matrix in embryogenic calli of Drosera rotundifolia and Zea mays. *Protoplasma*, 186, 45-49.

[28] Baluška, F., Šamaj, J., Wojtaszek, P., Volkmann, D., Menzel, D. (2003). Cytoskeleton-plasma membrane-cell wall continuum in plants. Emerging links revisited. *Plant Physiology*, 133, 482-491.

[29] Dostál, R. (1959). *O celistvosti rostliny (On Integration in Plants).* Prague, Czech Republic: SZN. (in Czech)

[30] Verdeil, J., Hocher, V., Huet, C., Grosdemange, F., Escoute, J., Ferrière, N., Nicole, M. (2001). Ultrastructural changes in coconut calli associated with the acquisition of embryogenic competence. *Annals of Botany*, 88, 9-18.

[31] Šamaj, J., Baluška, F., Bobák, M., Volkmann, D. (1999). Extracellular matrix surface network of embryogenic units of friable maize callus contains arabinogalactan-proteins recognized by monoclonal antibody JIM 4. *Plant Cell Reports*, 18, 369-374.

[32] Davies, J. (2001). Extracellular matrix. In *Encyclopedia of Life Sciences*. Nature Publishing Group.

Received August 23, 2016.
Accepted January 25, 2017.

MEASUREMENT SCIENCE REVIEW, **17**, (2017), No. 1, 27-36

DE GRUYTER OPEN

MEASUREMENT SCIENCE REVIEW

Journal homepage: http://www.degruyter.com/view/j/msr

ISSN 1335-8871

Measuring Light Air Ions in a Speleotherapeutic Cave

Z. Roubal[1], K. Bartušek[2], Z. Szabó[1], P. Drexler[1], J. Überhuberová[3]

[1]*Department of Theoretical and Experimental Engineering, Faculty of Electrical Engineering and Communication, Brno University of Technology, Technická, 3082/12, 61600, Brno, Czech Republic, roubalz@feec.vutbr.cz, szaboz@feec.vutbr.cz, drexler@feec.vutbr.cz*

[2]*Institute of Scientific Instruments, Academy of Sciences of the Czech Republic, Kralovopolska, 147, 61200, Brno, Czech Republic, bar@isibrno.cz*

[3]*Children's Speleotherapy Medical Centre, South Moravian Children's Medical Facilities (public benefit organisation), Ostrov u Macochy, 389, 67914, Ostrov u Macochy, Czech Republic*

The paper deals with a methodology proposed for measuring the concentration of air ions in the environment of speleotherapeutic caves, and with the implementation of the AK-UTEE-v2 ionmeter. Speleotherapy, in the context of its general definition, is the medical therapy that utilizes the climate of selected caves to treat patients with health problems such as asthma. These spaces are characterized by the presence of high air humidity and they make extreme demands on the execution of the measuring device, the Gerdien tube (GT in the following) in particular, and on the amplifier electronics. The result is an automated measuring system using a GT with low-volume air flow, enabling long-term measuring of air ion concentration and determination of spectral ion characteristics. Interesting from the instrumentation viewpoint are the GT design, active shielding, and execution of the electrometric amplifier. A specific method for the calculation of spectral ion characteristics and the mode of automatic calibration were proposed and a procedure of automatic measurement in the absence of attendants was set up. The measuring system is designed for studying and long-term monitoring of the concentration of light negative ions in dependence on climatic conditions and on the mobility of ions occurring in the cave.

Keywords: Speleotherapy, air ions, Gerdien tube, climatology.

1. INTRODUCTION

Measuring the properties of air ions and their concentration is a hot topic currently being solved at several scientific workplaces [1]-[6]. Tammet describes the working principle of measuring devices with a GT (Gerdien tube) in a survey publication [7]. Another publication, [8], [9], focuses on the evaluation of the mobility spectrum of air ions, inclusive of a data analysis with ion size interpretation. The proposed spectrometers are mostly of the stationary type, suitable for meteorological stations designed for measuring in an air-conditioned building [10], [11]. Some interesting spectrometers and GT for meteorological purposes are given in [1], [10]-[14]. From the viewpoint of determining the mobility spectrum of air ions, the measurement using a GT with a segmented internal electrode is more rapid but less accurate.

In a number of medical research projects, reported for example in [15]-[19], it has been proved that light negative ions have a positive effect on human health and their lack results in fatigue, health problems, and reduced performance at work. For example, special ionizers were tested that employ the stimulation of plants placed in a salt solution with high electric voltage [20], and their influence and effect on the tracheas of laboratory (sewer-) rats were evaluated, together with an analysis of the state of their blood. Measuring the concentration of air ions is widely applied in monitoring the degree of air pollution, hygiene checks at workplaces, health therapy – speleotherapy [21]-[23], in the study of electric phenomena in the atmosphere and, topically, in forecasting earthquakes [24], [25] or other weather anomalies. Aplin [26] describes the effects of atmospheric electricity on its surroundings and the manner it is generated in the troposphere. The area of interest extends into astrophysics, with focus on the exploration of atmospheric discharges and ionization on gaseous planets of the solar system [27].

All these applications work with data on the concentration of light air ions, with the mobility spectrum of ions measured with a relevant accuracy and with metrologically properly obtained data. It is therefore indispensable to set the measuring process and the measuring methodology such that analyses and evaluations can be performed on the derived and monitored phenomena.

Currently, a method for measuring the concentration of air ions using a GT is widely used. One of the greatest advantages of this method is the possibility of evaluating the

DOI: 10.1515/msr-2017-0004

mobility spectrum (spectral characteristics) of air ions from the measurements carried out [28]. Other methods such as those given in [28] and [15] lack this possibility.

The measurement of air ions in speleotherapeutic cave conditions is burdened with great uncertainties. These are primarily due to the high relative humidity in the cave (100 %), slow air flow with pronounced ion fluctuation under strong ionization of air by radon. A serious disadvantage of the air ion meters is that in an environment with high relative humidity they do not work or they only measure for a limited, very short period of time. The measuring ambiguity is also greatly affected by the presence of persons and by their motion in the cave during therapy and measurement.

The present work is concerned with a methodology of air ion measurement to be applied in speleotherapeutic caves. These spaces are characterized by the presence of high air humidity and they make extreme demands on the execution of the measuring device, the GT in particular, and on the amplifier electronics. The result is an automated measuring system using a GT with a low-volume air flow, enabling long-term measurements of air ion concentration and determination of spectral ion characteristics. The measuring system is designed for the study of and search for varied concentration of light negative ions in dependence on climatic conditions, and the mobility of ions occurring in the caves.

2. Methodology of ion concentration measurement

Problems of the methodology of measuring air ions with the aid of a GT require a complex solution including several mutually complementary areas.

To eliminate uncertainties in the measurement of ion concentration it is necessary to design and experimentally verify an appropriate conception of the measuring system with a GT for use in therapeutic cave spaces. These spaces are characterized by the presence of high air humidity and thus they make extreme demands on the execution of the measuring device, in particular the GT and the electronics, inclusive of the amplifier.

The mutual relationship between the concentrations of positive n_+ and negative n_- ions is expressed by unipolarity coefficient P.

$$P = \frac{n_+}{n_-} \tag{1}$$

3. Speleotherapeutic caves

In a speleotherapeutic cave, child patients suffering from bronchial asthma are treated. According to medical reports, as many as 10-15 % of children in the Czech Republic (CR) [29] suffer from this disease; thus it is a problem with societal impact. In CR, asthma treatment using speleotherapy is practised in the Eden Zlaté Hory centre in the Jeseníky Mountains, and also in the child sanatorium in Ostrov u Macochy, where the measurement using the proposed methodology was performed. The treatment takes place in the Císařská jeskyně, which was specially adapted for purposes of speleotherapy. It is a cold cave of the karst type.

The environmental theory currently characterizes the healing effects of speleotherapeutic caves by a set of components, factors and processes of the cave endo-environment and their clinically verifiable interactions with the human body. The confirmed effects that influence the patient's state of health can be characterized by the following parameters [29]:

- constant cave temperature, ranging from 7 – 8 °C;
- high relative air humidity, attaining 100 % for most of the year;
- high concentration of light negative and positive ions, generated by radionuclides contained in limestone (uranium, thorium and radioactive potassium); The unipolarity coefficient approaches P=1, and the related mobility is k>1,28 $cm^2 \cdot V^{-1} \cdot s^{-1}$.
- content of calcium and magnesium ions in aerosol;
- modest air flow;
- low dust content, absence of allergens and bacteria.

4. Electric field distribution in GT

Of the greatest importance for the metrological properties of the method with GT is the distribution of electric field. To assess the behaviour of air ions during their passage through GT, a simulation of electric field distribution inside and outside GT was conducted using the finite element method (FEM) [30]-[32]. The field must not markedly influence electric potential in the space being measured. In the space in front of GT the electrostatic field should draw in ions without the formation of electrostatic lenses. Within the given context, we first of all outline the results for the most advantageous arrangement of the electrostatic field as related to the measurement; this particular option was then chosen for our measuring system. The measuring configuration is illustrated in Fig.1. and Fig.2. When three electrodes (inner, outer, and shielding) are used, there are four possible variants, which differ depending on which electrode is earthed. From the simulation results the variant with the earthed outer electrode was chosen.

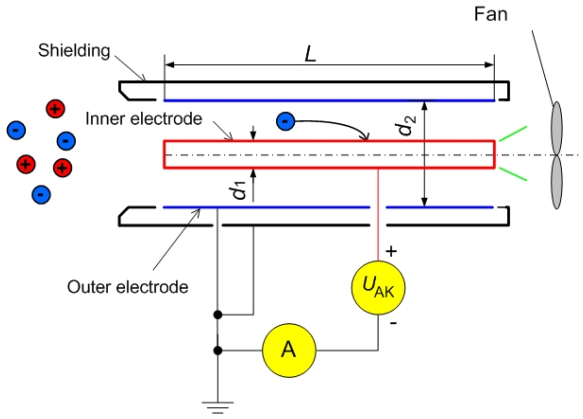

Fig.1. Measuring configuration of the optimal chosen variant for negative ions.

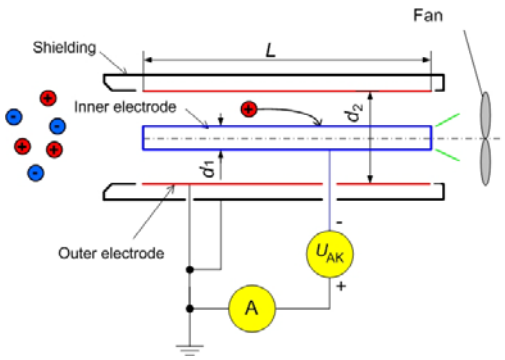

Fig.2. Measuring configuration of the optimal chosen variant for positive ions.

The simulation results in section and near the GT inlet as given in Fig.3. confirm a low effect on the intensity of electric field *E* in the space being measured, and appropriate suction of air ions without the formation of an electrostatic lens on the input.

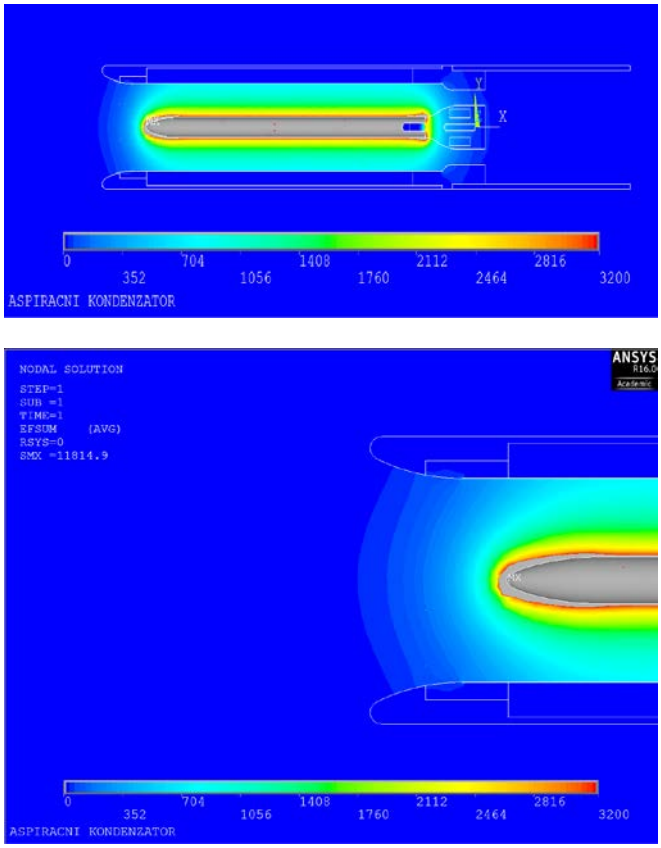

Fig.3. Distribution of intensity *E* in GT section (up) and on the GT input (down), with the scale limited to 3200 V/m (valid for both negative and positive ions). The relevant polarization voltage corresponds to U_{AK}=25 V.

The electric field intensity increases in the direction of the inner collecting electrode. There is no deformation of the trajectory of air ions and no drop in the measured concentration of air ions caused by the change in the polarization voltage U_{AK}. Near the inner electrode edges the drop in intensity *E* is not compensated for by edge effects, and the deviation ΔE may reach as much as -15 % from the ideal dependence. At the end of the inner electrode there are divergences in the FEM due to the sharp edge, and the intensity *E* is assumed to be higher than in other variants of electrode earthing. For 90 % of the space between the inner and the outer electrode the ideal distribution of electric field holds, similar to the cylindrical capacitor. Thus, there is no drop in the measured concentration of air ions that would still be dependent on the magnitude of the voltage U_{AK}. This property can be decisive for the measurement of ion fields in small constrained spaces. The result of the simulation is the proposal of suitable dimensions and distribution of potentials in GT (Table 1.).

In their relevant articles, [3], [14], Aplin and Kolarž connect the inner electrode to the potential of the earth, whereas the polarization voltage is led to the outer electrode. This approach is simpler due to the guarding principle used in the electrometric amplifier; however, as shown by the simulation, the solution can also be considered inconvenient in terms of the distribution of the electromagnetic field. Fig.4. represents the configuration for the measurement of negative ions; in measuring positive ions, positive voltage is led to the outer electrode.

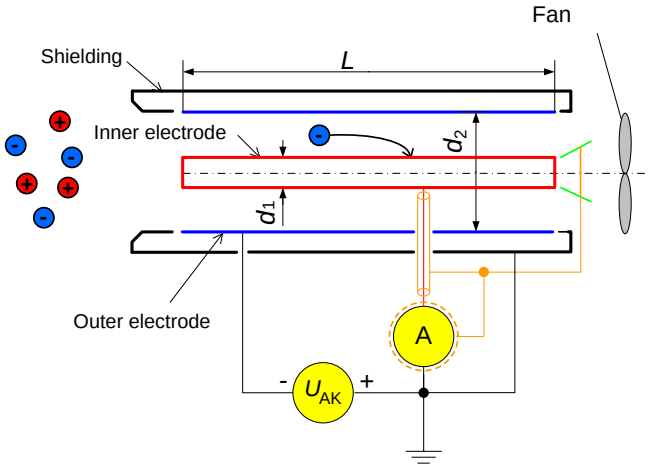

Fig.4. Measuring configuration utilized by Aplin and Kolarž for negative ions.

The distribution of intensity *E* is represented in Fig.5., which shows that the necessary shielding coat of the GT on the potential of the earth causes an electrostatic lens to form in front of the inner electrode at the inlet of the GT. The lens then prevents a portion of the ions from reaching the collecting electrode, and their concentration measured in this variant is thus lower than that found in the measured space. The detailed distribution of intensity *E* at the mouth of the GT is shown in Fig.5.

Ions are drawn into the GT by a ventilator. The ventilator motor must be magnetically shielded in order not to influence the ion trajectory in GT. Shielding is provided by a ferrite cylinder surrounding the motor. Commutator motors are a source of considerable interference and are not suitable for the proposed measurement.

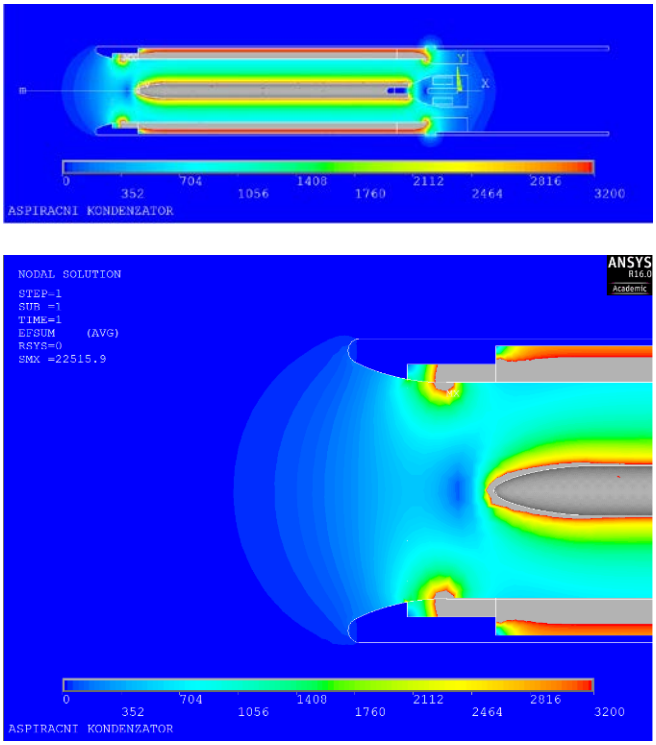

Fig.5. Distribution of intensity E in GT section (up) and on the GT input (down), with the scale limited to 3200 V/m (valid for both negative and positive ions). The relevant polarization voltage corresponds to U_{AK}=25 V.

Table 1. Properties of AK-UTEE-v2 [33].

	AK-UTEE
Diameter d_2 [mm]	38
Diameter d_1 [mm]	12
Inner electrode length L [mm]	160
Flow velocity v_x [m.s^{-1}]	2.1
Volume flow rate of air M [cm^3.s^{-1}]	2140
Capacitance C_{AK} [pF]	7.7
Limit mobility km [cm^2.V^{-1}.s^{-1}]	$\frac{24.5}{U_{AK}}$
Voltage U_{AK} required for measuring light ions with the mobility k > 1.7 cm^2.V^{-1}.s^{-1}	14.4

In our GT, the relationship between the concentration of air ions n and the measured current I corresponds to

$$n = 2140 \cdot I \qquad (2)$$

where the current I is expressed in pA, and n in cm^3.s^{-1}.

5. Conception of electrometric amplifier

Much attention needs to be paid to the measurement of very small currents of the order of 10^{-12} to 10^{-15} A. It is necessary to choose an electrometric amplifier design with minimum noise and to increase the insulation resistance of GT via employing a relay for range switching and using active shielding. It is good to characterize the effect of active shielding on the pulse response of a change in the concentration of air ions [34].

In view of the very low currents being measured it is necessary to eliminate the measuring cables and interfering electric and magnetic fields. A special electrometric amplifier is located as close to the GT collecting electrode as possible and is shielded from outer electromagnetic fields [34]. Feedback connection of the operational amplifier with an electrometric feedback resistor was chosen. This connection exhibits lower noise and it also filters the measured current data. The fundamental connection of electrometric amplifier showing the effect of input quiescent current i_B- and input residual voltage u_{OS} is given in Fig.6. An OPA129 operational amplifier was used in the electrometric amplifier. Table 2. gives the values of equivalent scheme elements for AK-UTEE-v2.

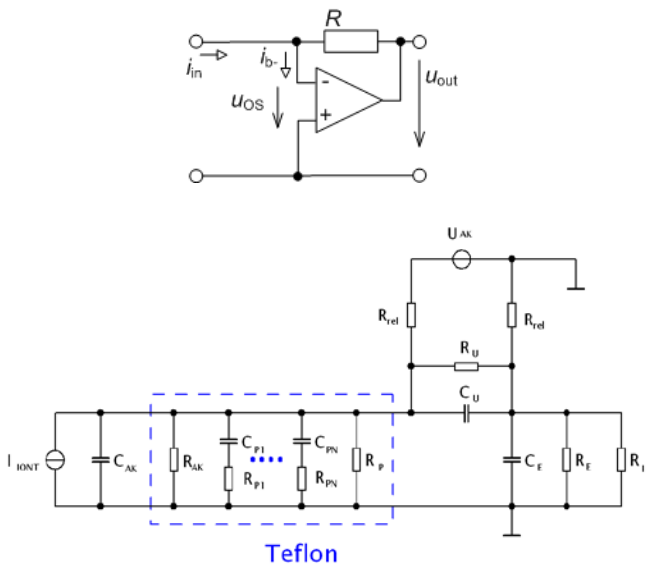

Fig.6. Fundamental connection of electrometric amplifier (top) and equivalent scheme of the AK-UTEE-v2 system (bottom).

Table 2. Properties of AK-UTEE-v2 [33].

AK-UTEE		
C_{AK}	7.7 pF	capacitance of GT
R_{AK} || R_P	5000 TΩ	leakage resistance of GT and Teflon bushing
C_{P1}, R_{P1}	0.7 pF, 40 TΩ	RC element modelling the Teflon DA
C_U, R_U	1 μF, 100 TΩ	polarization capacitor with leakage resistance
C_E	3 pF	capacitance of the lead to sensing resistor
R_E	1000 TΩ	leakage resistance of the lead to sensing resistor
R_{REL}	100 TΩ	leakage resistance of charging relays
R_I	10 kΩ	input resistance of electrometric amplifier
U_{AK}	25 V	source for polarization capacitor charging

The source of polarization voltage was implemented by a polarization capacitor C_U [34]. During the measurement, it is charged at regular intervals to a polarization voltage U_{AK}. While charging, the measurement is interrupted and, using a relay (a special, custom-made relay developed at DTEEE, with a Teflon skeleton and high-quality reed contacts A46), the capacitor C_U is switched over to controllable voltage source via both terminals. The purpose of using the capacitor is to obtain minimum leakage currents. The period of a new charging of C_U should be 4000 s and, if measuring in a cave, up to 50.10^5 s [34]. With longer periods of charging the C_U, significant errors may appear when measuring the saturation characteristics.

6. ACTIVE SHIELDING

An important problem when measuring in an environment with high air humidity is the appropriate earthing of GT that will eliminate the effect of electrostatic fields near the measuring device. In simulations using the FEM the effect of earthing can be examined by applying an interference potential to the outer electrode and determining its effect on the results of measuring the concentration of air ions for different configurations.

The selected configuration does not enable us to employ a shield clamp in the electrometric amplifier to facilitate active shielding; we therefore designed a novel, unique solution.

Since with the earthed outer GT electrode the classical active shielding cannot be applied, active shielding with an auxiliary capacitor C_{AS} was proposed (Fig.7.). At the beginning of the measurement, the C_{AS} capacitor together with the polarization capacitor C_E is charged to the voltage U_{AK}. One of its pins is earthed, the other is connected to the shielding ring of the bushing shielding and the shielding bevelled ring of the inner electrode Teflon holder. After disconnecting the polarization voltage source, the C_{AS} capacitor is actively shielding the inner electrode.

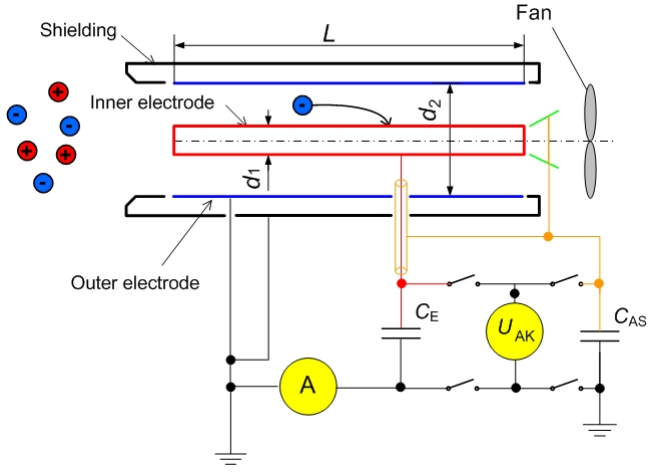

Fig.7. Schematic illustration of active shielding.

The reason for using a further capacitor is that the polarization voltage U_{AK} can attain a value of up to 60 V and it is necessary to use a further amplifier with a higher supply voltage. The pins of active shielding cannot be connected directly to the source of polarization voltage because its implementation is unipolar and its polarity is changed via a relay on the output. The C_{AS} capacitor is discharged by leakage current according to the relation

$$I_{svod} = \frac{U_{AK}}{R_{AK} \parallel R_P} \tag{3}$$

The error in the concentration measured is then caused by the voltage difference between the C_E and C_{AS}, given by their different ways of discharging during the measuring process. Experimental measurements revealed that a period of 30 min was sufficient to recharge the two capacitors to the polarization voltage.

7. MEASURING PROCEDURE

A properly chosen measuring procedure will enable eliminating the effect of the electrostatic field of the space being measured, the leakage current of GT, the effect of earthing, and the dynamics of the change in time of the concentration of air ions. The proposed automated measuring system AK-UTEE-v2 (Fig.8.) has an electrometric amplifier located on the GT shielding jacket. The block diagram of the proposed equipment is shown in Fig.9. The electrometric amplifier includes a polarization capacitor, which is periodically charged from a HV source. The electrometric amplifier is zeroed with the GT ventilator off, using a D/A converter. The value measured on the output of electrometric amplifier is digitized by a 16-bit A/D converter and processed in an AVR microcontroller. In automatic measurement the algorithm is controlled by the microcontroller, which in addition to providing the measuring mode also saves the measuring results in a FLASH memory or transfers them into a PC via USB interface in the case of manual measurement. The conception of the meter allows automatic measurement of ion concentration in the absence of attendants and periodic automatic compensation of the electrometric amplifier zero.

Fig.8. Two AK-UTEE-v2 measuring systems for measuring negative and positive ions.

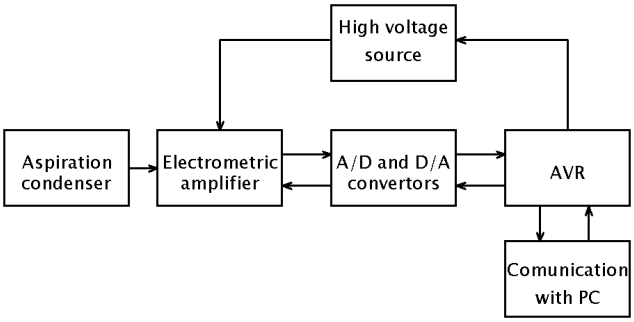

Fig.9. Block diagram of AK-UTEE-v2.

8. CALCULATION OF MOBILITY SPECTRUM OF AIR IONS

The processing of the values measured and the calculation of the spectral characteristics of air ions must suppress noise, and the proposed algorithm should be little sensitive to the time fluctuation of the concentration of air ions.

The saturation characteristic is the dependence of the measured electric current flowing through GT on the polarization voltage U_{AK} (schematic in Fig.1.). In [28] and [34] Israël derived a relation for the number of ions with greater mobility than the limit mobility k_m for a given polarization voltage U_{AK}.

$$\int_{k_m}^{\infty} n(k)\,\mathrm{d}k = Z - U_{AK}\frac{\mathrm{d}Z}{\mathrm{d}U_{AK}} \tag{4}$$

where n is the number of ions, k is the ion mobility, and Z is an auxiliary variable according to (4).

$$Z = \frac{I}{\mathrm{q}\cdot M} \tag{5}$$

The characteristic Z is graphically illustrated in Fig.8. To establish the amount of ions in the mobility interval (k_{m1} to k_{m2}) the first derivatives are obtained for two polarization voltages U_{GT}, and the point of intersection with the axis y is found, Fig.10.

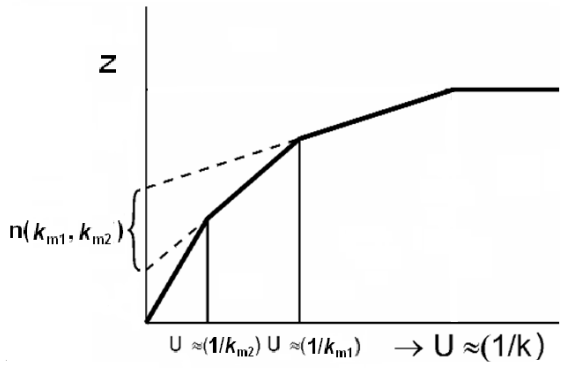

Fig.10. Example of establishing the mobility spectrum of air ions (adjusted according to [28]).

The result of the calculation of ions in the interval $k_{m1}<k_{m2}$ is given by the relation

$$n(k_{m1}, k_{m2}) = \int_{k_{m1}}^{\infty} n(k)\,\mathrm{d}k - \int_{k_{m2}}^{\infty} n(k)\,\mathrm{d}k \tag{6}$$

A new method was therefore proposed for the calculation of the spectral characteristic. The ion spectrum was calculated via fitting the saturation characteristic with the sum of several functions G (7), using the least squares method. The function G expresses the number of measured ions with different mobility values and it is

$$G = \begin{cases} \dfrac{C_{AK}\cdot U_{AK}\cdot k}{\varepsilon_0} & \text{for } k < k_m \\ M & \text{for } k \geq k_m \end{cases} \tag{7}$$

For a continuous spectrum, an infinite number of such functions would be necessary. According to experimental results, it is in most cases sufficient to consider a spectrum of two to three principal mobility values of ions. The saturation characteristic should be a monotonously rising function [36]. The calculation of the mobility spectrum of air ions from relation (6) is highly sensitive to fluctuation and noise [37], [38]. One point of the saturation characteristic must therefore be obtained from the average of 100 measured values of light ion concentration. Still, it is affected by large measuring uncertainties. The proposed method does not perform the first derivative of the saturation characteristic measured and does not emphasize fluctuation in the saturation characteristic waveform measured. This method markedly reduces the effect of undesirable noise and instability of the concentration of light negative ions in a space.

For the numerical method of least squares the function lsqcurvefit was made use of in the MATLAB environment. The saturation characteristic was measured at regular time intervals of 2 s. To eliminate the effect of ventilator start, 125 values of current were measured, with the first 25 measured values not taken into consideration. Measuring one point of the saturation characteristic took 250 s. Subsequently, the ventilator was turned off, followed by measuring 25 values with the ventilator off. Measuring the whole of the saturation characteristic takes 2.5 hours. During this period there is no marked change in the cave temperature (8.1 °C) and relative humidity (it usually reached 100 % RH). The saturation characteristic can therefore be used for a representative description of the mobility of air ions in a cave.

The resultant conversion of saturation characteristic (Fig.11.a)) for AK-UTEE-v2 is given in Fig.11.b). An advantage of this procedure is that in spite of the significant type A uncertainty for U_{AK} = 14 V, the function was fitted correctly. The obtained results correspond to the common mobility spectra shown in several studies, such as [7]; specific are high mobility ions 13.7 $cm^2 \cdot V^{-1} \cdot s^{-1}$.

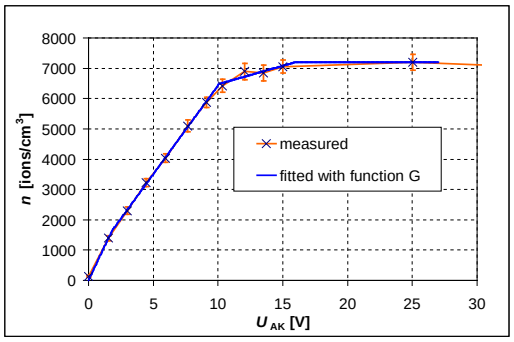

a)

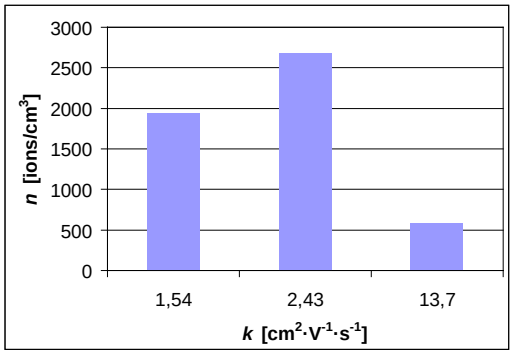

b)

Fig.11. a) measured and approximated saturation characteristics, b) obtained mobility spectrum.

9. RESULTS AND DISCUSSION

To test the correct function of AK-UTEE-v2, a comparative measurement was conducted with the device AK MGK-01 (Kathrein) as a reference apparatus, which is used in the National Institute of Public Health in Prague. AK MGK-01 contains a high-quality electrometric modulation amplifier AD310K. It is employed to verify the concentration of air ions generated by ionizers, and to assess the ion atmosphere at workplaces. Since there was no shielded Faraday chamber available at NIPH, the comparative measurement was conducted in a room designed for ionizer testing. The reference ionizer was placed on a desk covered with a conductive and earthed surface. Both measuring devices were placed on desks with identical surfaces (Fig.12.).

Within the initial step, carried out in Prague on Nov. 2, 2011, we compared the performance obtained at two different distances from the ionizer; the established correction coefficient corresponded to K=1.47. In the subsequent measurement, we used the direct output of the ionmeter, and the related voltage was measured with an Agilent 34401A multimeter.

The measurement on Feb. 21, 2012, was conducted twice, for distances of 1, 1.5 and 2 m from a BIV-07 ionizer; the measurement was not affected by attendants' motion. The relationship between the concentrations measured with the UTEE and the MGK-01 ionmeters is outlined in Fig.12. In addition, due to the longer time constant of the filtering integration circuit in AK MGK-01, the fluctuations in the air ion concentration caused by the instability of the reference ionizer are shifted. Turning off the AK-UTEE-v2 ventilator did not change the AK MGK-01 data. A similar check was performed by disconnecting the supply of AK MGK-01, the AK-UTEE-v2 did not change either. The two measuring systems did not affect each other.

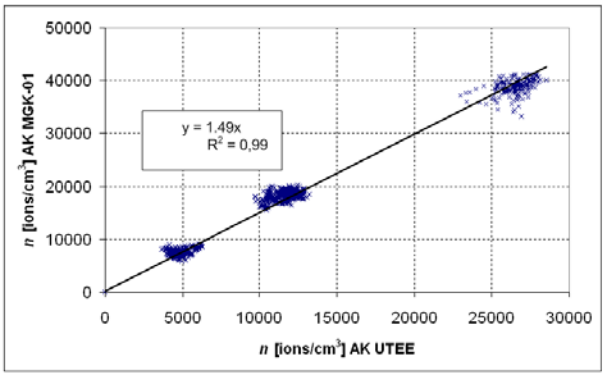

Fig.12. Comparison of measured waveforms from AK-UTEE-v2 and AK MGK-01 (at time 600 s the AK-UTEE-v2 ventilator was turned off) at a distance of 1.5 m from BIV-07 ionizer (top), position of both devices during measurement (down).

Table 3. Comparison of AK-UTEE-v2 and AK-MGK-01, Feb. 21, 2012.

Distance from ionizer	AK-UTEE-v2	AK-MGK-01
[m]	[ions/cm^3]	[ions/cm^3]
1.0	26700 ± 900	38800 ± 1400
1.5	14400 ± 600	18000 ± 1000
2.0	5350 ± 610	8140 ± 1000

Table 3. gives the measured air ion concentrations and their select standard deviations for AK-UTEE-v2 and AK-MGK-01. The air ion concentration was obtained from the average of measured values at times of 100 to 500 s. The chosen measuring interval was 1 s. Fig.12. shows a comparison of 2,000 measured values in both ionmeters. From the regression curve, we established the correction coefficient of K=1.49.

The described new AK-UTEE-v2 system will enable long-term measurement in caves. An example of 7-day measurement in the area of Moravian Karst – Císařská jeskyně, the Nagel Dome, employed for speleotherapy (temperature 8.1 °C, absolute pressure 980 hPa, relative humidity h = 100 %) is given in Fig.13. During the

therapeutic stay a group of 30 children is divided into two halves, with one half sleeping in the 'couch sector', the other playing in the Nagel Dome (usually referred to as playroom). The children come to the cave at 1 p.m. and leave at 4 p.m., swapping their roles in the middle of the stay.

The changes in time of the insulation resistance R_i can be interpreted as l/*f* noise affecting the measured concentration of light ions. The effect of R_i can be suppressed via automatic compensation of the GT zero, which is done periodically every half-hour. During this period the polarization capacitor does not get markedly discharged and the value of the GT leakage current does not change either. Due to the application of this principle, the measurement can proceed for up to one week.

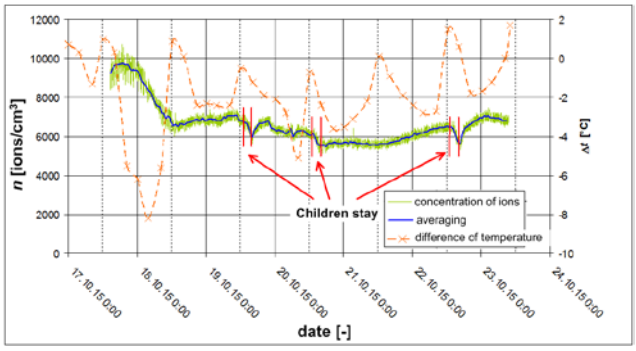

Fig.13. Measuring in cave (top) and the time dependence of concentration of light negative ions in the course of a week, together with the respective temperature difference between cave interior and cave surroundings (down).

The automatic measurement used when measuring the concentration of air ions in a cave is an absolute measurement. In differential measurement, an absolute identity of the two GTs is assumed and unknown distribution of electrostatic field in the space being measured affects the measuring accuracy. In the absolute measurement of the concentration of air ions using one GT the measurement is affected, apart from the required concentration of light air ions, also by: a) electrostatic field in the space measured, b) fluctuations in the GT leakage current caused by dirty insulant surface or phenomena related to dielectric absorption, c) GT contamination by radioactive substances, d) electrometric amplifier noise, in particular its low-frequency component l/*f*. To eliminate the above effects, a new methodology of absolute measurement was proposed for the AK-UTEE-v2 system. Even with the ventilator off, GT measures the residual current which is the result of the electrostatic field of the ionizer when ions move by diffusion from the ionizer tip to the collecting electrode. GT is therefore zeroed with the ion generator on.

The resultant saturation characteristic is obtained by subtracting from each measured value the value of the current when the ventilator is off. Furthermore, one measurement is performed with zero polarization voltage U_{AK} in order to eliminate the effect of electrostatic field in the space measured. It is assumed that the electrostatic field distribution does not markedly change in time. After removing the l/f noise, it is necessary to periodically zero the electrometric amplifier. This will suppress the change in the GT leakage current caused by impurities and potential aqueous film, and also the effect of temperature on the input quiescent current of the operational amplifier.

CONCLUSION

The above-described measuring system AK-UTEE-v2 enables long-term measuring of the concentration of air ions in the environment of speleotherapeutic caves. It operates on the familiar principle of measuring the current flowing through a GT, whose electric field draws in air ions. For long-term measuring of the concentration of ions in humid environment (more than 7 days) a specific measuring procedure is proposed consisting of regular measurements of leakage currents, and their application in the automatic calibration mode. The procedure used in automatic measurement enables long-term measuring and elimination of measuring errors caused by the presence of attendants. Interesting from the instrumentation viewpoint are the low-volume air flow, GT design, unique active shielding, and appropriate connection of electrometer amplifier.

Since obtaining a defined concentration of air ions is very problematic, experimental comparative measurement was performed on the AK-UTEE-v2 and AK MGK-01 (Kathrein) systems, the latter being used by the National Institute of Public Health in Prague. Compared with the AK MGK-01 system, the AK-UTEE-v2 system measures a lower value of ion concentration with a lower standard deviation, with the average value of correction coefficient K_{ion} = 1.49.

Unlike other applicable systems, [3], [4], [5], [14], the AK-UTEE-v2 was designed to facilitate more advantageous distribution of the electrostatic field in the mouth of the condenser; such an arrangement enables us to measure the saturation characteristics in a more accurate manner and to exploit these in computing the air ion mobility spectrum. In this context, for example, a relevant paper by Kolarž [40] shows the typical deformation of saturation characteristics, most probably caused by an inappropriate measuring configuration (Fig.4.). A very beneficial property of the GT consists in the low volumetric flow rate, whose effect on the sensitive environment of the cave is negligible.

The measuring system exhibits good qualities suitable for the study and long-term monitoring of the concentration of light negative ions in dependence on climatic conditions, and of the mobility of ions occurring in speleotherapeutic caves.

ACKNOWLEDGMENT

This work was supported by a grant from the Ministry of Education, Youth and Sports of the Czech Republic (LO1212), the research described in this paper was supported by Czech Science Foundation under grant No. 13-09086S.

REFERENCES

[1] Hörrak, U. (2001). *Air ion mobility spectrum at a rural area*. PhD thesis, University of Tartu, Estonia.

[2] Aplin, K.L., Harrison, R.G. (2001). A self-calibrating programable mobility spectrometer for atmospheric ion measurements. *Review of Scientific Instruments*, 72 (8), 3467-3469.

[3] Aplin, K.L., Harrison, R.G. (2000). A computer-controlled Gerdien atmospheric ion counter. *Review of Scientific Instruments*, 71 (8), 3037-3041.

[4] Harrison, R.G., Aplin, K.L. (2000). A multimode electrometer for atmospheric ion measurements. *Review of Scientific Instruments*, 71 (12), 4683-4685.

[5] Harrison, R.G., Aplin, K.L. (2007). Water vapour changes and atmospheric cluster ions. *Atmospheric Research*, 85 (2), 199-208.

[6] Hirsikko, A., et. al. (2011). Atmospheric ions and nucleation: A review of observations. *Atmospheric Chemistry and Physics*, 11, 767-798.

[7] Tammet, H., Kulmala, M. (2005). Simulation tool for atmospheric aerosol nucleation bursts. *Journal of Aerosol Science*, 36 (2), 173-196.

[8] Harrison, R.G., Tammet, H. (2008). Ions in the terrestrial atmosphere and other solar system atmospheres. *Space Science Reviews*, 137 (1-4), 107-118.

[9] Grabarzyk, Z. (2001). Frequency characteristic of an aspiration integrating small ion counter with a shielded collector. *Journal of Electrostatics*, 51-52, 284-289.

[10] Tammet, H. (2006). Continuous scanning of the mobility and size distribution of charged clusters and nanometer particles in atmospheric air and the Balanced Scanning Mobility Analyzer BSMA. *Atmospheric Research*, 82 (3), 523-535.

[11] Mirme, A., Tamm, E., Mordas, G., Vana, M., Uin, A.J., Mirme, S., Bernotas, T., Laakso, L., Hirsikko, A., Kulmala, M. (2007). A widerange multi-channel Air Ion Spectrometer. *Boreal Environment Research*, 12, 247-264.

[12] Tammet, H., Mirme, A., Tamm, E. (2002). Electrical aerosol spectrometer of Tartu University. *Atmospheric Research*, 62 (3-4), 315-324.

[13] Biskos, G., Reavell, K., Collings, N. (2005). Description and theoretical analysis of a differential mobility spectrometer. *Aerosol Science and Technology*, 39, 527-541.

[14] Kolarž, P., Marinković, B.P., Filipović, D.M. (2005). Zeroing and testing units developed for Gerdien atmospheric ion detectors. *Review of Scientific Instruments*, 76 (4), 046107.

[15] Charry, J.M., Kavet, R. (1987). *Air Ions: Physical and Biological Aspects*. CRC Press.

[16] Sirota, V., Safronova, V.G., Amelina, A.G., Maltseva, V.N., Avkhacheva, N.V., Sofin, A.D., Yanin, V.A., Mubarakshina, E.K., Romanova, L.K., Novoselov, V.I. (2008). The effect of negative air ions on the respiratory organs and blood. *Biophysics*, 53 (5), 457–462.

[17] Sirota, T.V., Novoselov, V.I., Safronova, V.G., Yanin, V.A., Tsvetkov, V.D., Amelina, S.E., Lushnikova, A.L., Maltseva, V.N., Tikhonov, V.P., Kondrashova, M.N. (2006). The effect of inhaled air ions generated by technical ionizers and a bioionizer on rat trachea mucosa and the phagocytic activity of blood cells. *IEEE Transactions on Plasma Science*, 34 (4), 1351-1358.

[18] Tikhonov, V.P., Temnov, A.A., Kushnir, V.A., Sirota, T.V., Litvinova, E.G., Zakharchenko, M.V., Kondrashova, M.N. (2004). Complex therapeutical effect of ionized air: Stimulation of the immune system and decrease in excessive serotonin. H2O2 as a link between the two counterparts. *IEEE Transactions on Plasma Science*, 32 (4), 1661-1667.

[19] Kondrashova, M.N., Grigigorreko, E.V., Tikhonov, A.N., Sirota, T.V., Temnov, A.V., Stavrovskaya, I.G., Kosyakova, N.I., Lange, N.V., Tikonov, V.P. (2000). The primary physico-chemical mechanism for the beneficial biological/medical effects of negative air ions. *IEEE Transactions on Plasma Science*, 28 (1), 230-237.

[20] Tikhonov, V.P., Tsvetkov, V.D., Litvinova, E.G., Sirota, T.V., Kondrashova, M.N. (2004). Generation of negative air ions by plants upon pulsed stimulation applied to soil. *Journal of Plant Physiology*, 51 (3), 414-419.

[21] Szabó, Z., Bartušek, K. (2009). Air ions concentration influence on bacterial colony count in the dwelling spaces. In *PIERS Proceedings, Moscow, Russia, August 18-21, 2009*, 1053-1055.

[22] Kolarž, P.M., Filipović, D.M., Marinković, B.P. (2009). Daily variations of indoor air-ion and radon concentrations. *Applied Radiation and Isotopes*, 67 (11), 2062-2067.

[23] Kolarž, P., Gaisberger, M., Madl, P., Hofmann, W., Ritter, M., Hartl, A. (2011). Characterization of ions at Alpine waterfalls. *Atmospheric Chemistry & Physics Discussions*, 11 (9), 3687-3697.

[24] Freund, F.T., Kulahci, I.G., Cyr, G., Ling, J., Winnick, M., Tregloan-Reed, J., Freund, M.M. (2009). Air ionization at rock surfaces and pre-earthquake signals. *Journal of Atmospheric and Solar-Terrestrial Physics*, 71 (17-18), 1824-1834.

[25] Freund, F. (2011) Pre-earthquake signals: Underlying physical processes. *Journal of Asian Earth Sciences*, 41 (4-5), 383-400.

[26] Aplin, K.L. (2008). Composition and measurement of charged atmospheric clusters. In *Planetary Atmospheric Electricity*. Springer, Vol. 30, 213-224.

[27] Leblanc, F., Aplin, K.L., Yair, Y., Harrison, G., Lebreton, J.P., Blanc, M. (Eds.) (2008). *Planetary Atmospheric Electricity*. Springer.
[28] Israël, H. (1971). *Atmospheric Electricity*. Vol. I. Jerusalem: IPST.
[29] Jirka, Z. (2001). *Speleoterapie: principy a zkušenosti*. 1. vyd. Olomouc: Univerzita Palackého. (in Czech)
[30] Bartušek, K., Fiala, P., Jirků, T., Kroutilová, E. (2007). Experiments of accuracy air ion field measurement. *PIERS Online*, 3 (8), 1330-1333.
[31] Steinbauer, M., Fiala, P., Bartušek, K., Szabó, Z. (2008). Experiments with accuracy of air ion field measurement. In *PIERS Proceedings, Hangzhou, China, March 24-28, 2008*, 1062-1066.
[32] Roubal, Z., Křepelka, P. (2013). Estimation of the air ion mobility spectrum by means of a Gerdien Tube with a segmented inner electrod. In *PIERS Proceedings, Stockholm, Sweden, August 12-15, 2013*, 767-771.
[33] Roubal, Z., Szabó, Z., Steinbauer, M. (2014). Uncertainty determination in measurements using a Gerdien Tube. In *PIERS Proceedings, Guangzhou, China, August 25-28, 2014*, 1902-1906.
[34] Israël, H., Schulz, L. (1933). The mobility-spectrum of atmospheric ions—principles of measurements and results. *Journal of Geophysical Research*, 38 (4), 285-300.
[35] Roubal, Z., Steinbauer, M. (2010). Design of electrometric amplifier for aspiration condenser measurement. In *PIERS Proceedings, Xi'an, China, March 22-26, 2010*, 1430-1434.
[36] Bartušek, K., Dokoupil, Z. (2003). Automatic device for ion fields measurement. *Measurement Science Review*, 3 (3), 75-78.
[37] Roubal, Z., Steinbauer, M., Szabó, Z. (2010). Modeling of saturation characteristic of an aspiration condenser. *PIERS Online*, 6 (1), 26-30.
[38] Roubal, Z., Bartušek, K., Szabó, Z., Drexler, P. (2011). Measurement of concentration and mobility spectrum of air ions in the natural environment. In *PIERS Proceedings, Marrakesh, Morocco, March 20-23, 2011*, 648-652.
[39] Bartušek, K., Buřival, Z., Darina, H. (1999). Methodology of measurement of air ions in moist environment for speleotheraphy. In *Measurement '99: 2nd International Conference on Measurement*. Bratislava, Slovak Republic: Institute of Measurement Science, Slovak Academy of Sciences, 262-265.
[40] Kolarž, P.M., Filipović, D.M. (2003). A new design of Gerdian type of small air-ion detector. In 5*th General International Conference of Balkan Physical Union (BPU-5)*, August 25-29, 2003, Vrnajcka Banja, Serbia and Montenegro, 411.

Received November 11, 2016.
Accepted January 25, 2017.

MEASUREMENT SCIENCE REVIEW, **17**, (2017), No. 1, 37-47

DE GRUYTER OPEN

MEASUREMENT SCIENCE REVIEW

Journal homepage: http://www.degruyter.com/view/j/msr

ISSN 1335-8871

An Experiment to Prove the Effect of Low-Level Magnetic Fields Resulting from Ionospheric Changes on Humans

M. Hanzelka[1], J. Dan[2], M. Šlepecky[4], V. Holcner[3], P. Dohnal[1], R. Kadlec[1]

[1]*Department of Theoretical and Experimental Electrical Engineering, Brno University of Technology, Technická 3082/12, 616 00 Brno, Czech Republic*
xhanze09@feec.vutbr.cz, tel.: +420 54114 6280, fax: +420 5 4114 6276
[2]*Rector's Office, Personnel Management Office, Masaryk University, Žerotínovonám. 9, 601 77 Brno, Czech Republic*
dan@rect.muni.cz, tel.: +420 54949 3455
[3]*Faculty of Economics and Management, University of Defence, Kounicova 65, 662 10 Brno, Czech Republic*
vladan.holcner@unob.cz, tel. +420 973 444 956
[4]*Constantine the Philosopher University in Nitra, Trieda A. Hlinku 1949 74 Nitra, Slovak Republic*
milos.slepecky@gmail.com, tel. +421 903 500 887

The investigation presented in the paper was performed in the laboratories of the Department of Theoretical and Experimental Electrical Engineering, Faculty of Electrical Engineering and Communication, Brno University of Technology, between April22 and June 26, 2014. We examined a homogeneous sample of male and female participants comprising a total of 49 persons aged 19 to 26. The time required for the measurement of psychophysiological parameters corresponded to 19 minutes, encompassing five stages: Basic (5 mins.), Color (2 mins.), Rest (5 mins.), Math (2 mins.), and Rest (5 mins.). All the measuring cycles were carried out using a BioGraph Infiniti device (Thought Technology, Ltd.). Generally, the impact of the environment upon living organisms constitutes a crucial problem examined by today's science. In this context, the present article describes the results of an investigation focused on ionosphere parameter variation and its role in the basic function of the nervous system. The discussed research concentrates on the measurement and detection of changes in the region of very low electromagnetic field frequencies; the authors introduce and verify related theoretical and experimental procedures to define the effects that influence brain activity and the cardiovascular system.

Keywords: Ultra low Frequency, Super Low Frequency, Extremely Low frequency, BioGraph Infiniti, Schumann resonances, heart coherence.

1. INTRODUCTION

The low-level measurement of low frequencies (0.01-10 Hz) performed to evaluate the effect of magnetic fields on the human organism can be regarded as an interdisciplinary branch of science that embraces different types of research. In this context, it is important to consider applied research disciplines, such as the measurement and radar technology in the following ranges: the ULF (Ultra Low Frequency Band: 300 Hz – 3 KHz), SLF (Super Low Frequency Band: 30 Hz – 300 Hz), and ELF (Extremely Low Frequency Band: 0.1 Hz – 30 Hz) [3]. The current status of knowledge in the given field is relatively unsatisfactory, and certain hasty conclusions have been made and subsequently applied even in hygienic standards. An example of such standards is the guideline issued by the Council of Europe and implemented by ICNIRP [4] in 1999 to establish the boundary values of magnetic flux in relation to the speed of magnetic field variations for very slowly changing currents. More concretely, this guideline introduces the value of 50 mT/s as the maximum magnetic flux change acceptable in an environment having a variable magnetic field at the frequency of 1 Hz and characterized by permanent presence of humans. This value is many million times higher than the largest changes hitherto measured during processes referred to as magnetic storms, in which the Earth was exposed to charged particles from the Sun.

The paper proposes an experiment involving comprehensive coverage of measurable parameters of the human body in a homogeneous sample of participants; the participants are monitored repeatedly, and the relevant parameters are evaluated with respect to external magnetic field changes. The generation and effects on the human organism of low-level magnetic fields induced by solar activity were described previously, [3] and [4].

According to the conclusions of the secondary research, there is mutual interaction between low-level electric or

DOI: 10.1515/msr-2017-0005

magnetic fields irradiated by both humans and the geomagnetic system. We present a portion of the research conducted in this province at the Department of Theoretical and Experimental Electrical Engineering (DTEEE), Faculty of Electrical Engineering and Communication (FEEC), Brno University of Techology (BUT); the investigation exploits the current knowledge of low-level magnetic fields generated by the geomagnetic mechanism and the solar system. The attention is centered on examining the effect of solar activity-induced changes in Earth's magnetic system. In this context, the research also focuses on proving the existence of that effect as a result of geomagnetic storms, which substantially influence low-level magnetic fields affecting the human organism, including its behavioral patterns and decision-making [5]. The detection of changes and disturbances in the geomagnetic field could be performed by means of the Schumann resonances. Until recently, the relevant oscillation was at the average yearly frequency of fsch=7.83 Hz; this frequency changes in consequence of the impact exerted by phenomena such as the solar wind or greenhouse gases. In 1953, Professor W.O.Schumann of the Technical University of Munich, Germany [6] found out that the cavity between the ionosphere and Earth's surface could be interpreted as a spherical resonator.

2. SUBJECT & METHODS

The laboratory-based research comprising a homogeneous sample of 49 subjects (men and women aged 19 to 25) began on April 22, 2014 and lasted until June 26, 2014 [7]. The young age and homogeneity characteristic of the group of participants led to stable cognitive competencies such as working memory, selective attention, multitasking, task switching, response monitoring, and error detection. Nearly all of these functions show an age-related decline [8]. The total time required for the examination of the psychophysiological parameters of a subject corresponded to 19 minutes. We used a Nickelodeons Infiniti [9] (Thought Technology, Ltd.) unit to perform the entire task, and the measurement proper involved five phases: Rest; Color; Rest; Math; and Rest. At the Color stage, a special (Stroop) test was utilized to acquire the psychophysiological responses of each subject to a load on their organism. Generally, this tool demonstrates that a person performing the given task can be easily distracted due to their automatic reactions and habits; the procedure is named after John Ridley Stroop (1897 - 1973), the American psychologist who first described the phenomenon in 1929 [10]. In the Math phase, then, the participants were asked to progressively subtract the number 7 from the initial value of 1081, and we examined the psychophysiological stress generated during such quiet countdown. The total number of measurements was 210, with the average of 4.29 per participant. The relationship between the above total count and the number of subjects who completed the task is shown in Table 1. The laboratory was configured to facilitate the measurement of comparable parameter values, namely constant temperature, noise, humidity, lighting, concentration of positive and negative ions, and homogenized geomagnetic field component (Fig.3.c)).

3. RESULTS

A major part of the laboratory research consisted of large-scale collection of psychological data from all participants (respondents) via several psychological tests, including an ASS-SYM test; this tool measures a respondent's sensitivity to changes in the transition from load to relax. All the results were then correlated with the psychophysiological measurements.

Table 1. The relationship between the number of completed measurements and the number of respondents.

Number of respondents	Number of measurements
4	1
1	2
4	3
12	4
24	5
4	6
49	SUM

The measurement comprised three relaxation and two stress phases, with an emphasis on intensive psychological stress in the participants. The stress stages were induced using a low-level electromagnetic field generator, an amplifier, and Helmholtz coils to interact with the EEG brain waves of the participant involved. The resulting low-level field enabled us to simulate the effect of solar activity changes as an additional offset to the related real intensity indicators prepared for each day by NASA. The field strength in the Helmholtz coil was set to the level of the terrestrial magnetic field, and the major parameters were as follows: pulse f = 1 kHz; start = 100 ns; wavelength λ = 50.4 km and $\lambda/2$ = 25.2 km; T = 168 μs; amplitude 1 V on the generator- amplified, out of coil; Bmax=60 μT, according to Fig.1. The indicated spectrum is a swept one, between 0.01 Hz and 30 Hz.

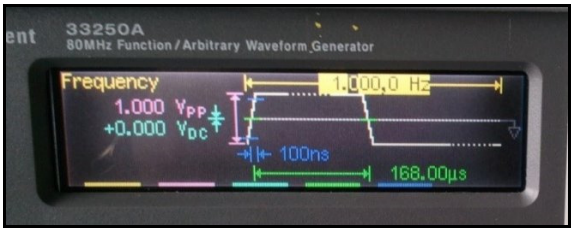

Fig.1. The waveform to offset field strength in the Helmholtz coil.

Fig.1. and Fig.2. illustrate the stimulation and measurement apparatus, and Fig.3. presents shots of the BioGraph Infiniti measurements.

In the course of the experimental research, a large volume of psychophysiological data were measured with the BioGraph Infiniti software; the actual measurement fundamentally exploited the states of relaxation and mental load placed upon each participant, whose mental condition was subsequently evaluated by means of psychological tests.

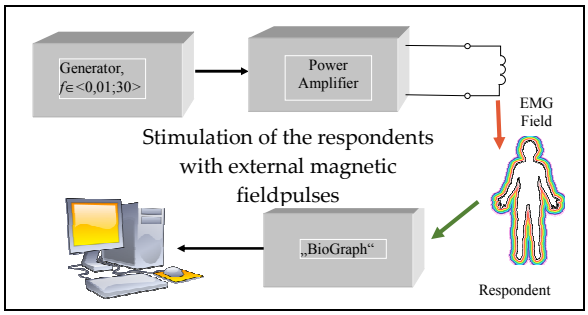

Fig.2. A scheme of the measurement and simulation apparatus.

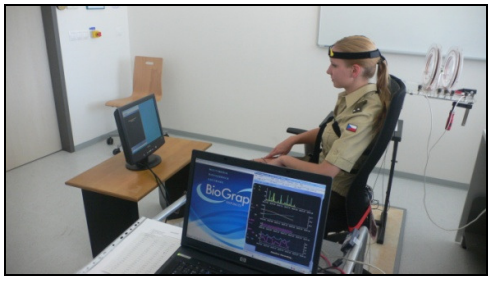

a)

b)

c)

Fig.3. The documentation shots from the laboratory measurements, a), b); the room with a geomagnetically stable magnetic field component, c).

The determined states can be expressed qualitatively. Based on the obtained information, we created a large, unique set of correlational dependencies existing between psychophysiological parameters of the human organism (or the related qualitative psychological measurement) and the intensity of solar activity.

Solar wind particles captured by Earth's magnetic field travel, especially in polar areas, along magnetic lines up to the upper layers of the atmosphere, where they – together with ultraviolet radiation from the Sun – excite and ionize neutral atoms. The excited atoms then emit a typical glow to form the well-known aurorae, and these ionized atoms are seized by the magnetic lines and move freely along them. Through this description, we have merely summarized general facts commonly exploited and referred to by various researchers. Methods and procedures for the measurement of ionosphere changes are currently available [11], Fig.3. In this context, secondary investigation of earlier observations may enable us to point out the connection between magnetic field changes and the social behavior of a group of humans. The corpus of specialized research on the problem comprises a large number of fundamental papers and monographs; interestingly, the achievements of the author of [12], Rollin McCraty, could also be of importance in many respects. McCraty gradually analyzed the impact of the environment on the physical, mental, emotional, and spiritual coherence of an individual, and he also outlined the relationship between these aspects and the cardiovascular system with its resonant frequency of 0.1 Hz (the ELF band of between 0.04 and 0.26 Hz, a precondition of cardiac coherence). Tchijevsky, then, found out that 80 % of the most significant events in human history occurred within an approximately five-year segment of solar activity, as illustrated in Fig.4., [12].

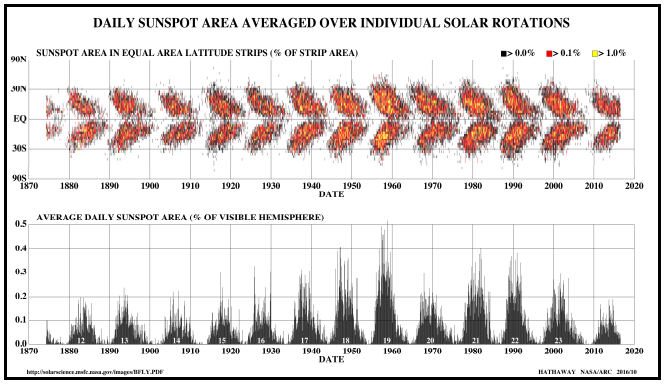

Fig.4. The values of solar activity since 1874, [12].

With respect to these aspects, however, no investigation has been performed thus far with a homogeneous group of selected human subjects to prove the long-term impact of changes in Earth's magnetic field and to eliminate any possible major influence of other factors.

During our experimental research, solar activity was monitored via NASA-indicated data: values acquired from daily solar activity measurements are collected by the agency for scientific purposes. Relevant graphs within this analysis present the solar activity record characterizing the activity period observed at the DTEEE, FEEC, Brno University of Technology.

The parameter of the Sun reflects the actual influence of solar wind particles, which – according to the velocity of the wind – bombard Earth's atmosphere, with a delay of between 2 and 8 days. A related study proposes that solar winds could be interpreted as collision less plasma moving

radially from the Sun at speeds oscillating between 300 and 800 km/s. The concentration of the wind varies from 1 to 10 cm-3, and its temperature ranges between 1 – 30 eV. The mass spectrum comprises mainly protons (~96 %) and helium nuclei (~4 %); the proportion of heavier elements is, for our purposes, negligible. In order to facilitate the measurement of solar wind parameters (or, more concretely, the proton component), a suitable detector was designed to operate from the orbit.

Hypotheses:
H0. The low-level magnetic fields generated by solar activity exert a negative impact on the human organism and influence human behavior and decision-making.
H1. The mutual interaction between the low-level magnetic and electromagnetic fields of a human subject and the low-level magnetic fields induced by geomagnetic changes constitutes a significant phenomenon.
H2. Solar activity, the resulting manifestations of geomagnetic storms, and their comprehensive effect on the human organism as regards economic behavior and decision-making are directly interrelated factors.

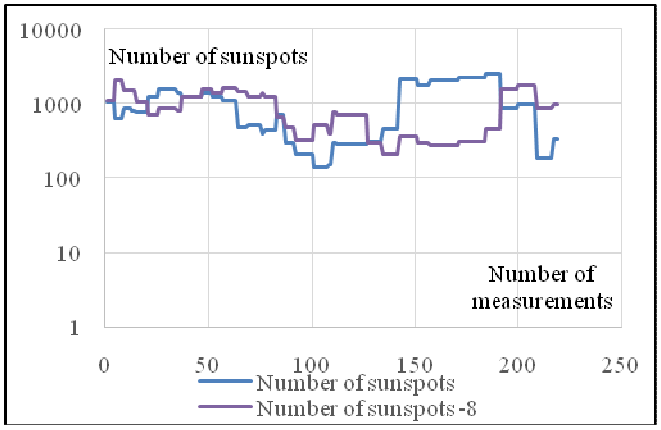

Fig.5. The progression of solar activity during the experimental research specified in chapter 3 (investigation performed between April 22 and June 26, 2014). Source: [13].

Data Analysis:
Static input psychological prerequisites

Before the actual commencement of the research, the 49 participants were assessed with the ASS-SYM and MBTI psychological testing methods. At the initial stage, before analyzing the methodology, we consider it important to introduce a brief definition of health as an underlying concept within our investigation. According to World Health Organization, health is "a state of complete physical, mental and social well-being and not merely the absence of disease or infirmity" [14]. This definition then leads us to a rather narrow domain of psychological methodology, namely self-assessment scales. With respect to these instruments, it is possible to accentuate the ASS-SYM, a representative method designed by the German psychologist Gunther Krampen [15]. The ASS-SYM, or Änderungssensitive Symptom Liste, constitutes an index of change-sensitive symptoms related to relaxed perception and experiencing, life satisfaction, mental load, problems, and other aspects outlined in [15]. The list comprises 48 items, within which each participant expresses themselves in four degrees. As proposed, the symptoms are sensitive to changes during autogenic training and progressive relaxation. The ASS-SYM has been verified as a part of the overall evaluation of the quality and effect of various therapeutic procedures; its advantage consists in that, unlike some other techniques, the discussed instrument does not cause excessive stress to the examined subject or bring any additional difficulties. The subscales relate to 6 areas (each comprising 8 items), and these domains involve several specific activities or elements: the examination and influencing of "intrinsic" mental processes such as the interpretation and assessment of the self and the environment; the core beliefs and assumptions of who I am and what the world around me is like; and determining the interrelationships or mutual impact between emotional experiences and cognitive mechanisms (or, in plain words, finding out how the brain and the heart influence each other). By definition, the areas concerned are presented as follows:

- Physical and mental exhaustion (such as "sleep disorder and falling asleep difficulty");
- Nervousness and mental tension ("internal stress, nervousness");
- Psychophysiological dysregulation ("inappetence");
- Behavioral and performance-related disorder ("performance anxiety prior to tests, exams, and similar situations ");
- Self-control difficulties ("head aches or pressures");
- General symptoms and problems ("indecisiveness, decision-making difficulty").

The initial psychological examination as a component of the wider test of the impact of geomagnetic field changes on a human being was attended by 38 from the total of 49 participants, and the obtained results are indicated in Fig.6. below.

In the course of the measurement, the majority of participants (mostly of military background) exhibited physical and mental exhaustion, behavioral and performance-related disorder, and burden of pain. Nine participants were affected by simultaneous action of all the three effects; interestingly, in six participants out of these nine we detected concurrent affection by 5 from the above-outlined 6 effects. This set of participants will be hereafter referred to as emotionally labile, EL. Even though a majority of the symptoms clearly manifested themselves at this stage, none of the subjects exhibited psychophysiological dysregulation.

The follow-up phase of the research consisted of MBTI-based personality testing. In spite of substantial character differences, the participants can be classified into 16 basic categories, each comprising a set of subjects with certain identical traits; thus, we respect the system of personality types founded by Carl Jung, further developed by American researchers Katharine Cook Briggs and Isabel Briggs Myers, and refined to its current forms (as regards, for example, the nomenclature) by later 20th century scholars [17].

The relevant classes are determined via the Myers–Briggs Type Indicator (MBTI); when using this instrument, we adopted – in accordance with the above references - personality type denomination variants that best suited our purposes, and the applied typology then was as follows:
The type indicator (MBTI) was applied in only 44 out of the total of 49 respondents; a portion of these subjects did not participate in the initial psychological testing and attended merely the laboratory measurements. The MBTI test was performed prior to the measurement cycle via psychological testing of each participant.

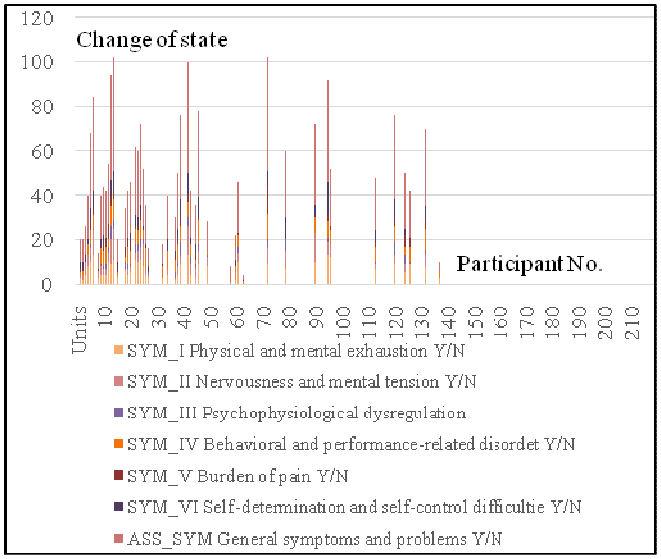

Fig.6. The assessment performed via the ASS-SYM instrument. Source: [16].

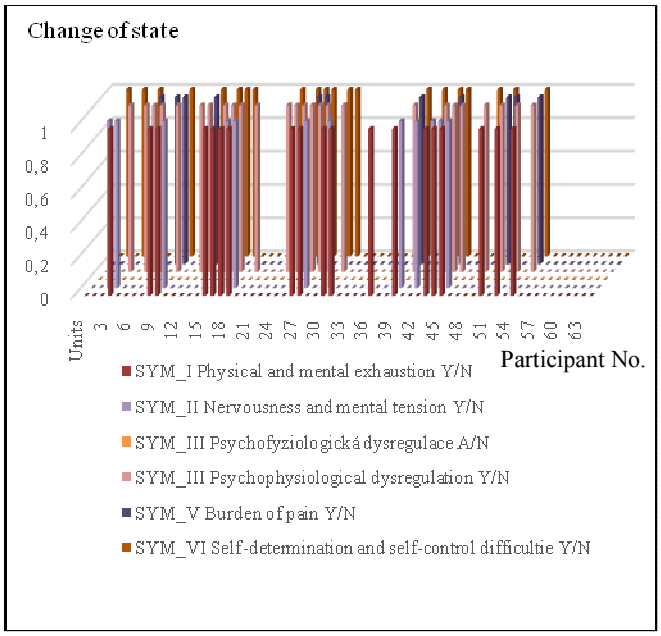

Fig.7. The cyclic change of the mental state in the three respondents specially observed during the experimental research. [16].

In the given context and as already outlined, from the general and theoretical perspectives, we investigate the influence of geomagnetic fields in relation to "intrinsic" human mental processes, such as the interpretation and evaluation of the self and the environment, core beliefs and assumptions of who I am and what the world around me is like, and we also focus on defining the mutual interaction between emotional experiences and cognitive processes, between the brain and the heart [18].

Dynamic gradual psychological prerequisites

Each psychophysiological measurement cycle was preceded by a Lüscher color test session. The Lüscher test concept comprises 8 color cards (blue, green, red, yellow, violet, brown, grey, and black) combinable into 40,320 possible answers. The main advantage of the instrument consists in its hidden validity: as the participant does not know the purpose of this particular test and cannot estimate what is being defined by it, they are not able to suitably modify their answers in advance to fit the presumed or desired result. Applicable criticism targeting the alleged insufficient reliability of the method is analyzed by, for example, the main author of papers [19], [20], and [21], who proposes that the test captures the dynamics of mental states and that "the determination of reliability in the sense of consistency is not feasible" owing to the structure of the instrument. The repeated use of the Lüscher color test enabled us to reveal progressively the actual mental state of the respondents prior to the main psychophysiological measurement, especially as regards the following parameters:

S – deteriorated mental condition; A – anxiety; B – emotional discomfort; A, B – mental imbalance.

The pattern in Fig.7. shows deteriorated mental condition in three subjects of the EL group; this decrease occurred cyclically during the entire experimental research and in all the monitored variables.

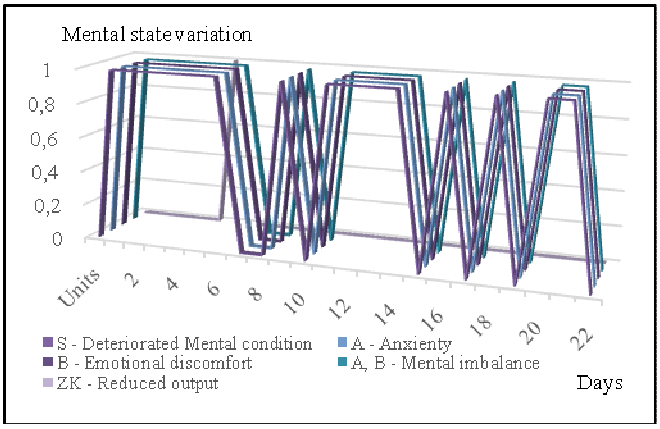

Fig.8. The sample of participants exhibiting reduced performance. Source: [16].

Another quantity monitored within the dynamic psychological data was mirror drawing, intended to define the instantaneous performance rate of the subjects. This activity was used to conclude each physiological measurement session. Fig.8. then represents the set of participants who exhibited signs of reduced performance; this group comprises32 out of the 49 respondents participating in the psychophysiological measurement.

Relationship between individual changes in the intensity of solar processes, and the effect of such changes on the skin conductance of examined participants

According to a major reference [22], skin conductance changes are caused by activation of the autonomic nervous system rather than by emotions. Based on the actual needs, however, strong emotions prepare the human organism for an intensive activity; variation in emotions is then accompanied by accelerated breathing, cardiac function, and vascular circulation. This process results in altered skin conductance, from the lowest level in sleep to the highest one attained under conditions such as emotional stress. The present study follows from the assumption that emotional lability in responsive individuals is directly related to and incited by changes of solar activity; conversely, in the same context, participants classified within the preliminary testing cycle as emotionally stable will be generally less sensitive to the discussed variations. The performed measurements propose that, in emotionally responsive individuals, skin conductance depends on changes in the intensity of solar activity (namely, the increase or decrease of such activity) rather than on its amplitude. As illustrated in Fig.9., the variation of solar activity then constitutes an element abetting emotional lability in humans, and this condition manifests itself in the growth of skin conductance. During the laboratory-based measurement of the psycho-physiological parameters of the human organism in relation to the intensity of solar activity, we simulated the effects of such activity via using a pulse magnetic field (as already mentioned above) that exhibited the magnetic flux density of B_{max}=60 μT in the region outside the Helmholtz coil; this field spread out towards the head of a participant, into a homogenized environment (this environment was completed with a special shielding bolster located in the vicinity of a participant, embodying the modification of Earth's inhomogeneity - namely, a quasi-stationary field - and the influence of natural radioactivity). At the head of a participant, which was positioned outside the absolutely homogeneous field, we set/measured B_{max}= 5.0 μT. The exposure to the given field was invariably triggered in the Color and Math load phases, in two-minute intervals. For the purposes of pulse measurement, identical repeatable conditions were set for all participants. The exposure was eliminated from the Rest stages. The total experiment time allocated to each respondent, including the preparation and connection to the measuring apparatus, equaled 40 minutes; within this period, a participant was exposed to the applied pulse magnetic field for four minutes.

Within the research, we also considered the actual effect of solar activity, assuming the delay of -4 to -8 days according to the relevant solar wind intensity (Fig.5.). The laboratory-based simulation of the conditions enabling the effect of solar activity brought into the measurement an additional gradient of low-level magnetic field changes in different phases of the psychophysiological measurements. Such changes are exemplified, with respect to skin conductance, in Fig.9., which also indicates the action of an offset pulse (twice every two minutes) during the entire forty-minute measurement. To amplify the effect of an external magnetic field resulting from solar activity, we performed the measurement in the lowest lying laboratory of the DTEEE.

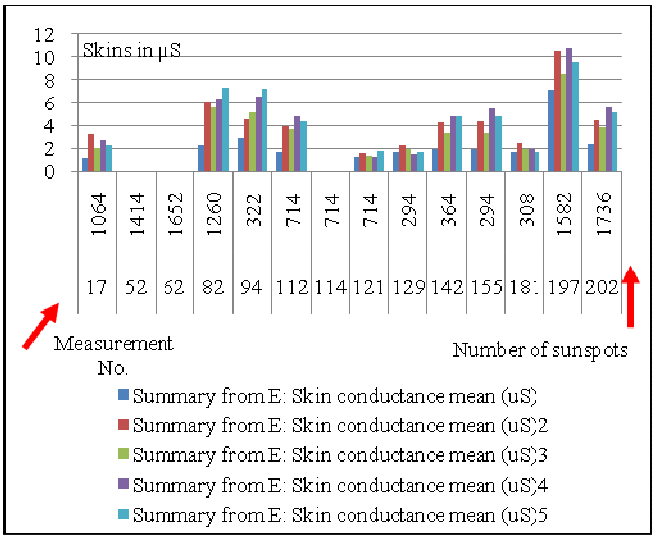

Fig.9. The variation of solar activity constitutes an element abetting emotional lability in humans; this condition manifests itself in the growth of skin conductance [16].

Changes in the intensity of solar activity and their effect on cardiac variability in the sample of participants

The theoretical basis for the domain of cardiac variability exploits the frequency analysis specified in Table 2.

A relevant reference [23] proposes that heart rate variability (HRV) is considered the neurocardiac function factor which reflects the interaction between the heart, brain, and autonomic nervous system (ANS) dynamics. All HRV parameters are derived from the evaluation of natural heartbeat changes, and HRV as such is substantially more than a mere indicator for cardiac frequency assessment: it reflects the complex interactions between the heart and a high number of bodily systems [24]. The optimum level of variability in key regulation systems of an organism has fundamental meaning for its internal flexibility and adaptability or, by extension, the resistivity and immunity, which embody a healthy coherent function and overall well-being. While an excessive amount of instabilities exerts a negative impact on effective physiological functioning and energy usage, a variation too low denotes an energy decrement or cardiac pathologies [25].

Table 2. The description and definition of the calculated parameters of the spectral analysis of cardiac frequency variability [25].

Description	Frequency band: VLF [0,02–0,05] Hz	LF [0,05–0,15] Hz	HF [0,15–F] Hz	Physical unit
Spectral power	$Power\ VLF = \int_{0,02}^{0,05} PSD\ df$	$Power\ LF = \int_{0,05}^{0,15} PSD\ df$	$Power\ HF = \int_{0,15}^{F} PSD\ df$	ms^2
Relative spectral power	$Rel.\ VLF = \frac{Power\ VLF}{Total\ Power}$	$Rel.\ LF = \frac{Power\ LF}{Total\ Power}$	$Rel.\ HF = \frac{Power\ HF}{Total\ Power}$	%
Individual spectral power ratios	$VLF/HF = \frac{Power\ VLF}{Power\ HF}$	$LF/HF = \frac{Power\ LF}{Power\ HF}$	$VLF/LF = \frac{Power VLF}{Power\ LF}$	—
Compensation coefficient for the effect of RR interval magnitudes	$CCVVLF = \frac{\sqrt{Power\ VLF}}{RR} * 100$	$CCVLF = \frac{\sqrt{Power\ LF}}{RR} * 100$	$CCVHF = \frac{\sqrt{Power\ HF}}{RR} * 100$	%
Total spectral power	$Total\ Power = \int_{0,02}^{F} PSD\ df$ nebo $(Power\ VLF + Power\ LF + Power\ HF)$			ms^2
Mean value of RR intervals	$RR = \frac{1}{n}\sum_{1}^{n} RR_i$			ms
Mean value of the power of sequential differences of the RR intervals	$MSSD = \frac{1}{n-1}\sum_{1}^{n}\left(RR_i - RR_{i-1}\right)^2$			ms^2

The quantity or extent of total HRV relate to the present-day lifestyles and are higher in younger people than in older ones [26]. A low HRV constitutes a strong and independent predictor of future health problems, including all mortality causes [27], and it is connected with a number of health conditions [28], [29]. Generally, HRV is also a significant indicator of not only psychological and behavioral resilience but also the ability to adapt oneself effectively to varying social or environmental conditions [30], [31], and HRV quiescent levels are associated with individual cognitive performance differences in tasks that require the use of physical performance functions [31]. Heart rate variability is reflected in the total cardiac power spectrum as a large output increase within low frequency (LF) bands (typically around 0.1 Hz) and a decrease at very low frequencies (VLF) or in high frequency (HF) bands [32], [33]. Thus, heart rate variability can be defined as relatively harmonic (sine-wave-like) signals with very narrow and high peak amplitude in the LF region of the HRV power spectrum but without main peaks in the VLF or HF regions. This holds true for the respiratory frequency of about 6 breaths per minute, where the complex ICA is reduced, and the characteristic introduced in the above definition is regarded as the load for the organism and possible training. Such variability then approximately consists in the amplitude ratio LF / (VLF + HF); more specifically, for the above-described problem, variability is observed between 0.04 and 0.26 Hz of the total power spectrum range. In general terms, the discussed phenomenon constitutes a highly effective functional mode that is closely connected with the expedient use of energy sources and with many health-related advantages. These include six central aspects, namely

1) resetting the sensitivity of the baroreceptors that relate to short-term blood pressure control and increased respiratory efficiency [34];
2) increased vagus nerve afferent stimulation, which participates in the inhibition of signals in sympathetic nerves [34];
3) improved cardiac output in conjunction with enhanced efficiency in fluid exchange, filtering, and absorption between the capillaries and tissue [34];
4) strengthened ability of the cardiovascular system to adapt to circulation requirements;
5) increased time synchronization of cells in the whole body (Langhorst et al. 1984); and
6) improved synchronization of the mutual activity of ANS branches [24].

The above elements all result from the overall coherence to energetically enhance the entire system [34]. Another facet of the variability mode is the resonance effect. In this context, applicable mathematical models can be used to demonstrate that the resonant frequency of the human cardiovascular system is determined according to the feedback between the heart and the brain [34]. In humans and a large variety of animals, the resonant frequency of the system corresponds to approximately 0.1 Hz. Based on the proposed details, we can conclude that variability and resonance are typical of the natural physiological effects associated with the heart; these effects constitute and induce positive emotions. The graphs below show a continuous, solar activity-related BVL HF and BLV LF heart variability record of the selected sample of emotionally labile respondents. According to the graphically presented data, a higher emotional load was accompanied by a domination of BVP LF. However, it is not completely clear whether the cause of the higher BVP LF consisted in a changed intensity of solar activity or in the actual emotional character of each respondent within the EL group.

Functions of the ANS are also markedly influenced by respiratory sinus arrhythmia, which is, from the frequency perspective, found in the predominantly weighted spectrum (HF) situated between 0.15-0.4 Hz; the respiratory frequency then correspondingly ranges between 9-24 breaths/min. In the described experimental research, we observed negative breathing, where thoracic respiration dominates. By correlating such negative breathing with solar activity changes, we reach the conclusion that, in the group of emotionally labile respondents, negative breathing manifested itself mainly as a result of a change of the intensity of solar activity without any major influence of the amplitude of such activity.

4. DISCUSSION / CONCLUSIONS

During the experimental research, large amounts of quantifiable psychophysiological data based on the states of relaxation and mental load were obtained using the BioGraph Infiniti software. In this context, we also employed psychological tests to determine the mental state of the respondents, and the results of this phase can be expressed qualitatively. These procedures enabled us to form a unique, extensive group of correlational dependencies existing between psychophysiological parameters of the human organism and the intensity of solar activity with corresponding changes of the external electromagnetic field.

Impact of changes in the intensity of solar activity on skin conductance (skins) in the examined respondents

According to the research presented in [26], skin conductance changes are induced by the activation of the autonomic nervous system rather than by emotions. Strong emotions, however, prepare the human organism for a major activity, depending on the actual need; in the course of an emotional change, the breathing, cardiac activity, and vascular circulation all accelerate. This process then results in changed skin conductance, from the lowest level during sleep to the highest values typical of situations such as emotional stress.

Significantly, this paper as a whole is based on the presumption that the lability of individuals more prone to being influenced by emotional stimuli will be abetted by variation in solar activity; conversely, in this context, those participants who exhibited relatively consistent emotional stability during the pre-research testing will show less dependence on the discussed changes. The measurement results propose that skin conductance in emotionally sensitive individuals depends on variation in solar activity (growth or drop) rather than on its amplitude. According to Fig.10., a solar intensity change increases the rate of emotional lability in the human organism, thus also causing the relevant skin conductance to grow.

Impact of changes in the intensity of solar activity upon heart variability in the respondents

The research showed that such correlational dependence manifested itself markedly in skin conductance (or its growth) and heart variability via changes in the LF/HF frequency ratio, shown in Fig.11.; domination of the parasympaticus was observed, and thoracic respiration, i.e., negative breathing, prevailed over abdominal respiration.

The evaluation presented herein relates to participants whose psychological test results (those obtained from the ASS-SYM, MBTI, Lüscher–Color–Diagnostik, and mirror drawing) exhibited increased mental lability.

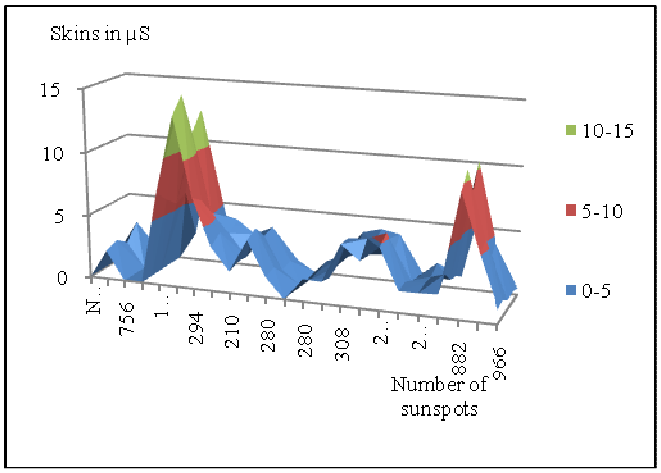

Fig.10. The relationship between skin resistance and solar activity changes in labile individuals. Source: [16].

The follow-up research will continue to evaluate the above-described dependencies in all participants, thus including also those who showed stable or variable mental condition, and the individual procedures will enable us to establish a benchmark for the psychophysiological parameters of healthy, mentally balanced subjects. Further, this benchmark is expected to facilitate mutual comparison between the groups of participants involved in the research.

The investigation of the intensity of solar activity, a phenomenon contingent on changes of solar wind intensity, was performed in the course of using data acquired and classified by NASA.

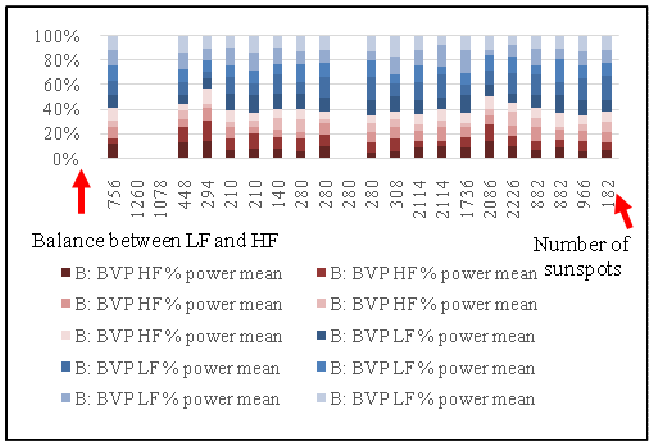

Fig.11. The dependence of the BVP HF and BVP LF signals on solar activity in emotionally labile participants. Source: [16].

At this point, we can note again that the primary aim of our effort lies in defining the impact of solar wind intensity changes on emotions, stress generation, and performance in a homogeneous sample of participants. Research of such scope has not been published thus far; one of its central benefits is the formation of a benchmark of psychophysiological values acquired from a homogeneous set of participants, the basic data range being as follows:

Age: 20 to 31

Body temperature before *)PP measurement: 35.5 to 37.5 OC

Body temperature after *)PP measurement: 35.5 to 37.0 OC

Systolic blood pressure before *)PP measurement: 100 to 180 mmHg

Diastolic blood pressure after *)PP measurement: 40 to 91 mmHg

Systolic blood pressure before *)PP measurement: 94 to 185 mmHg

Diastolic blood pressure after *)PP measurement: 48 to 99 mmHg

Number of sunspots during (Plasma waves hitting Earth) *)PP measurement: 140 to 2226 p/cm3 – number of sunspots*)PP: psychophysiological measurement with the BioGraph Infiniti device.

The output of the measurement cycles is summarized in Table 3.; while the relaxation phases Basic and Rest lasted 5 minutes, the Color and Math stages ran for two minutes only. Table 3. also shows the ranges of the measured

psychophysiological values in the individual, consecutive phases. Importantly, special emphasis was placed on examining the LF/HF ratio; at high solar wind intensities, domination of the parasympaticus was observed. The standard deviation of this LF/HF ratio, depending on solar wind intensity changes determined by the number of sunspots, is illustrated in Fig.12. below.

The above figure indicates that, at low solar wind rates, the dispersion of the LF/HF values is more uniform, with min. 0.084 and max. 5.71. At high solar wind intensity rates (from 1,000 units), the dispersion of the LF/HF values tends to grow and exhibits greater dynamics, namely, min. 0.056 and max. 10.94. Fig.12. simultaneously shows volatility differences in the standard deviations characteristic of the individual load phases (Basic; Color (two-minute color reading); Rest; Math (two-minute progressive subtraction of the number 7 from 1081); and Rest).

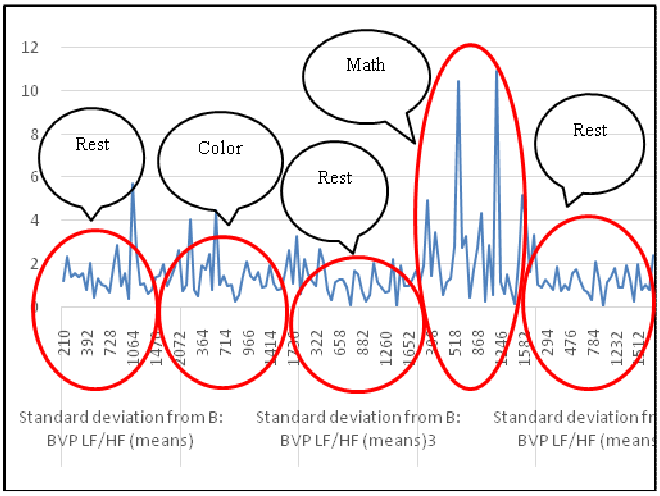

Fig.12. The BVP LF/HF standard deviation. Source: [16].

Table 3. The ranges of the measured psychophysiological values. Source: [16].

Sequence	Basic		Color		Rest		Math		Rest	
B: BVP amplitude mean (Rel)	0	30.0	0	20.6	0	22.0	0	21.9	0	21.2
B: BVP HR mean (beats/min)	0	125.84	0	123.12	0	97.72	0	125.28	0	99.68
B: BVP HR std. dev.	0	60.66	0	45.61	0	44.44	0	43.22	0	46.07
B: BVP peak freq. mean (Hz)	0	0.27	0	0.26	0	0.24	0	0.33	0	0.27
B: BVP IBI std. dev. (SDRR)	0	366.1	0	361.47	0	366.88	0	426.15	0	363.13
B: BVP VLF % power mean	0	44	0	65.36	0	46.41	0	67.27	0	51.25
B: BVP LF % power mean	0	86.39	0	84.76	0	71.82	0	87.18	0	68.4
B: BVP HF % power mean	0	80.94	0	61.57	0	79.89	0	74.99	0	77.54
B: BVP ULF % power mean	0	16	0	31.13	0	17.7	0	32.75	0	14.98
B: BVP VLF total power mean	0	2549.09	0	3525.78	0	12547.57	0	2874.66	0	7478.45
B: BVP LF Total power mean	0	5142.99	0	12113.5	0	8879.18	0	5915.88	0	12536.73
B: BVP HF total power mean	0	4464.12	0	11793.98	0	6587.36	0	7841.5	0	7094.28
B: BVP LF/HF (means)	0	14.85	0	14.79	0	9.02	0	30.94	0	7.13
Total spectral power	0	8629.04	0	21593.77	0	15467.89	0	13758.13	0	16747.21
C: EMG mean (uV)	0	592.58	0	623.16	0	600.11	0	622.14	0	615.93
D: EMG mean (uV)	0	219.63	0	325.07	0	380.12	0	613.48	0	502.14
E: Skin conductance mean (uS)	0	17.34	0	20.58	0	18.27	0	19.19	0	17.49
E: SC as % of value mean (%)	0	346.9	0	411.68	0	365.38	0	383.88	0	349.89
F: Temperature mean (Deg)	0	36.01	0	35.98	0	36.07	0	36.04	0	36.08
F: Temp as % of value mean (%)	0	36.74	0	36.72	0	36.81	0	36.77	0	36.82
G: Resp rate mean (br/min)	0	18.8	0	15.25	0	18.77	0	19.75	0	18.8
B&G: (HR max-min) mean (b/min)	0	51.72	0	116.92	0	84.94	0	102.94	0	92.24
G: Abd amplitude mean (rel)	-0.69	5.17	0	5.6	0	4.61	0	3.64	0	4.82
H: Thor amplitude mean (rel)	0	4.03	0	4.43	0	3.35	0	3.03	0	2.99
G&H: Abd-tho ampl diff (means)	-2.27	4.53	-3.29	4.62	-2.23	3.8	-2.26	3.3	-1.78	3.51

Within the planned follow-up activities, we will concentrate on further examination of the investigated variables, or the HRV, EMG [32] and [33], Skins [34], Abd and Thor respiration amplitudes, which were systematically monitored in the course of the research involving a homogeneous sample of participants.

APPENDIX

The article discusses the results and evaluation of a cycle of experimental measurements performed to define the impact of solar activity upon an individual and their social interactions. The related primary research has shown that geomagnetic field changes resulting from solar eruptions affect the neurophysiological condition and status of a human being within society. The obtained knowledge and conclusions are of major importance for predictive control applications related to the management of social and economic processes (such as those within healthcare, transportation, industrial and financial markets, and supply of energy and goods).

The experiment was performed with the intention to screen out the influence of Earth's external quasistationary field.

Using a source of an offset magnetic field to simulate in laboratory conditions the effect of changes in the intensity of solar activity amplified the variation of psychophysiological parameters, depending on solar activity. The problem of the possible effect of greenhouse gases and the related impact on the ionosphere was not analyzed within the described research, mainly because, from the perspective of the time domain, ionospheric changes due to climatic variation are very slow with respect to the manifested effects of solar activity.

ACKNOWLEDGMENT

The research was funded via the National Sustainability Program, grant No. LO1401. For the actual analyses and experiments, the current infrastructure of the SIX Center was used. The authors acknowledge the help and support of the University of Defence (Brno), whose students and employees formed a homogeneous sample of participants to facilitate the actual investigation procedures.

REFERENCES

[1] Ferris, J. (2010). The brain generates an electric field that influences its own activity. *Scientific American Mind*, 21 (10).

[2] Unakafov, A. (2009). Analysis and modeling of the galvanic skin response spontaneous component in the context of intelligent biofeedback systems development. *Measurement Science Review*, 9 (2), 36-41.

[3] Surkov, V., Hayakawa, M. (2014). *Ultra and Extremely Low Frequency Electromagnetic Fields.* Springer.

[4] International Commission on Non-Ionizing Radiation Protection (ICNIRP). (2009). *Exposure to High Frequency Electromagnetic Fields, Biological Effects and Health Consequences (100 kHz - 300 GHz): Review of the Scientific Evidence on Dosimetry, Biological Effects, Epidemiological Observations, and Health Consequences Concerning Exposure to High Frequency Electromagnetic Fields (100 kHz - 300 GHz).* ICNIRP, ISBN 978-3-934994-10-2.

[5] Prechter, R. (1999). *The Wave Principle of Human Social Behavior and the New Science of Socionomics*. New Classics Library.

[6] Miller, R.A., Miller, I. (2003). The Schumann's resonances and human psychobiology. *Nexus Magazine*, 10 (3).

[7] Urban, R., Holcner, V. (2010). Educating for the future challenges in military education at the beginning of the 21st century. In *Securitate şi apărare europeană în contextul crizei economico-financiare.* Bucharest, Romania: Editura Universităţii Naţionale de Apărare "Carol I", ISBN 978-973-663-809-1, 128-135.

[8] Falkenstein, M., Hoormann, J., Christ, S., Hohnsbein, J. (2000). ERP components on reaction errors and their functional significance: A tutorial. *Biological Psychology*, 51 (2-3), 87-107.

[9] Thought Technology Ltd. *Operations manual.*

[10] MacLeod, C.M. (1992). The Stroop task: The "gold standard" of attentional measures. *Journal of Experimental Psychology: General*, 121 (1), 12-14.

[11] Hanzelka, M., Dan, J., Fiala, P., Steinbauer, M., Holcner, V. (2015). Experiments with sensing and evaluation of ionosphere changes and their impact on the human organism. In *MEASUREMENT 2015: 10th International Conference on Measurement*. Bratislava, Slovak Republic: Institute of Measurement Science, Slovak Academy of Sciences, 173-176.

[12] McCraty, R. (2010). Coherence: Bridging personal, social and global health. *Alternative Therapies in Health and Medicine*, 16 (4), 10-24.

[13] NASA. (2015). *The solar wind*. http://solarscience.msfc.nasa.gov/SolarWind.shtml

[14] Krampen, G. (2006). *Änderungssensitive Symptomliste zu Entspannungserleben, Wohlbefinden, Beschwerden und Problembelastungen (ASS-SYM)*. Göttingen: Hogrefe.

[15] Dan, J. (2009). Lüscher – Color – Diagnostik. Tschechische Version. In *Lüscher – Color – Diagnostik*. Brunnen/Schweiz, 1.- 4.10.2009. 2009.

[16] Šťastný, P. (2015). *Solar Activity : Analytical Software in xls*. Brno.

[17] Berens, L., Nardi, D. (1999). *The Sixteen Personality Types: Descriptions for Self-Discovery.* Radiance House.

[18] Dan, J., Edelmann, A. (2013). *Max Lüschers Color Test*.

[19] Woodworth, R.S., Schlosberg, H. (1959). *Experimentálna psychológia (Experimental Psychology)*. Bratislava, Slovak Republic: VEDA, the Publishing House of the Slovak Academy of Sciences, 149-176. (in Slovak)

[20] McCraty, R., Atkinson, M., Tiller, W.A., Rein, G., Watkins, A.D. (1995). The effects of emotions on short-term power spectrum analysis of heart rate variability. *American Journal of Cardiology*, 76 (14), 1089-1093.

[21] Umetani, K., Singer, D.H., McCraty, R., Atkinson, M. (1998). Twenty-four hour time domain heart rate variability and heart rate: Relations to age and gender over nine decades. *Journal of the American College of Cardiology*, 31 (3), 593-601.

[22] Levy, B.R., Slade, M.D., Kunkel, S.R., Kasl, S.V. (2002). Longevity increased by positive self-perceptions of aging. *Journal of Personality and Social Psychology*, 83 (2), 261-270.

[23] Lindmark, S., Lonn, L., Wiklund, U., Tufvesson, M., Olsson, T., Eriksson, J.W. (2005). Dysregulation of the autonomic nervous system can be a link between visceral adiposity and insulin resistance. *Obesity Research*, 13 (4), 717-728.

[24] Saul, J.P., Arai, Y., Berger, R.D., Lilly, L.S., Colucci, W.S., Cohen, R.J. (1988). Assessment of autonomic regulation in chronic congestive heart failure by heart rate spectral analysis. *American Journal of Cardiology*, 61 (15), 1292-1299.

[25] Beauchaine, T. (2001). Vagal tone, development, and Gray's motivational theory: Toward an integrated model of autonomic nervous system functioning in psychopathology. *Development and Psychopathology*, 13 (2), 183-214.

[26] Thayer, J.F., Hansen, A.L., Saus-Rose, E., Johnsen, B.H. (2009). Heart rate variability, prefrontal neural function, and cognitive performance: The neurovisceral integration perspective on self-regulation, adaptation, and health. *Annals of Behavioral Medicine*, 37 (2), 141-153.

[27] McCrea, I.W., Jones, T.B., Schlegel, K., Tuomo, N. (1991). COSCAT, a new auroral radar facility on 930 MHz - system description and first results. *Annales Geophysicae*, 9, 461-469.

[28] Lehrer, P., Vaschillo, E., Lu, S.E., Eckberg, D. Vaschillo, B., Scardella, A., Habib, R. (2006). Heart rate variability biofeedback: Effects of age on heart rate variability, baroreflex gain, and asthma. *Chest*, 129 (2), 278-284.

[29] Foreman, R. (1997). Organisation of visceral input. In *Anesthesia: Biologic Foundations*. Lippincott-Raven Publishers, 663-683.

[30] Siegel, G., Ebeling, B.J., Hofer, H.W., Nolte, J., Roedel, H., Klubendorf, D. (1984). Vascular smooth muscle rhythmicity. In *Mechanisms of Blood Pressure Waves*. Japan Scientific Societies Press; Springer, 319-338.

[31] Baselli, G., Cerutti, S., Badilini, F., Biancardi, L., Porta, A., Pagani, M., Lombardi, F., Rimoldi, O., Furlan, R., Malliani, A. (1994). Model for the assessment of heart period variability interactions of respiration influences. *Medical and Biological Engineering and Computing*, 32 (2), 143-152.

[32] Phinyomark, A., Limsakul, C., Phukpattaranont, P. (2011). Application of wavelet analysis in EMG feature extraction for pattern classification. *Measurement Science Review*, 11 (2), 45-52.

[33] Mishra, P., Singla, S.K. (2013). Artifact removal from biosignal using fixed point ICA algorithm for preprocessing in biometric recognition. *Measurement Science Review*, 13 (1), 7-11.

[34] Unakafov, A. (2009). Analysis and modeling of the galvanic skins response spontaneous component in the context of intelligent biofeedback systems development. *Measurement Science Review*, 9 (2), 36-41.

Received July 3, 2016.
Accepted January 24, 2017.

MEASUREMENT SCIENCE REVIEW, **17**, (2017), No. 1, 48-52

DE GRUYTER OPEN

MEASUREMENT SCIENCE REVIEW

Journal homepage: http://www.degruyter.com/view/j/msr

ISSN 1335-8871

A Novel Adaptive Frequency Estimation Algorithm Based on Interpolation FFT and Improved Adaptive Notch Filter

Shen Ting-ao[1, 2], Li Hua-nan[1], Zhang Qi-xin[1], Li Ming[1]

[1]*Department of Petroleum Supply Engineering, Logistical Engineering University, Chongqing 401311, China*
[2]*Corresponding Email: 279522560@qq.com*

The convergence rate and the continuous tracking precision are two main problems of the existing adaptive notch filter (ANF) for frequency tracking. To solve the problems, the frequency is detected by interpolation FFT at first, which aims to overcome the convergence rate of the ANF. Then, referring to the idea of negative feedback, an evaluation factor is designed to monitor the ANF parameters and realize continuously high frequency tracking accuracy. According to the principle, a novel adaptive frequency estimation algorithm based on interpolation FFT and improved ANF is put forward. Its basic idea, specific measures and implementation steps are described in detail. The proposed algorithm obtains a fast estimation of the signal frequency, higher accuracy and better universality qualities. Simulation results verified the superiority and validity of the proposed algorithm when compared with original algorithms.

Keywords: Adaptive notch filter, frequency estimation, Fast Fourier Transform, negative feedback.

1. INTRODUCTION

Frequency is a basic parameter to describe the characteristic of the signal, which has been widely used in many fields such as power systems, flow measurement, and fault diagnosis.

In the past three decades, lots of frequency estimation algorithms have been proposed to provide good performance, such as FFT [1], wavelet transform [2], correlation [3], ANF [4]-[5], and so on. Compared with other frequency estimation algorithms, ANF can automatically adjust the parameters according to the measured signal characteristics, and realize the estimation and tracking of frequency. It is a research hotspot of the current frequency estimation algorithm [6]-[7]. But the algorithm is more sensitive to the initial parameter value, and it is difficult to balance the convergence rate and the long tracking precision.

To resolve the above problems, a novel adaptive frequency estimation algorithm based on interpolation FFT and improved ANF is proposed. In Section 2, the ANF is introduced and analyzed. In Section 3, the proposed algorithm is elaborated, including the interpolation FFT algorithm which is introduced to improve the short time signal frequency estimation, and the improved ANF which is used to monitor and track signal frequency for long time, by designing an evaluation factor to adjust the ANF parameters using the feedback control principle. In Section 4, the proposed algorithm is validated by simulations. Finally, Section 5 concludes.

2. ANALYSIS OF THE ADAPTIVE NOTCH FILTER

A. Principle of the adaptive notch filter

Adaptive notch filter (ANF) is used to obtain the filter parameters, which could automatically adjust the filter parameters of the current time, and adapt to the unknown changes of the signal and noise statistical characteristics. The frequency characteristic of the ideal notch filter equals to 1, and the other equals 0. ANF can make the notch frequency automatically follow the changing of the input signal frequency. It can be used to eliminate the interference and to detect the sinusoidal signal in noise frequency [8]. The realization of the ANF is shown in Fig.1.

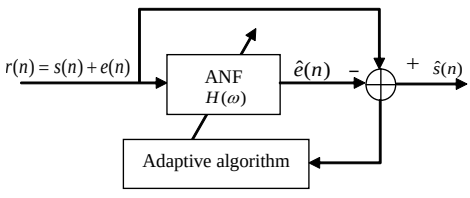

Fig.1. Structure of adaptive notch filter.

As shown in Fig.1., when an observation signal $r(n)$ gets through the ANF, sinusoidal signal $s(n)$ can be filtered, and the optimal estimation noise signal $\hat{e}(n)$ can be obtained, and then, by subtracting $\hat{e}(n)$ from the observed signal $r(n)$, the optimal estimation value $\hat{s}(n)$ can be obtained.

DOI: 10.1515/msr-2017-0006

B. Problem analysis

1) Convergence rate

According to the principle of ANF, if the input signal's a priori is unknown, the initial notch bandwidth tends to be larger, so that the signal frequency can be captured as soon as possible. But if the initial notch bandwidth is too wide, it will cause less filtered noise and lower accuracy of frequency estimation. With the adaptive adjustment of ANF parameters, the ANF will be gradually locked on the correct frequency, the notch bandwidth will be gradually reduced, the filtered noise will be higher, and the precision of frequency tracking will be much higher. The process of ANF from the beginning to locking on the correct frequency can be regarded as a convergence process, and the frequency estimation accuracy in the process is low.

In order to improve the precision of the frequency estimation in the convergence process of ANF, some frequency estimation methods can be used to improve the accuracy in the convergence process.

2) Continuous tracking problem

When the ANF is used to track the unknown signal frequency, to capture the signal frequency as quickly as possible, the initial notch bandwidth often sets to be larger. With the adaptive adjustment of ANF parameters, the convergence factor approaches to 1, the notch bandwidth approaches to 0, and the accuracy of the frequency estimation will be higher and higher. When the notch bandwidth approaches 0, if the signal frequency changes and jumps out of the notch bandwidth, it will cause the notch in false frequency, and then cause larger frequency estimation error.

In the process of frequency tracking, along with the continuous adjustment of ANF parameters, the notch bandwidth will be gradually reduced. If the notch bandwidth approaches 0, it will easily lead to the correct frequency out of the notch bandwidth, so that the ANF cannot perceive the change of the signal frequency, and then a larger frequency estimation error will be caused, which can be regarded as the tracking problem for long time.

To improve the frequency tracking estimation accuracy for long time, when the notch bandwidth approaches 0, an evaluation factor can be set up to monitor and adjust ANF parameters in real-time, which aims to ensure the frequency value in notch bandwidth range and prevent the ANF loss of adaptive ability. All the aforementioned problems can be improved by adjusting the notch bandwidth.

3. PROPOSED ALGORITHMS

A. Basic ideas

From the above analysis, it is difficult to balance the convergence rate and the continuous tracking precision. Therefore, a novel frequency tracking algorithm based on interpolation FFT and improved ANF is put forward in this paper. Firstly, interpolation FFT algorithm is used to estimate the initial signal frequency, and the estimated value is set as the initial frequency before the ANF is stable (assuming a stable point of the ANF at M), and then, the improved ANF is used to estimate the signal frequency after M. M is an empirical value which could be obtained by lots of simulations, and it often sets among 500~1000.

B. Concrete measure

1) Convergence problem

In order to overcome the problem of the convergence rate of ANF, the interpolation FFT algorithm is used to estimate the short time frequency of the signal as follows.

Set the single frequency sine signal as follows

$$s(t) = A\cos\left(2\pi f_0 t + \theta_0\right) \tag{1}$$

where A, f_0 and θ_0 denote the amplitude, frequency, and initial phase of the signal, respectively. Generally, f_0 is expressed as:

$$f_0 = (k_0 + \delta)\cdot f_d \tag{2}$$

where k_0 denotes positive integer, δ denotes leakage errors and $|\delta| \le 0.5$, f_d denotes frequency resolution and $f_d = f_s / N$, f_s denotes sampling frequency, N denotes sampling number. The sampled signal can be illustrated as:

$$s(n) = A\cos[2\pi(k_0 + \delta)\cdot n / N + \theta_0] \tag{3}$$

The frequency spectrum $S(k)$ can be obtained by DFT.

$$S(k) = \frac{A\cdot\sin\left[\pi\left(k - f_0 T\right)\right]}{2\sin\left[\pi\left(k - f_0 T\right)/N\right]}\cdot e^{j\left[\theta_0 - \frac{N-1}{N}(k - f_0 T)\pi\right]} \tag{4}$$

where T is the sampling time, and $f_d = f_s / N = 1/T = \Delta f$. Assuming $k_1 = \mathrm{int}\left[f_0 T\right]$ is the maximum amplitude point at $S(k)$. The maximum amplitude value A_1 can be expressed as:

$$A_1 = \left|S\left(k_1\right)\right| = \frac{NA\sin\left(\pi\delta\right)}{2\pi\delta} \tag{5}$$

The line of the relatively large amplitude next to k_1 is called second-rate amplitude value [9]. Assume the discrete frequency index value is k_2, the second-rate amplitude value A_2 can be approximated as:

$$A_2 = \left|S\left(k_2\right)\right| = \frac{NA\sin\left(\pi\delta\right)}{2\pi\left(1 - |\delta|\right)} \tag{6}$$

$$\alpha = \frac{A_2}{A_1} = \frac{\delta}{1 - |\delta|} \tag{7}$$

$$|\delta| = \frac{\alpha}{1+\alpha} = \frac{A_2}{A_1 + A_2} \tag{8}$$

According to the value of δ, the estimated higher accuracy frequency value of $\hat{f}_0$ can be obtained.

$$\hat{f}_0 = \left(k_1 \pm |\delta|\right)\Delta f \tag{9}$$

In equation (9), the symbol is dependent on the position of k_2. If $k_2 = k_1 + 1$, it gets plus sign. If $k_2 = k_1 - 1$, it gets minus sign.

2) Long time tracking problem

By using the negative feedback control principle, the parameters of ANF can be monitored and adjusted in real-time by setting an evaluation factor and the algorithm can be illustrated as follows.

As shown in Fig.1., the enhanced signal $\hat{s}(n)$ is independent of the noise $z(n)$. If the ANF works normally, the enhanced signal $\hat{s}(n)$ is significantly correlated with the initial input signal $r(n)$. According to the correlation, an evaluation factor $h(n)$ can be designed to detect whether the ANF is an effective tracking signal frequency or not. The structures of the improved ANF are shown in Fig.2.

The value of $h(n)$ can be obtained from the extra LMS block algorithm by the following:

$$\begin{cases} \varepsilon(n) = \hat{s}(n) - h(n)r(n) \\ h(n) = h(n-1) + \mu_h \varepsilon(n) r(n) \end{cases} \tag{10}$$

where μ_h is the step size, h is deduced from the Wiener-Hopf equation in [10].

$$\begin{aligned} & h \cdot E\left\{r^2(n)\right\} = E\left\{r(n)\hat{s}(n)\right\} \\ \Leftrightarrow\ & h \cdot E\left\{\left[s(n)+e(n)\right]^2\right\} = E\left\{\left[s(n)+e(n)\right]\hat{s}(n)\right\} \\ \Leftrightarrow\ & h \cdot \left(E\left\{s^2(n)\right\} + E\left\{e^2(n)\right\}\right) = E\left\{s(n)\hat{s}(n)\right\} + E\left\{e(n)\right\}E\left\{\hat{s}(n)\right\} \\ \Leftrightarrow\ & h = \frac{E\left\{s(n)\hat{s}(n)\right\}}{A^2/2 + \sigma_e^2} \end{aligned} \tag{11}$$

where $E\left\{s(n)e(n)\right\} = 0$, $E\left\{e(n)\right\} = 0$, $E\left\{e^2(n)\right\} = \sigma_e^2$, $E\left\{s^2(n)\right\} = A^2/2$.

If the ANF locks on the right frequency, then $\hat{s}(n) \approx s(n)$, and h converges to

$$h = \frac{A^2/2}{A^2/2 + \sigma_e^2} = \frac{A^2}{A^2 + 2\sigma_e^2} \tag{12}$$

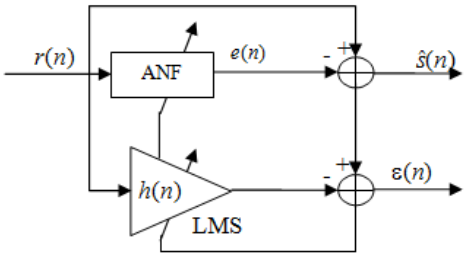

Fig.2. Structures of the improved adaptive notch filter.

If the ANF locks on the wrong frequency, then $\hat{s}(n) \approx e(n)$, substitute it into equation (11), and h converges to 0 since $E\left\{s(n)\hat{s}(n)\right\} = 0$. Therefore, the evaluation factor $h(n)$ can be used to judge whether the ANF effectively tracks the signal frequency or not. If the $h(n)$ falls below the set value T_h, the ANF can resume the parameters to assure the notch bandwidth contains the signal frequency again.

According to the above basic ideas, the improved ANF algorithm is illustrated in Fig.3.

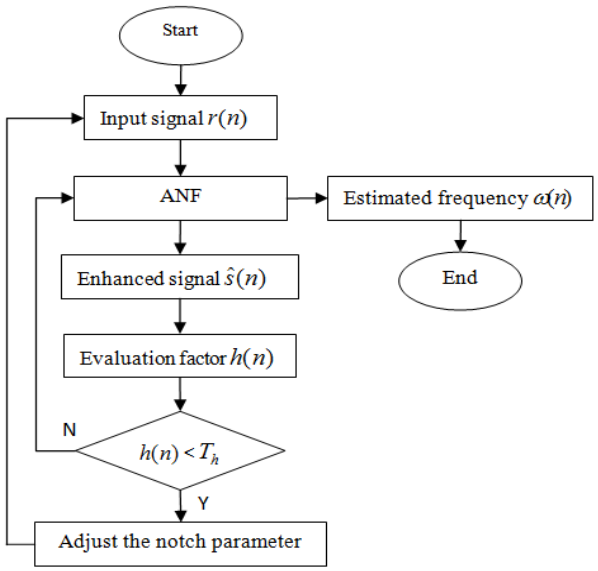

Fig.3. Flow chart of the improve ANF.

The overall block diagram of the proposed technique is summarized in Fig.4.

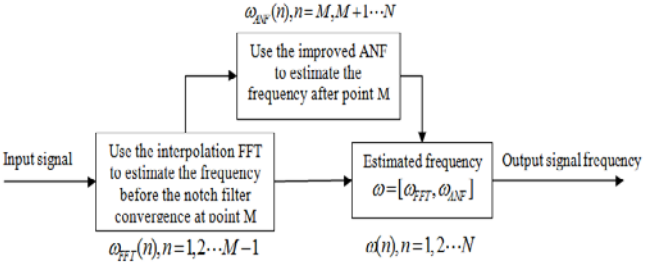

Fig.4. Flow chart of the proposed frequency estimation algorithm.

As shown in Fig.3. and Fig.4., the proposed algorithm obtains fast frequency tracking, long time frequency tracking and high accuracy estimation characteristics even for the unknown signal.

4. SIMULATION ANALYSES

In order to verify the validity and the universality of the proposed algorithm, the algorithm is applied in lattice adaptive notch filter (L-ANF) [11], simplified lattice adaptive notch filter (SL-ANF) [12], and SMM adaptive notch filter (SMM-ANF) [13], respectively. In simulations, the input signal model and ANF parameters refer to references [11]-[13], and all the ANF parameters remain unchanged. The proposed algorithm just introduces the FFT algorithm at the beginning of the frequency estimation, and adds an evaluation factor in ANF for long-time frequency estimation, the parameters $T_h = 0.05$ and $\mu_h = 0.008$.

Fig.5. shows the estimated frequencies by original L-ANF and the improved algorithm in this paper based on L-ANF. Fig.6. shows the estimated frequencies by original SL-ANF and the improved algorithm in this paper based on SL-ANF. Fig.7. shows the estimated frequencies by original SMM-ANF and the improved algorithm in this paper based on SMM-ANF. In order to validate the universality of the proposed method in this paper, the curves of Fig.5. to Fig.7. are randomly generated.

As shown in Fig.5. to Fig.7., which include L-ANF, SL-ANF and SMM-ANF, there are convergence process and long precision problem when tracking signal frequencies. Compared with the original algorithm, the improved algorithm of frequency tracking curve is better and closer to the true frequency. The proposed algorithm maintains higher estimation accuracy in the whole process of frequency tracking, which overcomes the influence of the convergence process, and solves the problem of long time tracking. In addition, we can see from Fig.5. to Fig.7., that the proposed algorithm can be applied to many kinds of ANF, and all the randomly generated curves maintain a good tracking effect, which verifies the universality of the proposed algorithm.

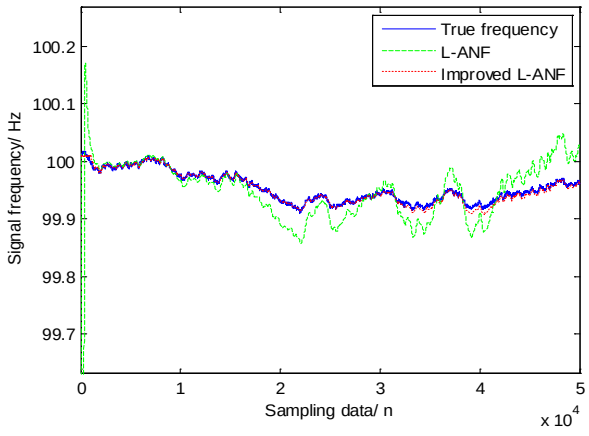

Fig.5. Comparisons by L-ANF and proposed method.

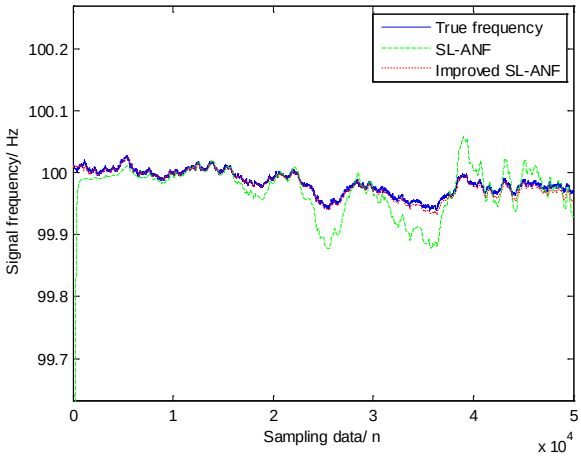

Fig.6. Comparisons by SL-ANF and proposed method.

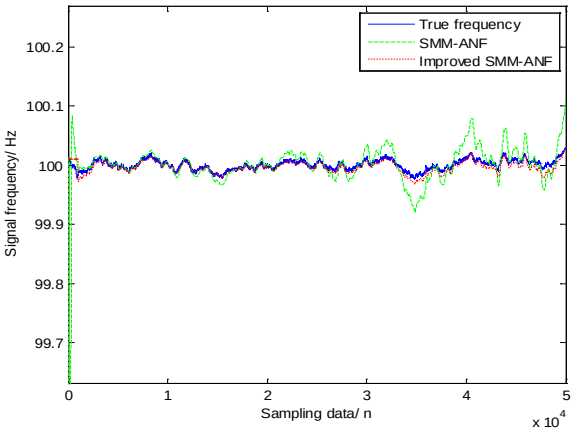

Fig.7. Comparisons by SMM-ANF and proposed method.

Testing 100 independent and random experiments, the mean of square errors (MSE) of the three types of ANF is compared and calculated according to the equation (13), which is shown in Table 1. To avoid the influence of convergence of the ANF algorithms, the signals after 1000th point are intercepted to calculate the frequency.

$$MSE = \frac{1}{49000}\sum_{i=1001}^{50000}[\hat{\omega}(i) - \omega(i)]^2 \tag{13}$$

As shown in Table 1., the MSE of the proposed algorithm is smaller than the original algorithm, which also demonstrates the superior performance of the proposed algorithm.

Table 1. Comparisons of MSE acquired by three types of ANF.

ANF	**MSE**	
	Original algorithm	**Proposed algorithm**
L-ANF	3.72×10^{-7}	1.66×10^{-8}
SL-ANF	3.57×10^{-7}	1.65×10^{-8}
SMM-ANF	3.19×10^{-7}	1.64×10^{-8}

5. CONCLUSIONS

In order to solve the problem of convergence rate and long time frequency tracking, a new frequency estimation algorithm based on interpolation FFT and improved ANF is proposed. Simulations show that the proposed algorithm obtains the following characteristics:

1) Using interpolation FFT algorithm in the initial stage of signal frequency estimation, which can improve the convergence process of frequency estimation accuracy, at the same time, the estimate value by interpolation FFT algorithm can be used as the initial frequency, which could speed up the convergence rate of the ANF.

2) Using the negative feedback control theory to design the evaluation factor, it can effectively solve the problem of long time frequency tracking of the ANF.

3) The proposed algorithm is more universal, which can apply to other types of ANF.

For future research, we will focus on extending and generalizing this type of algorithms to a more general system identification scheme, and further research is under discussion.

ACKNOWLEDGMENT

This work was supported by National Natural Science Foundation of China (Grant Nos. 61601493) and Science Foundation of Logistical Engineering University (Grant Nos. YQ16-420804). The authors would like to thank the Associate Editor and the reviewers for their helpful comments, which improved the quality of this paper.

REFERENCES

[1] Chen, K., Wang, J., Zhang, S. (2008). Spectrum correction based on the complex ratio of discrete spectrum around the main-lobe. *Journal of Vibration Engineering*, 21 (3), 314-318.

[2] Wang, X., Xu, K. (2005). Fundamental wave extraction and frequency measurement base on wavelet transform. *Chinese Journal of Scientific Instrument*, 26 (2), 146-151.

[3] Ksibi, R.E., Besbes, H., Valcarce, R.L., Cherif, S. (2010). Frequency estimation of real-valued single-tone in colored noise using multiple autocorrelation lags. *Signal Processing*, 90 (7), 2303-2307.

[4] Loetwassana, W., Punchalard, R., Koseeyaporn, J., Wardkein, P. (2012). Unbiased plain gradient algorithm for a second-order adaptive IIR notch filter with constrained poles and zeros. *Signal Processing*, 90 (8), 2513-2520.

[5] Punchalard, R. (2012). Mean square error analysis of unbiased modified plain gradient algorithm for second-order adaptive IIR notch filter. *Signal Processing*, 92 (11), 2815-2820.

[6] George, N., Anthony, T. (2010). Application of adaptive lattice filters for modal parameter tacking of a single flexible link carrying a shifting payload. *Mechanical Systems and Signal Processing*, 24 (5), 1338-1348.

[7] Regalia, P.A. (2010). A complex adaptive notch filter. *IEEE Signal Processing Letters*, 17 (11), 937-940.

[8] Cho, N.I., Choi, C.H., Lee, S.U. (1989). Adaptive line enhancement by using an IIR lattice notch filter. *IEEE Transactions on Acoustics, Speech and Signal Processing*, 37 (4), 585-589.

[9] Shen, T., Tu, Y., Li, M., Zhang, H. (2015). A new phase difference measurement algorithm for extreme frequency signals based on discrete time Fourier transform with negative frequency contribution. *Review of Scientific Instruments*, 86 (1), 015104.

[10] Ta, M., Thai, H., DeBrunner, V. (2009). Stochastic search methods to improve the convergence of adaptive notch filter. In *IEEE 13th Digital Signal Processing Workshop*, January 4-7, 2009. IEEE, 78-83.

[11] Xu, K., Ni, W., Chen, Z. (2006). A signal processing method for Coriolis mass flowmeter based on time-varying signal model and lattice notch filter. *Chinese Journal of Scientific Instrument*, 27 (2), 596-601.

[12] Ni, W., Xu, K. (2007). A signal processing method for Coriolis flowmeter based on time-varying signal model and normalized lattice notch filter. *Acta Metrologica Sinica*, 28 (3), 243-247.

[13] Tu, Y., Su, F., Shen, T., Zhang, H. (2011). Frequency tracking method and simulation for Coriolis Mass Flowmeter based on new adaptive notch filter. *Journal of Chongqing University*, 34 (10), 147-152.

Received October 26, 2016.
Accepted February 2, 2017.